UC Riverside
UC Riverside Electronic Theses and Dissertations

Title

Investigation of Excitonic, Electronic and Thermal Properties of Two-Dimensional and Quasi-One-Dimensional Materials

Permalink

https://escholarship.org/uc/item/3wk7g9tv

Author

Debnath, Bishwajit

Publication Date

2018

Copyright Information

Peer reviewed|Thesis/dissertation

UNIVERSITY OF CALIFORNIA
RIVERSIDE

Investigation of Excitonic, Electronic and Thermal Properties of Two-Dimensional
and Quasi-One-Dimensional Materials

A Dissertation submitted in partial satisfaction
of the requirements for the degree of

Doctor of Philosophy

in

Electrical Engineering

by

Bishwajit Debnath

December 2018

Dissertation Committee:

    Dr. Roger K. Lake, Chairperson
    Dr. Alexander Balandin
    Dr. Jianlin Liu

The Dissertation of Bishwajit Debnath is approved:

_____

_____

_____
                                    Committee Chairperson

University of California, Riverside

Acknowledgments

I want to thank my advisor and mentor, Professor Roger K. Lake, for his unlimited support, encouragement and guidance during my PhD. Over the past four years, I have learned a lot from him about material science engineering, condensed matter physics, device modeling, as well as scientific writings for publications and proposals. Many times he has saved me from losing grip and focus, whenever I was struggling with my projects, and offered me insight and kind directions to overcome such challenges. He has taught me how to approach any scientific problem starting from the scratch, and how to build up the understanding by focusing on the underlying physics. Without his unparalleled support, none of these works would have been possible.

I also want to thank my committee member Prof. Alexander Balandin, for all the fruitful collaborations with his POEM and NDL groups over the years. I have learned a lot about the experimental side of device fabrication and characterization from Dr. Balandin and his group, through our valuable discussions, meetings and feedback. I appreciate his kind encouragement in allowing me to participate with his group's experiments and in providing theoretical support for explaining the experimental results. I also want to thank my committee member Dr. Jianlin Liu, for giving me the amazing opportunity to collaborate with his students on numerous projects. I am also grateful to all my committee members for providing me valuable feedback on my dissertation.

Special thanks to my current labmates in LATTE lab, Chenyang Li, Rakibul Karim Akanda, Nima Djavid, In Jun Park, as well as my former colleagues and friends Dr. Protik Das, Dr. Gen Yin, Dr. Shanshan Su, and Dr. Darshana Wickramaratne, for their

The text of this dissertation, in part or in full, is a reprint of the material as it appears in the following journal:

- Physical Review B [45] [2017]. American Physical Society

To my dear brother, Topojit Debnath

I leave this book to you.

ABSTRACT OF THE DISSERTATION

Investigation of Excitonic, Electronic and Thermal Properties of Two-Dimensional and
Quasi-One-Dimensional Materials

by

Bishwajit Debnath

Doctor of Philosophy, Graduate Program in Electrical Engineering
University of California, Riverside, December 2018
Dr. Roger K. Lake, Chairperson

We explore the excitonic, electronic, phononic and thermal properties of low-dimensional

materials, specifically the two-dimensional and quasi-one-dimensional transition metal chalco-

genides. The possibility of observing Bose-Einstein exciton condensation (BEC) in tran-

sition metal dichalcogenides (TMDs) has been analyzed at three different levels of theory.

We find that, in the strong coupling regime, mean field theory with either an unscreened

or screened interlayer interaction predicts a room-temperature condensate. However, in-

tralayer interactions can essentially renormalize the quasiparticle dispersion, which can be

captured by many-body GW formalism. In the strong coupling regime, the improved BEC

theory predicts that intralayer interactions have a large impact on the condensate order pa-

rameter, as well as on its functional dependencies on effective mass and carrier density. We

also explore the thermal properties of 2D materials, specifically in the misoriented bilayer

graphene (m-BLG) system, using ab initio density functional theory (DFT) and phonon

Boltzmann transport equation (BTE). we find that the lattice thermal conductivity of m-

BLG reduces to almost half of its unrotated counterpart. To explain the phonon dynamics,

we analyze the phonon dispersions, phonon velocity distributions, occupations, density of states and heat capacity, both before and after misorientation. Detailed calculation of the phonon-phonon scattering lifetime reveals that, the increased umklapp scattering in the acoustic and quasi-acoustic phonon branches is the main reason for the reduced thermal conductivity in m-BLG system. We also explore the thermal conductivity of quasi-1D materials, specifically $TaSe_3$ and NbS_3, using ab initio DFT and phonon BTE. We find that both materials exhibit highly anisotropic thermal transport. A thermal conductivity of 6.3 W/m·K (70.6 W/m·K) is observed for metallic $TaSe_3$ (semiconducting NbS_3) along the chain direction. In-depth study of velocity and lifetime distribution shows that lower scattering and higher phonon velocity in NbS_3 are the reasons behind such higher thermal conductivity. The umklapp scattering process is found to be the dominant phonon scattering mechanism in this family of low-dimensional materials. We also investigate the electronic and vibrational properties of different phases of the quasi-1D material NbS_3. We find that the dimerized phase NbS_3-IV is a semiconductor, whereas the undimerized phase NbS_3-V is a metal. Similarity between the band dispersions of phase-I and phase-IV arises from the similarity in their structures, in spite of some stacking and chiral faults. Both phase-I and phase-IV are dynamically stable, whereas the phonon dispersion in phase-V exhibits instability along the inter-chain and growth direction, indicating a possible charge density wave ground state. Finally, we explore the band alignment properties of different quasi-1D transition metal trichalcogenides (TMTs). From the DFT calculations, we can identify several TMTs as promising candidates for ohmic contacts and tunnel FET devices.

Contents

List of Figures

List of Tables

Chapter 1

Rationale

1.1 Objectives

Over the last decade, the world has eagerly seen how the discovery of atomically-thin graphene has revolutionized device engineering, by vigorously adopting the low-dimensional materials [214, 26, 36, 228, 57, 18, 152]. As worthy companions to graphene, other 2D materials, e.g. transitional metal dichalcogenides (MoS_2, WS_2, etc.), have broadened those engineering efforts, and resulted in a plethora of electronic, mechanical, optical and thermal 2D devices [124, 87, 125, 72, 124, 87, 125, 111, 246, 153, 177, 190, 181]. However, one of the unexplored directions, where 2D materials can push the knowledge boundaries of "cold-atom" physics, is the realization of Bose-Einstein exciton condensate (BEC) [27, 202, 102, 209, 155, 242, 103, 174]. In BEC, the electron-hole pairs can "condense" into a single quantum state and exhibit exciting phenomena like gravity-defying superfluidity and dissipation-less transport [2, 61, 204, 138]. In my research, I will explore the possibility of using 2D materials to find this "elusive" Bose-Einstein condensate. Furthermore, I will

also study the criteria and phase map for realizing such condensate in experimental setup.

Another hurdle that the material scientists and device engineers are facing is excessive heat management, which is a natural byproduct of superior processing power. Two-dimensional materials like bilayer graphene (BLG), which exhibit very high thermal conductivity [8, 70], is an excellent candidate for extracting heat from overheated semiconductor devices [7, 234, 186, 194, 195, 99]. However, during growth and transfer, BLG samples often show unintentional interlayer twisting, which negatively impacts the heat conduction [162, 187, 33, 81, 37, 30, 215, 165, 123, 122]. Understanding the microscopic physics of heat transport, in terms of quantum unit "phonons", is an essential step towards designing efficient heat-extracting devices based on BLG. To complete this knowledge gap, I will explore the phonon dynamics and thermal conductivity of twisted bilayer graphene using ab initio density functional theory and Boltzmann phonon transport theory. I will also explain the physical mechanism behind such phonon-limited heat transport.

As the research initiatives for 2D materials are reaching saturation, both the industry and academia are looking for next family of low-dimensional materials. One such direction is the quasi-1D materials, specifically transition metal trichalcogenides (TMT) [89, 192, 79, 229, 180, 253]. Due to their inherent low-dimensionality and anisotropic behavior [97, 85, 254, 184, 95, 41, 88, 172, 40, 110], the quasi-1D TMT materials can be very promising in designing heat extracting devices. However, a full investigation of the thermal stability and thermal conductivity in quasi-1D materials are still missing. Hence, in my research, I will explore and evaluate the thermal properties of TMT materials, for both semiconducting and metallic phases, thus filling in the gap of current understanding

of phonon dynamics in quasi-1D materials.

A second reason behind the popularity of quasi-1D materials is the rich phase chemistry they can present [180, 219, 231, 104, 185]. Depending on the growth conditions, they can exhibit numerous phases by allowing small stacking or chiral faults in their unit cell [90, 25, 253, 15]. Interestingly, these variations in structure can result in quite different properties of materials, ranging from metallic to semiconductor, from superconductor to insulator, and from exhibiting an incommensurate charge density wave phase to commensurate charge density wave phase [236, 191, 73, 253]. Recently, Several new phases of NbS_3 have been reported [15], but the electronic and vibrational properties of these phases are yet unknown. Some of these phases are very promising in showing charge density waves (CDW) at high temperatures, making them very good candidate for room-temperature CDW-based devices [134]. To explore the possibilities of room-temperature CDW in such chemically-rich material system, I will also theoretically investigate the known-phases of this quasi-one dimensional NbS_3, using ab initio density functional theory. Both the electrical performance and the phonon dispersion will be studied, to explore the dynamical stability of the discovered phases, as well as to predict any possible commensurate structures for this material.

Along with the promise of better thermal response and attractive phase engineering, transitional metal trichalcogenides can also become ideal candidate for next-generation electronic contacts [95]. TMT grows in μm-long chains, can sustain high current and is only several 100 nm thick [170, 59, 105, 75, 171, 135]. They can solve the contact scaling problems in semiconductor industry by replacing the existing bulky contacts [98, 43, 34, 71]. Since

the thermal performance of these quasi-1D materials makes them promising for heat extraction, choosing certain TMT materials with better electrical contact efficiencies and better heat-sink capabilities, will facilitate dual functionality in future contact design. However, before such industrial appropriation, a comprehensive theoretical study of their electronic performance as contact is necessary. To evaluate these issues, I will categorically calculate the electronic dispersions and band alignment properties of different members of TMT material family. Both metallic and semiconducting polymorphs of quasi-1D materials will be studied to evaluate the best possible combinations, both for contacts and tunnel FET devices.

1.2   Organization

The rest of the dissertation is organized as follows. Chapter 2 presents the investigation of Bose-Einstein condensate in two-dimensional transitional metal dichalcogenides, using different level of theory. Chapter 3 presents density functional theory calculations of phonon dispersion and thermal conductivity of misoriented bilayer graphene. Chapter 4 presents the investigation of ab initio thermal conductivity in quasi-1D materials $TaSe_3$ and NbS_3. Chapter 5 presents the theoretical calculations of electronic and vibrational properties of different phases of NbS_3. Chapter 6 explores the electronic properties and band alignment of different quasi-1D materials.

Chapter 2

Exciton condensate in bilayer transition metal dichalcogenides: strong coupling regime

2.1 Introduction

Electron-hole (e-h) bilayer systems, such as the one illustrated in Fig. 2.1 (a), are good candidates for observing exciton condensation [142]. The presence of an exciton condensate results in a gapped spectrum for the e-h bilayer system, as illustrated in Fig. 2.1 (b). Although there is evidence of exciton condensation in GaAs double quantum wells in the quantum Hall regime [27, 202, 102, 209], the zero-field exciton condensate remains elusive. Recently, focus has returned to engineering a bilayer exciton condensate in the absence of a magnetic field in two-dimensional crystals, such as graphene [155, 242, 103,
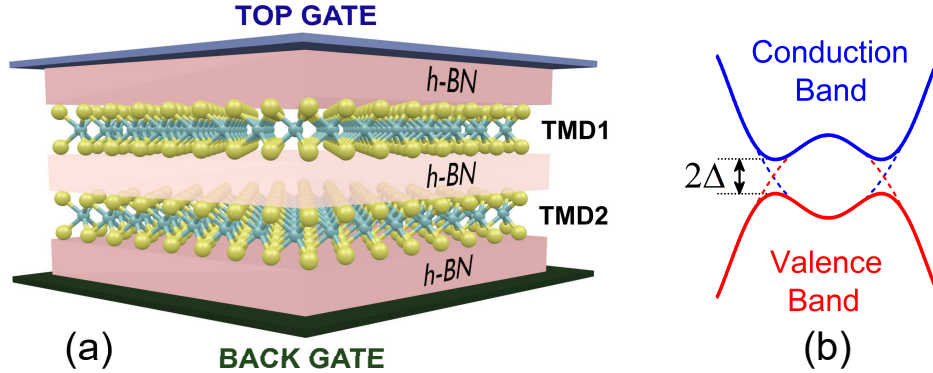
Figure 2.1: (a) Illustration of two monolayers of transition metal dichalcogenides separated by a thin film of hexagonal boron nitride (h-BN). The Fermi levels of the top and bottom monolayers are tuned to induce equal electron and hole carrier densities. (b) The conduction band of the electron layer and the valence band of the hole layer overlap, and in the presence of a condensate, a gap (2Δ) opens in the dispersion.

174, 2, 61, 204, 138] and transition metal dichalcogenides [63, 224, 226, 138].

Graphene appears to be an attractive candidate for the realization of bilayer exciton condensates due to its perfect particle-hole nesting [155, 242]. Mean field calculations with the bare Coulomb interaction predict high transition temperatures (~ 300 K) [155]. However, screening effects in graphene are of the order of the Fermi wavevector (k_F). As a result, static screening reduces the transition temperatures significantly [103, 74, 61]. The predicted transition temperatures in the e-h graphene bilayer systems range from 1 mK – 100 K [155, 242, 141, 103, 143, 137, 156, 61], depending on the level of the theory. A study which includes dynamical effects on the screened interactions estimates a transition temperature $T_c \sim 4$ K [200]. Another study taking into account the screening resulting from proximity gates found transition temperatures in the 1 mK–1 K range [61]. Replacing each monolayer of graphene with a bilayer of graphene has been suggested for increasing the transition temperature [238].

The strength of the exciton condensate is proportional to the coupling strength λ, which is the ratio of the interaction energy to the band energy. This ratio is the fine structure constant in graphene given by $\lambda = e^2/[\kappa \hbar v_F] \sim 2.2/\kappa$ [155, 140, 200], where κ is the dielectric constant of the barrier material and v_F is the Fermi velocity. Graphene's fine structure constant is density independent and typically $\lambda \lesssim 1$, which is a good approximation for weak coupling theories. However for parabolic bands, such as those in bilayer graphene and transition metal dichalcogenides (TMDs), λ is density dependent. In this case, $\lambda \approx 6gm_+/(\kappa k_F)$, where m_+ is the reduced electron-hole mass of the e-h bilayer system, g is the degeneracy, and $k_F \propto \sqrt{n_{2D}/g}$ is the Fermi momemtum that depends on electron density n_{2D}. In bilayer graphene, the low effective mass gives $\lambda = 0.2 \sim 1.1$, so that weak coupling theories also apply.

TMDs have larger effective masses and typically larger values of $\lambda = 2.2 \sim 10.4$, depending on the carrier density of $10^{11} \sim 10^{12}$ cm^{-2}. Larger masses result in larger excitonic binding energies that would appear more suitable for higher exciton gaps and transition temperatures [63, 29]. Mean field calculations using the unscreened Coulomb interactions do predict room temperature condensation, and they also predict higher condensation temperature for higher carrier densities (n_{2D}). However, for higher carrier densities, screening effects should be considered. In graphene bilayers, screening incorporated within a random phase approximation (RPA) reduces the interlayer coherence [174], as one would expect. On the other hand, in TMD bilayers with $\lambda > 1$, RPA screening has little effect on the interlayer coherence. However, since TMD bilayers lie in the strong coupling regime, quasiparticle renormalization influences the order parameter significantly.

In this work, we formulate an intermediate/strong coupling theory for the TMD bilayer exciton condensate by incorporating screening effects in the RPA and the quasi-particle self-energy correction, self-consistently with the exciton gap. The inter-layer and the intra-layer RPA screened interaction is used to calculate the quasi-particle self-energy, within the GW approximation. Screening not only affects the *interlayer* interaction, but it also affects the *intralayer* interaction (within the same monolayer). The intra-layer interaction renormalizes the effective mass and the corresponding λ. In this approach, the excitonic gap is calculated self-consistently as a function of the renormalized λ. The inclusion of the self-energy renormalization reverses the trends predicted from the unscreened and screened MF theories. The heavy masses of the TMD materials that increase the order parameter in the MF theories, decrease the order parameter when the interlayer and intralayer screening are self-consistently included. High carrier density limits the condensation gap due to screening, and low carrier density (i.e. strong coupling) reduces the condensation gap due to mass renormalization.

Typically, beyond mean field, diffusion quantum Monte Carlo (QMC) simulations are employed to predict the condensate temperature. This approach includes both interlayer and intralayer screening, as well as vertex corrections [160]. For the graphene bilayer, these studies suggest that screening effects destroy the superfluidity at high carrier densities, but it can survive at low carrier density [174]. This indicates that correlations play a significant role, especially in the strong coupling regime [44]. Our strong coupling approach is comparable to QMC approach in prediction of the gap behavior of excitonic condensates. It also provides insight into the different physics that govern the trends. Additionally, since

Table 2.1: TMD material parameters obtained using density functional theory (HSE-SOC) [220]. m_α is the longitudinal effective mass at the valence band edge (K_v) and the conduction band edge (K_c), in the units of free electron mass m_0. ϵ is the relative dielectric constant of each monolayer. n_{2D} and k_F are the maximum allowed electron density and Fermi wavevector for one-type of spin determined by the conduction spin-splitting energy Δ_c.

Material	Effective Mass (m_α)		Band Splitting		ϵ	n_{2D}	k_F
	K_v	K_c	$\Delta_v(meV)$	$\Delta_c(meV)$		$(\times 10^{12}\,cm^{-2})$	(nm^{-1})
MoS$_2$	0.485	0.407	188.6	9.9	3.43	0.4	0.1585
MoSe$_2$	0.503	0.435	254.8	36.9	4.74	1.7	0.3268
MoTe$_2$	0.576	0.501	317.4	43.7	5.76	2.3	0.3801
WS$_2$	0.304	0.331	528.7	12.0	4.13	0.4	0.1585
WSe$_2$	0.303	0.358	606.4	7.80	4.63	0.3	0.1373

the diffusion QMC studies include vertex corrections, which are missing in our approach, comparison of the two approaches can indicate the optimal approximation to accurately predict the transition temperatures in exciton condensates.

The remainder of the paper is organized as follows. Section 2.2 describes the effective model for TMDs used in this paper. Section 2.3 discusses the standard mean field treatment of the model Hamiltonian for the bilayer TMD system with an unscreened interaction. In section 2.4, we include RPA screening and a self-energy renormalization in a GW approximation and compare the predictions of the different levels of theory. Section 2.5 summarizes and concludes.
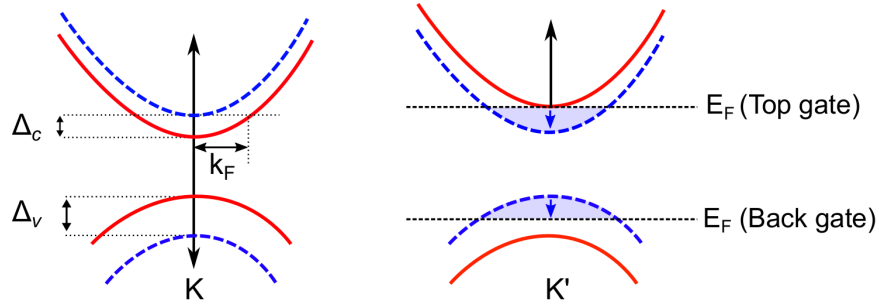
Figure 2.2: Spin composition at **K** and **K**′ of monolayer MoX$_2$ TMDs [112]. Up- and down-spin bands are denoted by solid-red and dash-blue lines, respectively. Spin-orbit coupling causes spin splitting of the conduction band (Δ_c) and the valence band (Δ_v).

2.2 Effective model for e-h TMDs bilayers

We consider several TMD electron-hole bilayers separated by an insulating h-BN spacer layer, as illustrated in Fig 2.1 (a). Separation of the electron and hole layers by a barrier reduces the overlap of their respective wavefunctions which reduces the interlayer tunneling and recombination [63]. The Fermi level lies in the conduction band of the top monolayer and in the valence band of the bottom monolayer.

The two layers of the bilayer system can consist of the same TMDs (homo-bilayer) or different TMDs (hetero-bilayer). To achieve high critical temperatures for exciton condensation particle-hole nesting is beneficial, (*i.e.*, $|m_e| = |m_h|$). The electron and hole masses in TMDs are similar but not equal, therefore, we consider different homo- and hetero-layer TMD combinations.

Table 2.1 shows the spin-resolved band parameters, the effective masses and maximum 2D carrier density for several monolayer TMDs. Our calculations of the electronic structure of the monolayer TMDs are based on spin-resolved density functional theory as implemented in the Vienna Ab-initio Simulation Package (VASP) [115, 114]. We use the

hybrid functional of Heyd-Scuseria-Ernzerhof (HSE) [83] where the fraction of screened Fock exchange α was set to 0.25 which results in band gaps for the monolayers of each material that are in agreement with the experimentally reported band gaps of each material [245, 51, 244]. A 400 eV energy cut-off was used, and spin-orbit interaction was included self-consistently in all calculations. Calculations were done using a Γ centered (12 $\times$ 12 $\times$ 1) Monkhorst-Pack k-point grid. Each of the monolayer unit cells were constructed using 20 Å of vacuum to achieve negligible interaction between the periodically repeating surfaces. The conduction and valence band effective masses at K_v and K_c are calculated for each material by fitting the dispersion around the extrema of each valley to a fourth order polynomial and then calculating $1/m^* = \frac{1}{\hbar^2} d^2 E/dk^2$ [220]. From the effective masses in Table 2.1, we identify several TMD bilayer combinations with partial electron-hole nesting (*i.e.*, $|m_e| \sim |m_h|$). All of the n-type layers are chosen from the MoX$_2$ materials with spin splitting illustrated in Fig. 2.2 [248, 112]. The spin splitting of the conduction band Δ_c sets the maximum Fermi level for each calculation. Within this limit, each band of each K-valley is spin polarized.

Treating the electron and hole dispersions as parabolic, the model Hamiltonian for the structure is $\mathcal{H} = \mathcal{H}_0 + \mathcal{H}_{e-e}$,

$$\mathcal{H} = \sum_{\mathbf{k}\sigma\alpha} \epsilon_{k,\sigma}^{\alpha} c_{\mathbf{k}\sigma\alpha}^{\dagger} c_{\mathbf{k}\sigma\alpha} + \frac{1}{2S} \sum_{\mathbf{q}\alpha\beta} V_{\alpha\beta}(q) \rho_{\alpha}(\mathbf{q}) \rho_{\beta}(-\mathbf{q}), \tag{2.1}$$

where $c_{\mathbf{k},\sigma,e}^{\dagger}$ ($c_{\mathbf{k},\sigma,h}^{\dagger}$) denote the electron (hole) creation operators, σ denotes the spin and valley quantum numbers for the electron/hole, $\mathbf{k} = (k_x, k_y)$ is the in-plane two-dimensional momentum with $k = \sqrt{k_x^2 + k_y^2}$, S is the area of the bilayer, $\alpha(\beta) \in \{e, h\}$ are the electron/hole layer indices, $\epsilon_{k,\sigma}^{\alpha=e} = \hbar^2(k^2 - k_F^2)/(2m_{e,\sigma})$, $\epsilon_{k,\sigma}^{\alpha=h} = -\hbar^2(k^2 - k_F^2)/(2m_{h,\sigma})$, k_F is
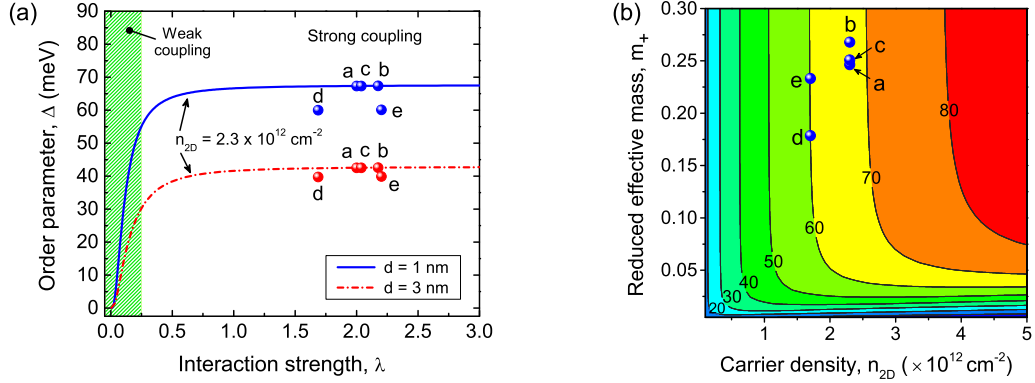
Figure 2.3: (a) The order parameter Δ as a function of the interaction strength $\lambda = ge^2 m_+/(\pi \kappa \hbar^2 k_F)$ for $d = 1.0$ nm (solid line), and $d = 3.0$ nm (dashed line) with $n_{2D} = 2.3 \times 10^{12}\,\text{cm}^{-2}$. The spheres give the order parameter for five possible e/h bilayers: a) $MoTe_2/MoS_2$, b) $MoTe_2/MoTe_2$, c) $MoTe_2/MoSe_2$, d) $MoSe_2/WSe_2$, e) $MoSe_2/MoSe_2$. In calculating Δ for specific combinations, respective effective masses and the maximum allowed 2D carrier density of the electron layer are used. The interaction strength λ for the TMD bilayers lies in the strong coupling regime. (b) Color contour plot of Δ as a function of m_+ and n_{2D} with $d = 1.0$ nm. The value in meV of each contour is labeled. The positions of the 5 bilayers of (a) are shown.

the Fermi momentum, and $m_{e(h),\sigma}$ denotes the spin and valley dependent effective masses for the electron (hole). Time reversal symmetry dictates that $m_{\alpha,\sigma} = m_{\alpha,-\sigma}$. In Eq. (2.1), $\rho_\alpha(\mathbf{q}) = \sum_{\mathbf{k}\sigma} c^\dagger_{\mathbf{k}+\mathbf{q}\sigma\alpha} c_{\mathbf{k}\sigma\alpha}$ is the total electron density for the αth layer, $V_{ee} = V_{hh} = 2\pi e^2/(\kappa q)$ is the Fourier transform of the intralayer interaction, and $V_{eh} = V_{he} = -V_{ee}e^{-qd}$ is the Fourier transform of the interlayer interaction, where κ is barrier dielectric constant, d is the thickness of the h-BN insulating spacer, and q is the momentum transfer, $q = |\mathbf{k} - \mathbf{k}'|$.

2.3 Mean Field Theory

Mean field decomposition of Eq. (2.1), gives an effective BCS-like Hamiltonian. The Green's function for the MF effective Hamiltonian can be expressed as,

$$\widehat{G}_0(k,\omega) = \frac{(\omega - \zeta_k)\widehat{\mathcal{I}} + \xi_k\hat{\tau}_3 + \Delta_k\hat{\tau}_1}{(\omega - \zeta_k)^2 - E_k^2 + i\eta}, \qquad (2.2)$$

where $\hat{\tau}_i$ is a Pauli matrix representing the layer pseudospin in the indices α and β; $\zeta_k = \hbar^2 k^2/(4m_{-,\sigma})$, $m_{-,\sigma}^{-1} = (m_{e,\sigma}^{-1} - m_{h,\sigma}^{-1})$, $\xi_k = \hbar^2(k^2 - k_F^2)/(4m_{+,\sigma})$, $m_{+,\sigma}^{-1} = (m_{e,\sigma}^{-1} + m_{h,\sigma}^{-1})$, $E_k = \sqrt{\xi_k^2 + \Delta^2}$, and Δ_k is the order parameter. When $\Delta \to 0$, the Green function in Eq. (2.2) reduces to the Green's function of the normal state. The value of the order parameter Δ is evaluated self-consistently,

$$\Delta_{\mathbf{k}} = -\frac{1}{2}\sum_{\mathbf{k}'} V_{eh}(|\mathbf{k} - \mathbf{k}'|)\frac{\Delta_{\mathbf{k}'}}{E_{\mathbf{k}'}}. \qquad (2.3)$$

In general, the order parameter can have a complicated dependence on momentum, but here we assume a translationally invariant order parameter Δ. We evaluate the normalized order parameter $\bar{\Delta} = \Delta/\epsilon_F$, as a function of the interaction strength λ and the interlayer separation d,

$$1 = \lambda \int\limits_{-\pi/2}^{\pi/2} d\phi \int\limits_{0}^{2\cos\phi} d\bar{q} \ \frac{v_D(q)}{\sqrt{\bar{\xi}_{k-q}^2 + \bar{\Delta}^2}}, \qquad (2.4)$$

where $\bar{\xi}_{k-q} = \xi_{k-q}/\epsilon_F$, $v_D(q) = e^{-k_F\bar{q}d}$, $\lambda = ge^2 m_+/(\pi\kappa\hbar^2 k_F)$, κ is the dielectric constant of the h-BN barrier (3.9), g is flavor multiplicity (two-fold for the valley degeneracy), ϕ is the angle between $\mathbf{k}$ and $\mathbf{q}$, and $\bar{q} = q/k_F$ when $k_F = \sqrt{4\pi n_{2D}/g}$. Note the appearance of the interaction parameter λ, which captures the strength of the interlayer coherence. Eq. (2.4) is evaluated self-consistently at $k = k_F$. Henceforth, we restrict our attention to the

case where the electron and hole densities are identical, $n_e = n_h = n_{2D}$. We refer to this approach as unscreened mean field (MF) and will denote it as MF.

Figure 2.3 (a) shows the dependence of the order parameter Δ as a function of the coupling parameter λ at a carrier density of $n_{2D} = 2.3 \times 10^{12} \, \text{cm}^{-2}$. Eq. (2.4) predicts that room temperature condensation is possible for $\lambda \gtrsim 0.2$. Due to the exponential dependence of d in Eq. (2.4), decreasing the interlayer separation from 3 nm to 1 nm increases the order parameter by almost a factor of two.

Figure 2.3 (a) also shows the order parameter Δ for five possible TMD bilayer structures (blue/red spheres): a) $MoTe_2/MoS_2$, b) $MoTe_2/MoTe_2$, c) $MoTe_2/MoSe_2$, d) $MoSe_2/WSe_2$, e) $MoSe_2/MoSe_2$. The order parameters for these combinations are calculated using the masses and maximum carrier densities of the n-type layer as listed in Table 2.1. Due to the higher effective masses and lower carrier densities, the values of λ for these bilayer combinations are in the strong coupling regime ($\lambda \sim 2$). Figure 2.3 (b) shows the order parameter Δ in the phase space of the reduced effective mass (m_+) and the electron density (n_{2D}). The positions of the 5 bilayer systems are also shown. As anticipated, the unscreened mean field theory indicates that exciton condensation is favorable for higher 2D carrier densities and larger effective masses.

The unscreened mean field calculations are generally valid for weak coupling regimes ($\lambda \sim 0.25$). Considering that the TMD hetero-structures fall in the strong coupling regime ($\lambda \sim 2$), the theory of exciton condensates in TMDs must be enhanced to include screening and renormalization effects. In the next section, we formulate a strong coupling theory that includes screening of the Coulomb interaction, as well as the effect of quasiparticle
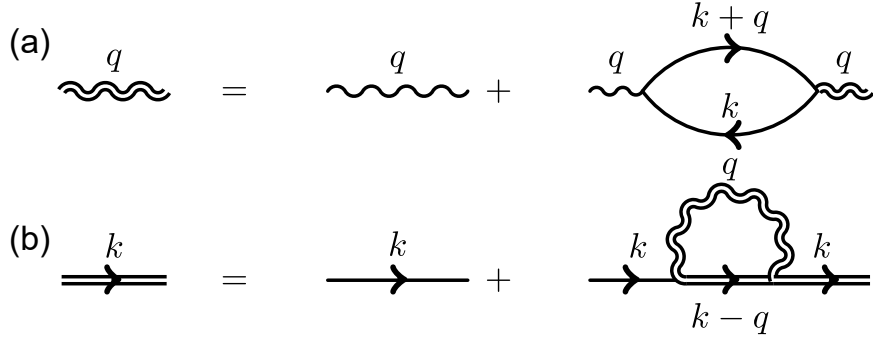
Figure 2.4: (a) Screened interaction in the RPA approximation. The Green's function used in the polarization bubble depends on the level of theory. (b) Dyson equation for the Green function in a GW approximation that includes both interlayer and intralayer screening.

renormalization.

2.4 Intermediate/Strong coupling theory

In this section, we first include RPA screening and then self-energy renormalization in a GW approximation. Results from the different levels of theory are compared.

2.4.1 Screened interlayer and intralayer interaction

Screening is treated in the random phase approximation as illustrated in Fig. 2.4 (a). At this level of theory, the solid lines in the polarization diagram represent the Green function of Eq. (2.2) which includes the coherence term Δ. Δ is calculated from Eq. (2.4) using the screened interaction self-consistently with the polarization functions.

The polarization is a 2×2 matrix with diagonal terms Π_S corresponding to same-layer polarization, and off-diagonal terms Π_D corresponding to different-layer polarization. When the top and bottom layers have the same carrier density, Π_S and Π_D can be decoupled

into even and odd channels, defined as $\Pi_\pm = \Pi_S \pm \Pi_D$ where

$$\Pi_\pm(q,\omega) = g \int \frac{d^2k}{(2\pi)^2} \left(\frac{E_{k+q} + E_k}{E_{k+q}E_k} \times \frac{E_{k+q}E_k \mp \Delta^2 - \xi_{k+q}\xi_k}{\omega^2 + i\eta - (E_k + E_{k+q})^2} \right). \qquad (2.5)$$

The particle-hole response functions depend on the order parameter Δ and also through the gapped spectrum $E_k = \sqrt{\xi_k^2 + \Delta^2}$, as seen explicitly in Eq. 2.5. The response function is evaluated self-consistently with the order parameter. From this point onward, we neglect dynamical retardation of the screened interaction and set the frequency $\omega = 0$.

The even polarization function Π_+ captures the density response to the total charge density of the gapped spectrum. Since the total response of a gapped system to a uniform shift in the potential vanishes, $\Pi_+(q \to 0) = 0$. The odd channel polarization function Π_- captures the response to a difference in the charge density of the two layers. In the $q \to 0$ limit, the odd channel polarization function approaches the density of states, $\Pi_-(q \to 0, \omega = 0) = -N(\epsilon_F)$, independent of the gap Δ.

The intralayer and interlayer density response functions needed for the calculations are $\Pi_S = (\Pi_+ + \Pi_-)/2$ and $\Pi_D = (\Pi_+ - \Pi_-)/2$ given by

$$\Pi_S(q) = g \int \frac{d^2k}{(2\pi)^2} \left(1 - \frac{\xi_{k+q}\xi_k}{E_{k+q}E_k} \right) \times \frac{-2E_k}{(E_k + E_{k+q})^2}, \qquad (2.6)$$

$$\Pi_D(q) = g \int \frac{d^2k}{(2\pi)^2} \frac{2\Delta^2}{E_{k+q}(E_k + E_{k+q})^2}. \qquad (2.7)$$

The response functions are normalized to the 2D density of states as

$$\Pi_{S(D)}(q) = -N(\epsilon_F)\, \chi_{S(D)}(q), \qquad (2.8)$$

where $N(\epsilon_F) = gm_+/(2\pi\hbar^2)$ is the density of states for the parabolic bands and $\chi_{S(D)}(q)$ are the dimensionless polarization functions.

16

The interlayer screened interaction $V_{eh}^{sc}(q)$, within the RPA, can be expressed as $V_{eh}^{sc}(q) = 2\pi e^2/(\kappa q) \cdot v_D^{sc}(\bar{q})$, where

$$v_D^{sc}(\bar{q}) = \frac{\bar{q}\left[v_D + \tilde{\lambda}\left(v_S^2 - v_D^2\right)\chi_D\right]}{1 - 2\tilde{\lambda}(v_S\chi_S + v_D\chi_D) + \tilde{\lambda}^2(v_S^2 - v_D^2)(\chi_S^2 - \chi_D^2)}. \tag{2.9}$$

Here, we define $v_S = 1/\bar{q}$, $v_D = e^{-k_F\bar{q}d}/\bar{q}$ and $\tilde{\lambda} = 2\pi\lambda$. In the limit of an unscreened potential, $v_D^{sc}(\bar{q})$ reduces to $v_D(q) = e^{-k_F\bar{q}d}$ of Eq. (2.4).

One can now include self-consistent screening in the calculation of the order parameter by replacing the bare Coulomb potential $v_D(q)$ in Eq. (2.4) with the screened interlayer interaction $v_D^{sc}(q)$, and calculate Δ in Eq. (2.4), Π_S in Eq. (2.6), Π_D in Eq. (2.7), and $v_D^{sc}(q)$ in Eq. (2.9) self-consistently. We refer to this approach as mean field with RPA screening (MF-RPA).

Electron-electron interactions not only result in screening, but they also renormalize the quasiparticle dispersion. The self-energy renormalization is affected by both the interlayer and the intralayer interactions. Similar to the screened interlayer interaction in Eq. (2.9), the screened intralayer interactions are $V_{ee}^{sc}(q) = V_{hh}^{sc}(q) = 2\pi e^2/(\kappa q) \cdot v_S^{sc}(\bar{q})$, where

$$v_S^{sc}(\bar{q}) = \frac{\bar{q}\left[v_S - \tilde{\lambda}\left(v_S^2 - v_D^2\right)\chi_S\right]}{1 - 2\tilde{\lambda}(v_S\chi_S + v_D\chi_D) + \tilde{\lambda}^2(v_S^2 - v_D^2)(\chi_S^2 - \chi_D^2)}. \tag{2.10}$$

This correctly reduces to the monolayer RPA interaction in the limit $d \to \infty$.

The order parameter is directly proportional to the interlayer screened potential v_D^{sc}. The intralayer interaction v_S^{sc} enters into the diagonal element of the self-energy which renormalizes the quasiparticle dispersion (ξ_k) and the interaction strength λ. To understand these effects, we determine the self-energy of Fig. 2.4 (b) and use it to calculate the order parameter self-consistently.

2.4.2 Self-energy correction to many-body interaction

The renormalization of both the quasiparticle dispersion and the interlayer interaction are included within a GW approximation. The self-energy illustrated in Fig. 2.5 is calculated self-consistently with the Green's function. The Green's functions used in the polarization diagram include the renormalized order parameter but ignore the mass renormalization. Only the real part of the self energy is used in the calculation of the Green's function. We refer to this approach as mean field with GW renormalization (MF-GW).

Denoting the 2×2 self-energy matrix as $\widehat{\Sigma}_c$, the full Green function matrix $\widehat{\mathcal{G}}(k, \omega)$ is given by $\widehat{\mathcal{G}}^{-1}(k, \omega) = \widehat{G}^{-1}(k, \omega) - \widehat{\Sigma}_c(k, \omega)$, where $\widehat{G}$ is the bare Green function in Eq. (2.2). Hence, the full Green function is

$$
\widehat{\mathcal{G}}^{-1} = \begin{bmatrix} \omega + i\eta - [\xi_k + \mathcal{R}(\Sigma_S)] & -\Delta_0 - \mathcal{R}(\Sigma_D) \\ -\Delta_0 - \mathcal{R}(\Sigma_D) & \omega + i\eta + [\xi_k + \mathcal{R}(\Sigma_S)] \end{bmatrix},
\tag{2.11}
$$

where Δ_0 is the gap function in the absence of the self-energy correction, and $\mathcal{R}$ denotes the real part. It is clear from Eq. (2.11) that the diagonal element Σ_S renormalizes the quasiparticle dispersion as $\xi_k \to \xi_k + \mathcal{R}(\Sigma_S)$, and the off-diagonal element Σ_D renormalizes the gap function as $\Delta_0 \to \Delta_0 + \mathcal{R}(\Sigma_D)$.

We calculate the diagonal self-energy as

$$
\Sigma_S(k, \omega - \Omega) = i \int \frac{d\Omega}{2\pi} \int \frac{d^2q}{(2\pi)^2} v_S^{sc}(q) \widehat{\mathcal{G}}_S(k - q, \omega - \Omega),
\tag{2.12}
$$

where $\widehat{\mathcal{G}}_S$ is the diagonal part of the Green's function in Eq. (2.11). We take the complex path integral over Ω in Eq. (2.12) and calculate the normalized diagonal self-energy in the
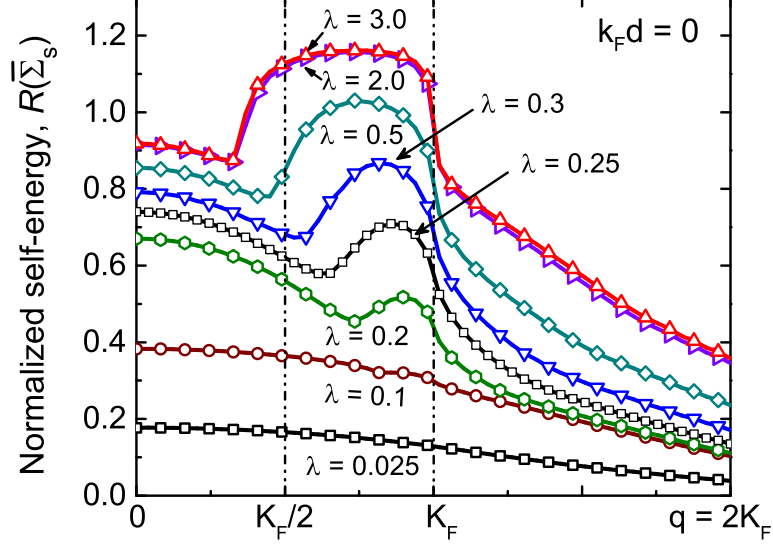
Figure 2.5: Real part of the diagonal self-energy $\Sigma_S(q)$ normalized to ϵ_F for $k_F d = 0$.

static limit ($\omega \to 0$),

$$\mathcal{R}(\overline{\Sigma}_S(\bar{k})) = -\left(\frac{\lambda}{\pi}\right) \int\limits_0^{2\pi} d\phi \int\limits_0^2 d\bar{q} \quad v_S^{sc}(\bar{q})\Theta(k_F^2 - |\mathbf{k} - \mathbf{q}|^2)$$

$$\times \quad \frac{-|\bar{\xi}_{\bar{k}-\bar{q}}^R|}{\sqrt{\left[\bar{\xi}_{\bar{k}-\bar{q}}^R\right]^2 + \bar{\Delta}^2}}, \tag{2.13}$$

where $\bar{\xi}_{\bar{k}-\bar{q}}^R = \bar{k}^2 - 2\bar{q}\bar{k}\cos\phi + \bar{q}^2 - 1 + \mathcal{R}\{\overline{\Sigma}_S(\bar{k}-\bar{q})\}$ takes into account the renormalization

of the quasiparticle dispersion. Θ is the unit step function, and $\overline{\Sigma}_S = \Sigma_S/\epsilon_F$. Since $\overline{\Sigma}_S(\bar{k})$

in Eq. (2.13) requires the evaluation of $\overline{\Sigma}_S(\bar{k}-\bar{q})$, we use analytical continuation properties,

i.e., $\mathcal{R}(\overline{\Sigma}_S(\bar{k})) = \mathcal{R}(\overline{\Sigma}_S(-\bar{k}))$. A separate calculation of the off-diagonal self-energy Σ_D is

avoided by self-consistently absorbing it in the definition of $\bar{\Delta}$,

$$1 = \lambda \int\limits_{-\pi/2}^{\pi/2} d\phi \int\limits_0^{2\cos\phi} d\bar{q} \quad \frac{v_D^{sc}(\bar{q})}{\sqrt{[\bar{\xi}_{1-\bar{q}}^R]^2 + \bar{\Delta}^2}}. \tag{2.14}$$

The value of Δ determined from Eq. (2.14) is used self-consistently in determining

19

the polarization functions Π_S and Π_D and thus the screened interactions v_D^{sc} and v_S^{sc}. The dispersion represented by ξ_k used in the calculation of the polarization functions is the bare dispersion in the absence of Σ_S. Thus, the Green function lines in the polarization bubble are partially self-consistent in that they include the effect of the self-energy on the off-diagonal order parameter, but they do not include the effect of mass renormalization. Eqs. (2.6), (2.7), (2.9), (2.10), (2.13), and (2.14) are the set of self-consistent equations that are solved to obtain Δ.

To understand the relative contribution of the self-energy correction, we plot the normalized $\mathcal{R}(\Sigma_S)$ in Fig. 2.5 for different values of λ. In the weak coupling regime ($\lambda < 0.2$), the self-energy is only 20% – 60% of the Fermi energy. However, at the onset of intermediate/strong coupling region ($\lambda \geq 0.5$), the self-energy becomes equal to or larger than the Fermi energy. This illustrates the importance of the self-energy correction in the strong coupling regime.

2.4.3   Discussion

In this section, we discuss the MF-GW results and compare them with the MF and MF-RPA predictions. Theoretically, the most favorable condition of condensation occurs at vanishing interlayer distance, *i.e.* $k_F d \to 0$. Considering this optimum condition, Fig. 2.6 summarizes the three different levels of theory. For the MF calculation the gap increases monotonically with interaction strength. In this case, moderate interlayer interaction ($\lambda > 0.2$) leads to room temperature condensation. The effect of RPA screening (MF-RPA) on the order parameter depends on the relative strength of λ. In the weak
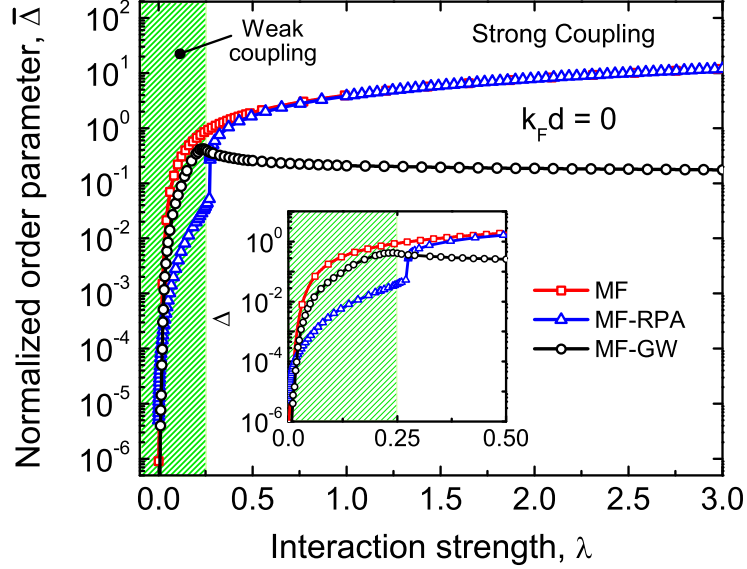
Figure 2.6: Normalized order parameter as a function of the effective interaction strength λ, obtained from MF, MF-RPA, and MF-GW theory for $k_F d = 0$. The inset shows the region near $\lambda = 0.25$

.

coupling regime ($\lambda \approx 0.25$), screening reduces the interlayer coherence. In the intermediate/strong coupling regime, screening cannot compete with the interlayer interaction and Δ follows the unscreened gap function. The discontinuity in the MF-RPA curve near $\lambda = 0.25$ is similar to the discontinuity observed and discussed by Neilson et al. [160] When both interlayer and intralayer screening are included as a self-energy correction (MF-GW), the interlayer coherence is strongly reduced for interaction strengths above 0.25. As $\lambda \to 0$, the MF-GW theory and the MF theory coincide. The reason is apparent from Fig. 2.5, which shows that self-energy correction remains negligible up to $\lambda \sim 0.1$.

Figure 2.7 is a color contour plot of Δ as a function of m_+ and n_{2D} determined from the MF-GW theory. The positions of the same bilayer structures from Fig. 2.3 are shown. A comparison of the $m_+ - n_{2D}$ phase diagram in Fig. 2.7 with that of the MF

result in Fig. 2.3 (b) shows that MF-GW theory predicts trends that are qualitatively different from the MF theory. For a reduced mass greater than 0.05, the order parameter of MF theory is nearly independent of the mass and is moderately dependent on the density, changing by a factor of ~ 3 as the density increases an order of magnitude from 5×10^{11} cm^{-2} to 5×10^{12} cm^{-2}. The order parameter of MF-GW theory has the same moderate dependence on the density, but it is exponentially dependent on the mass. For a density of 2×10^{12} cm^{-2}, the order parameter decreases 5 orders of magnitude as the mass increases from 0.05 to 0.3. Also, the functional dependence of the order parameter on the mass is qualitatively different. In both theories, the order parameter rapidly increases as m_+ increases from zero. In MF theory, the order parameter saturates and remains constant for $m_+ \gtrsim 0.1$. In MF-GW theory, the order parameter peaks at $m_+ \sim 0.025$ and then exponentially decays as m_+ increases. For MF theory, the conditions for maximum Δ occur at the upper right corresponding to high density and high mass. For MF-GW theory, the conditions for maximum Δ occur at the lower left corresponding to low density and low mass. The MF-GW theory exponentially reduces the magnitude of the order parameter for masses corresponding to those of the 2D bilayers. The heavy masses of the 2D materials which increase the order parameter in MF theory, decrease the order parameter in MF-GW theory.

As shown in Fig. 2.6, *interlayer* screening calculated self-consistently in the presence of a condensate has little effect on the order parameter in the strong coupling limit. Renormalization due to *intralayer* screening has a large effect. We conclude that, in the strong coupling limit, the *intralayer* interactions determine the overall trends of the order

parameter.

The transition temperature, T_c for the exciton condensate can be calculated from the well-known result of the BCS theory of superconductivity [9], $k_B T_c \sim 0.57\Delta$. Using the largest value of $\Delta = 2~\mu$eV from point d in Fig. 2.7 gives a value of $T_c = 13~\mu$K. At larger values of Δ, or equivalently at higher temperatures, the transition will be of the Kosterlitz-Thouless (KT) type [113]. The KT-transition temperature T_{KT} can be calculated from the superfluid density, $n_s(T)$ and is given by $k_B T_{KT} = \pi\hbar^2/(2m)n_s$. It has been shown in Ref. [155], that the upper bound of the KT transition for both parabolic and Dirac bands is $k_B T_{KT} < 0.1\epsilon_F$, a property of the normal state. Therefore, KT transition will be only relevant for exciton gaps $\Delta \sim 0.1\epsilon_F$.

We now comment on effects not included in the above calculations, namely dynamical retardation effects and vertex corrections. To our knowledge only a handful of studies have accounted for the dynamical nature of screening. In Ref. [200], the dynamical retardation effects on the screening along with the simultaneous reduction in screening accompanied by the appearance of inter-layer coherence, have been studied in the weak coupling limit. These effects lead to an increase in the strength of the order parameter Δ, when compared to static screening partly due to larger phase space. We expect a similar trend in the strong coupling limit. The effects of the vertex correction on exciton condensates remains an open theoretical question.
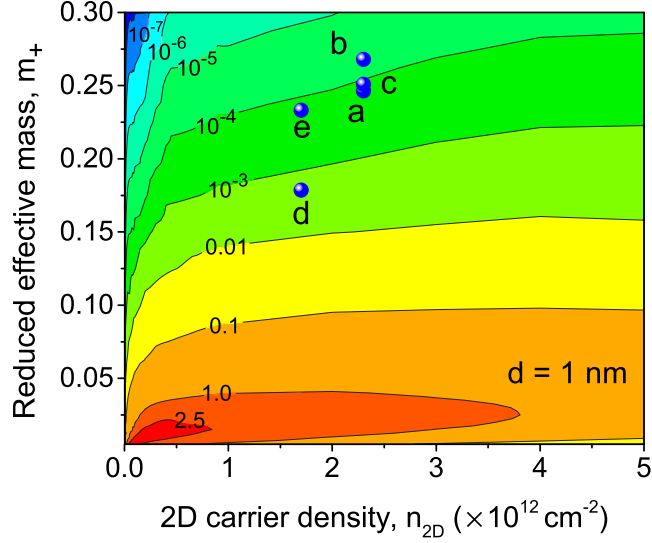
Figure 2.7: Color contour plot of Δ as a function of m_+ and n_{2D} with $d = 1.0$ nm calculated with MF-GW theory. The value in meV of each contour is labeled. The positions of the 5 bilayers from Fig. 2.3 (a) are shown.

2.5 Conclusion

Exciton condensation is analyzed as a function of the coupling strength with a focus on the strong coupling regime, which is the regime of TMD bilayer electron-hole systems. Three different levels of theory are considered. Starting from unscreened mean field theory, RPA screening and self-energy renormalization in a *GW* approximation are included. A mean field calculation with an unscreened Coulomb potential predicts a room temperature exciton condensate. The inclusion of RPA screening in the interlayer interaction reduces the order parameter in the weak coupling regime, but it has little effect in the strong coupling regime, and a room temperature condensate is still predicted. The inclusion of the effects of both the interlayer and intralayer interactions through a self-energy correction to the quasiparticle dispersion and the order parameter in a *GW* approximation reverses the trends

predicted from the MF and MF-RPA theories. The MF-GW theory favors low density and low mass for maximizing the magnitude of the order parameter. The heavy masses of the TMD materials that increase the order parameter in MF and MF-RPA theories, reduce the order parameter in the MF-GW theory. In the strong coupling regime, *intralayer* screening has a large impact on the magnitude of the order parameter and its functional dependencies on effective mass and carrier density.

Chapter 3

Ab initio thermal conductivity of misoriented bilayer graphene

3.1 Introduction

Interlayer misorientation in the bilayer graphene (BLG) system has attracted significant attention due to its effect on the electronic dispersion [136, 121, 196, 154, 149, 84, 146, 193, 107] including the magic angles that give rise to flat bands and superconductivity [31, 32], the phonon dispersion [162, 187, 33, 81, 37, 30, 215], and the thermal properties [165, 123, 122].

Observation of high thermal conductivity of graphene has motivated numerous experimental and theoretical discoveries over the past decade, and paved the way to engineering new thermal management devices [7, 234], thermal phase change devices [186] and thermal interface material composites [194, 195, 99]. The room temperature (RT) thermal

conductivity of single layer graphene (SLG) is approximately 3000–5000 W/m·K [8], while the room temperature thermal conductivity of few layer graphene (FLG) ranges from 1300 W/m·K to 2800 W/m·K [70]. There are many factors that influence the phonon dispersion, heat capacity, and thermal conductivity of bilayer graphene, such as vacancies, chirality, isotope, wrinkles, number of layers, etc. Among them, the effect of interlayer rotation on the phonon properties and the resulting thermal conductivities in misoriented bilayer graphene (m-BLG) is least understood, and it is the focus of this work.

Experimentally, several groups have identified distinct Raman signatures, arising from the m-BLG regions of the grown BLG samples [179, 78, 33, 189, 82, 183]. There are a number of theoretical investigations to explain the origin and evolution of these peaks [187, 37, 183, 122]. The theoretical calculations for m-BLGs are based on parametric atomic interaction models optimized for graphite or graphene crystals. Ab initio phonon dispersion calculations for misoriented bilayer graphene are absent in the literature, primarily because of the numerical difficulty associated with the large unit cells required to describe the m-BLG structures [82].

The effect of misorientation on the in-plane thermal conductivity of m-BLG is an open theoretical question [165, 123, 122]. Recent optothermal Raman measurements [123] found that the thermal conductivity of BLG goes down from ∼1892 W/m·K to ∼1422 W/m·K (∼1.3×) at room temperature with a misorientation angle estimated to be ∼ 32°. At high temperature, the reduction in thermal conductivity was less pronounced (∼1.1×). A hypothesis to explain the reduction is that the reduced Brillouin zone of the misoriented bilayers allows increased phonon-phonon umklapp scattering [123]. This hypothesis is con-

sistent with the results from nonequilibrium molecular dynamics calculations showing that the thermal conductivity scales with the commensurate lattice constant rather than the rotation angle [122]. There have been no DFT level calculations of the phonon modes and thermal conductivity as a function of interlayer misorientation.

In this work, we use density functional theory (DFT) to calculate the lattice thermal conductivity of misoriented bilayer graphene for rotational angle of $21.78°$. We explicitly calculate the ab initio phonon dispersion before and after misorientation, as well as calculate the ab initio phonon scattering lifetime in m-BLG using DFT enabled phonon Boltzmann transport theory. Sec. 3.2 describes the structure, lattice constants, and unit cells of misoriented bilayer graphene. The details of the DFT and BTE calculations are described in Sec. 3.3. Sec. 3.4 discusses the results of the thermal conductivity calculations, phonon dispersion, lifetime, and scattering processes, whereas Sec. 3.5 concludes the findings.

3.2 Misoriented bilayer graphene

We consider the misoriented bilayer graphene system as shown in Fig. 3.1, where the bottom layer is rotated with respect to the top layer by an angle θ. The relative twisting between monolayers breaks the symmetry of the Bernal stacked AB-BLG and generates a superlattice structure, exhibiting a moiré pattern [30]. These rotations create a θ-dependent $\mathbf{q}$-wavevector for phonon modes. Formation of a superlattice also changes the phonon dispersion by zone-folding, and hence modifies the kinematics of phonon-phonon scattering [19]. As a result, interlayer misorientation can significantly affect the thermal properties in a m-BLG system [37].
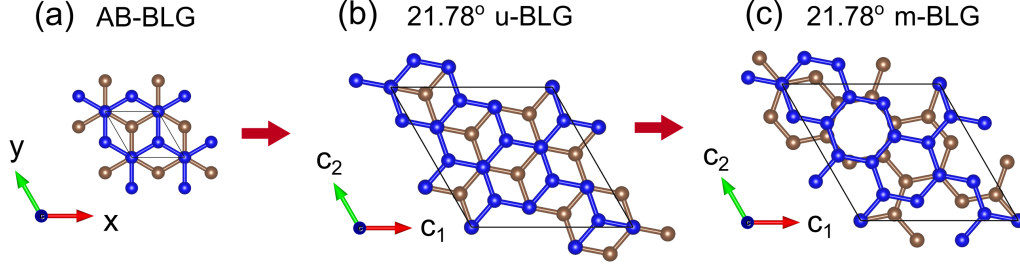
Figure 3.1: Atomic configuration of (a) 4-atom AB bilayer graphene, (b) 28-atom 21.78°
unrotated BLG (u-BLG), (c) 28-atom 21.78° misoriented BLG (m-BLG). The blue (gray)
atom are from the top (bottom) layer of the BLG.

To ensure the periodicity of the atomic configurations in the presence of mis-
orientation, only certain commensurate rotational angles (θ) are allowed, as given by the
following expression [122]

$$\cos\theta = \frac{n^2 + 4nm + m^2}{2(n^2 + nm + m^2)}, \tag{3.1}$$

where the m and n are the non-negative integers ($m \leq n$). The commensurate lattice
vectors are $\mathbf{c_1} = n\mathbf{a_1} + m\mathbf{a_2}$ and $\mathbf{c_2} = -m\mathbf{a_1} + (m+n)\mathbf{a_2}$, where $\mathbf{a_1}$ and $\mathbf{a_2}$ are the unit
cell vectors of AB-BLG.

Using the vectors $\mathbf{c_1}$ and $\mathbf{c_2}$, we create a supercell of AB-BLG for the commensu-
rate angle $\theta = 21.78°$, and denote them as u-BLG (unrotated BLG), as shown in Fig. 3.1
(b). Subsequently, the bottom monolayer (gray atoms) of u-BLG is rotated with respect to
the top layer (blue atoms) by θ, to obtain the m-BLG structures shown in Fig. 3.1 (c). From
the structural point of view, the u-BLG structure is just a large supercell of AB-BLG. On
the other hand, the m-BLG structure is essentially the same AB-BLG supercell as u-BLG,
but with one monolayer misoriented by $\theta°$. Hence, both u-BLG and m-BLG structures have
the same lattice constants and same number of atoms (N = 28).

The purpose of creating the u-BLG structure is to allow easy comparison of the

Table 3.1: DFT calculated atomic and vibrational properties of u-BLG and m-BLG for the misorientation angle of $21.78°$: interlayer distance ($d_\perp$), and phonon frequencies of shearing (TA_2/LA_2), breathing (ZA_2), out-of-plane optical (ZO), transverse optical (TO), longitudinal optical (LO) modes.

	$d_\perp$	TA_2/LA_2	ZA_2	ZO	TO	LO
	(Å)	(cm^{-1})	(cm^{-1})	(cm^{-1})	(cm^{-1})	(cm^{-1})
AB-BLG	3.25	28.55	91.83	866.9, 869.5	1567	1573
u-BLG	3.26	28.38	93.03	866.5, 868.9	1568.1	1572.7
m-BLG	3.36	2.31	87.69	868.3 (2)	1571.8	1572.2

thermal conductivity and phonon dispersion with those from the m-BLG structure. Since the two structures have the same lattice constants and the same number of atoms, their phonon dispersions lie within the same irreducible Brillouin zone. A comparison of the phonon dispersions of these two structures automatically decouples the trivial effects of zone folding from the effects due to changes in the interlayer interaction arising from misorientation.

3.3 Computational details

The phonon frequency, phonon velocity, and phonon transition probabilities in an atomic system depend on the accurate calculations of the second-order (harmonic) and third-order (anharmonic) interatomic force constants (IFCs). To obtain all of the interatomic interactions, we use density functional theory, as implemented in Vienna Ab-initio Simulation Package (VASP) [115, 114], with projector-augmented-wave (PAW) pseudopotentials [14] and the Perdew-Burke-Ernzerhof formalism [175]. The van der Waals interac-

tions between the graphene layers are included by considering the semi-empirical correction of Grimme-D2 [77]. To relax the atomic structures, a converged k-point grid of $16\times16\times2$, $10\times10\times2$, and $10\times10\times2$ are used for AB bulk graphite, $21.78°$ unrotated graphite, and $21.78°$ misoriented graphite, respectively. All structures are relaxed until the forces on the atom is less than 10^{-5} eV/Å and the energy convergence reaches 10^{-8} eV. Following the typical procedure of monolayer simulations in DFT [45], a converged vacuum distance of 16 Å is added to the relaxed bulk graphite structure to form the bilayer geometry. The additional vacuum is necessary to avoid spurious interaction with the periodic images. The atomic positions of each bilayer structure are subsequently relaxed, while the convergence of energy is checked at each simulation step. The in-plane C-C bond length of the u-BLG and m-BLG structure remain almost same (1.423 Å), whereas the interlayer C-C bond length $(d_\perp)$ changes by ~0.1 Å, as shown in Table 3.1.

The second-order interatomic force constants are calculated within a real-space supercell approach by using the Phonopy package [206]. For the phonon dispersion of the AB-BLG, $21.78°$ u-BLG and $21.78°$ m-BLG, a supercell size of $5\times5\times2$, $3\times3\times1$ and $2\times2\times1$ is used, with a **k**-grid of $5\times5\times2$, $4\times4\times1$ and $4\times4\times1$, respectively. The phonon density of states (DOS) and other thermodynamics properties, *e.g.* heat capacity are calculated using the 2nd-order IFCs for each structure.

The thermal conductivity tensor is calculated from the Boltzmann phonon transport equation [129, 249],

$$\kappa_{\alpha\beta} = \frac{1}{K_B T^2 NV} \sum_{\boldsymbol{\lambda}} f_{\boldsymbol{\lambda}}^0 (f_{\boldsymbol{\lambda}}^0 + 1)(\hbar\omega_{\boldsymbol{\lambda}})^2 v_{\boldsymbol{\lambda}}^\alpha v_{\boldsymbol{\lambda}}^\beta \tau_{\boldsymbol{\lambda}}, \qquad (3.2)$$

where $\boldsymbol{\lambda} = \{\lambda, \mathbf{q}\}$ indicates both the phonon mode λ and the wavevector $\mathbf{q}$, $\hbar\omega_{\boldsymbol{\lambda}}$ is the

phonon energy, $f_{\boldsymbol{\lambda}}^0$ is the equilibrium Boltzmann distribution, $v_{\boldsymbol{\lambda}}$ is the group velocity, and $\tau_{\boldsymbol{\lambda}}$ is the phonon-phonon scattering lifetime. N is the number of uniformly spaced $\mathbf{q}$ points in the irreducible Brillouin zone. V is the volume of the BLG unit cell having thickness $2h$, where h is taken to be the equilibrium van der Waals distance $(\mathrm{d}_\perp)$ obtained from the DFT relaxation steps. The scattering lifetime $\tau_{\boldsymbol{\lambda}}$ in Eq. (3.2) can be written as [148], $\tau_{\boldsymbol{\lambda}} = \tau_{\boldsymbol{\lambda}}^0 (v_{\boldsymbol{\lambda}}^\beta + \Delta_{\boldsymbol{\lambda}})$ where $\tau_{\boldsymbol{\lambda}}^0$ is the lifetime obtained under relaxation time approximation (RTA), and $\Delta_{\boldsymbol{\lambda}}$ is a correction to the RTA value obtained by solving the BTE in an iterative manner.

The lowest-order anharmonic scattering process that affects thermal conductivity is three-phonon scattering [19]. Due to the anharmonicity of the interatomic potential, the three-phonon scattering process is inelastic and provides an intrinsic limitation on the thermal conductivity. Other, extrinsic scattering mechanisms include scattering from defects, impurities, isotopes, and boundaries. These additional scattering mechanisms also give rise to mode-dependent scattering lifetime. The total phonon-phonon scattering rate $(1/\tau_{\boldsymbol{\lambda}})$ results from all of these processes. We neglect isotope scattering, since the anharmonic phonon-phonon scattering rate dominates over the isotope scattering rate beyond a few tens of Kelvin [21]. We also ignore boundary scattering [118], since we are interested in large samples in which the thermal conductivity is dominated by transport through the bulk rather than the edges. The higher-order scattering processes, e.g. the four-phonon scattering [16], are much more complex and difficult to numerically model at a DFT level of theory with the large supercells under consideration, and therefore are beyond the scope of this work.

The three-phonon scattering process, where one phonon decomposes into two phonons and vice versa, must satisfy both energy conservation, $\omega_{\boldsymbol{\lambda}} \pm \omega_{\boldsymbol{\lambda'}} = \omega_{\boldsymbol{\lambda''}}$, and quasi-momentum conservation, $\mathbf{q} \pm \mathbf{q'} = \mathbf{q''} + \mathbf{G}$, where $\mathbf{G}$ is the reciprocal lattice vector. The plus (minus) sign indicates the phonon absorption (emission). $\mathbf{G}$ is zero for normal scattering (N process), and non-zero for umklapp scattering (U process) [21]. The U process tries to relax the phonon distribution $f_{\boldsymbol{\lambda}}$ to an equilibrium distribution $f_{\boldsymbol{\lambda}}^0$ (resistive process), whereas the N-process shifts the distribution to a displaced distribution $f_{\boldsymbol{\lambda}}^*$. [148]

To obtain the three-phonon scattering and *ab initio* thermal conductivity, we calculate the third-order interatomic force constants for AB-BLG, $21.78°$ u-BLG and $21.78°$ m-BLG. Supercell structures of $4\times4\times1$, $2\times2\times1$, and $2\times2\times1$ size are used to calculate the anharmonic IFCs, which generates 220, 240 and 564 atomic configurations for AB-BLG, u-BLG and m-BLG structures, respectively. The total phonon scattering rate is obtained from the anharmonic transition rate $\Gamma_{\boldsymbol{\lambda\lambda'\lambda''}}^{\pm}$ as [50], $1/\tau_{\boldsymbol{\lambda}} = \frac{1}{N} \sum_{\boldsymbol{\lambda'\lambda''}} [\Gamma_{\boldsymbol{\lambda\lambda'\lambda''}}^{+} + \frac{1}{2}\Gamma_{\boldsymbol{\lambda\lambda'\lambda''}}^{-}]$. Γ depends on the scattering matrix element $V_{\boldsymbol{\lambda\lambda'\lambda''}}^{\pm}$, which is calculated from the third-order IFCs [218]. Atomic interactions up to 5th-nearest neighbor are considered. The phonon BTE is solved using both the relaxation time approximation (RTA) and the full iterative approach, as implemented in the ShengBTE package [126, 130]. The convergence of κ for a certain $Nq\times Nq\times1$ integration grid is tested with a precision of 10^{-5} difference between the iterative steps. Moreover, the convergence with respect to different $Nq\times Nq\times1$ mesh-grid is also checked. Note that, a preliminary lifetime calculation of m-BLG has been reported by us earlier for $15\times15\times1$ $\mathbf{q}$-grid [122]. However, in this work, our analysis is based on $27\times27\times1$ $\mathbf{q}$-grid calculation and with better numerical criteria, which gives a converged
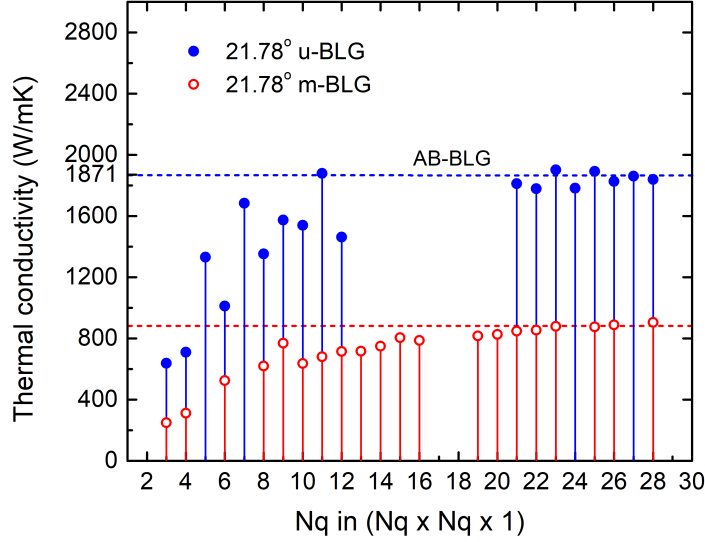
Figure 3.2: Convergence of thermal conductivity calculation for different K-point grid at T = 300 K.

thermal conductivity, for both u-BLG and m-BLG structures (see Fig. 3.2). The effect of the Born effective charge is ignored, since the non-analytical corrections to the phonons are negligible in the BLG system.

3.4 Results and Discussions

3.4.1 Thermal conductivity of m-BLG system

Figure 3.3 shows the *ab initio* thermal conductivity (κ) of AB-BLG, 21.78° u-BLG and 21.78° m-BLG. The calculated κ for u-BLG (1839.3 W/m·K at RT) is very close to κ of AB-BLG (1871.3 W/m·K at RT), which is expected given that the 21.78° u-BLG is just a commensurate supercell of AB-BLG unit-cell. This also agrees well with prior theoretical calculations of κ for AB-BLG (1880 W/m·K at RT) [109]. As evident from Fig. 3.3, interlayer misorientation reduces the room-temperature thermal conductivity by a factor of
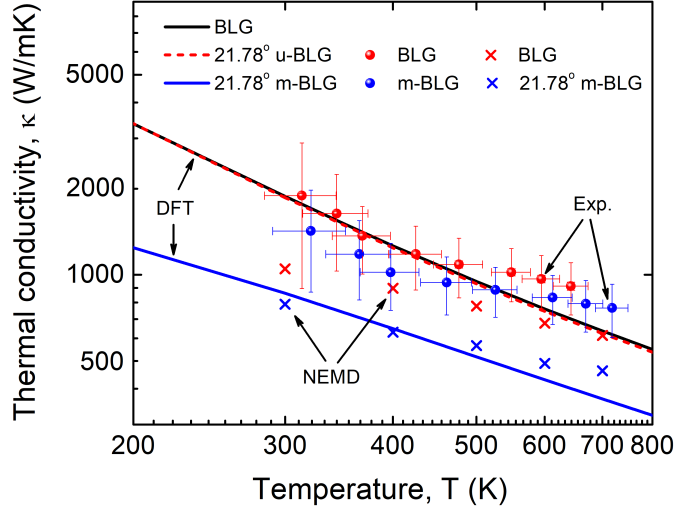
Figure 3.3: Lattice thermal conductivity of AB-BLG, 21.78° u-BLG, and 21.78° m-BLG, calculated from DFT and phonon BTE. The circle symbols are experimental thermal conductivity from the optothermal Raman experiment [123], and the cross symbols are from NEMD simulations [122].

2.2. Moreover, thermal conductivity exhibits Eucken's law of T^{-1} dependence [55] at high temperature, for both u-BLG and m-BLG cases, indicating that the umklapp scattering is the dominating process at elevated temperature. The calculated thermal conductivities are numerically well-converged with respect to the integration grid (Fig. 3.2). Prior NEMD simulations [122] (cross symbols in Fig. 3.3) also exhibit 1.3∼1.4 times reduction in κ with rotation at all temperatures, although the NEMD thermal conductivity of AB-BLG is very low (1045 W/m·K at RT), compared to the DFT values (1871.3 W/m·K) and experimental reports (1892 W/m·K) [123].

We also compare the *ab initio* calculation with experimental reports of κ for the twisted and suspended BLG samples [123]. As seen in Fig. 3.3, the experimental κ matches well with the DFT calculated BLG and u-BLG cases, except at high temperature limit. On

35

the other hand, the experimental κ of m-BLG is almost similar in range when compared to that of u-BLG, contrary to the DFT prediction. The mismatch between the experiment and simulation might come from the large systematic error arising from the finite spectral resolution in optothermal Raman technique, as well as the uncertainty in identifying the accurate temperature of the sample [123] (error-bar in Fig. 3.3). At high temperature limit, the experiments show that the thermal conductivity of m-BLG is very close to that of u-BLG (within 13%). DFT calculation also suggests that the relative difference between u-BLG and m-BLG will be less pronounced at high temperatures, although not as insignificant as seen in experiment.

To explain why the thermal conductivity goes down with misorientation, we need to calculate the phonon energy dynamics and phonon scattering distribution in the twisted bilayer graphene system. Thermal conductivity is an integrated function of the phonon dispersion ($\omega_{\boldsymbol{\lambda}}$), phonon velocity ($v_{\boldsymbol{\lambda}}$) and phonon-phonon scattering lifetime ($\tau_{\boldsymbol{\lambda}}$). Typically, the energy and velocity modification of the low-energy acoustic and quasi-acoustic phonon modes have crucial implications on the thermal properties of materials [100]. On top of that, the phonon-phonon scattering is another important factor limiting the intrinsic thermal conductivity, even at moderate temperature. To our knowledge, no ab initio studies of phonon energetics and scattering dynamics, comparing solely the effect of misorientation, have been reported. In the next sections, using density functional theory and phonon BTE formalism, we will explore each of these contributing factors. We will also explain the underlying nature of thermal conduction in m-BLG system.

3.4.2 Phonon dispersion of m-BLG

We first consider the effect of misorientation on the phonon dispersion. Figure 3.4 (a) shows the phonon dispersion of u-BLG (solid line) and m-BLG (dash line) for $\theta = 21.78°$, focusing on the low-frequency region up to 500 cm^{-1}, which is the primary energy-scale responsible for thermal conduction (see Fig. 3.6 for the full-range dispersion). From the comparative dispersions, it is clear that misorientation significantly affects the quasi-acoustic mode LA$_2$/TA$_2$. At Γ point of the BZ, the frequency of the LA$_2$/TA$_2$ mode of u-BLG is around 28 cm^{-1} (see Table 3.1). However, after rotation, the frequency of this mode reduces to $\sim$2 cm^{-1}.

The doubly-degenerate LA$_2$/TA$_2$ phonon mode is characterized by an in-plane sliding motion, where the top and bottom layers slide out-of-phase with respect to each other. As seen in Fig. 3.4 (b), in both u-BLG and m-BLG cases, the displacement is an optical shear mode in which the two layers slide in opposite directions. However, the energy cost associated with such sliding motion reduces significantly in m-BLG. The reason is apparent from the presence of the moiré pattern in m-BLG system. In u-BLG, half of C atoms (7 out of 14) in the top layer are directly on top of another C atom of the bottom layer. On the contrary, in m-BLG, only one atom on the top layer is directly on top of another C atom from bottom layer. Hence, for the sliding motion in m-BLG, only one C-C interlayer bond has to be displaced. Moreover, the sliding motion in m-BLG moves half of the C atoms closer to one another, while shifts the other half away from one another. The compensating nature of such sliding motion is the reason behind one-order reduction of LA$_2$/TA$_2$ phonon frequency in m-BLG. The slight increase in the interlayer distance with
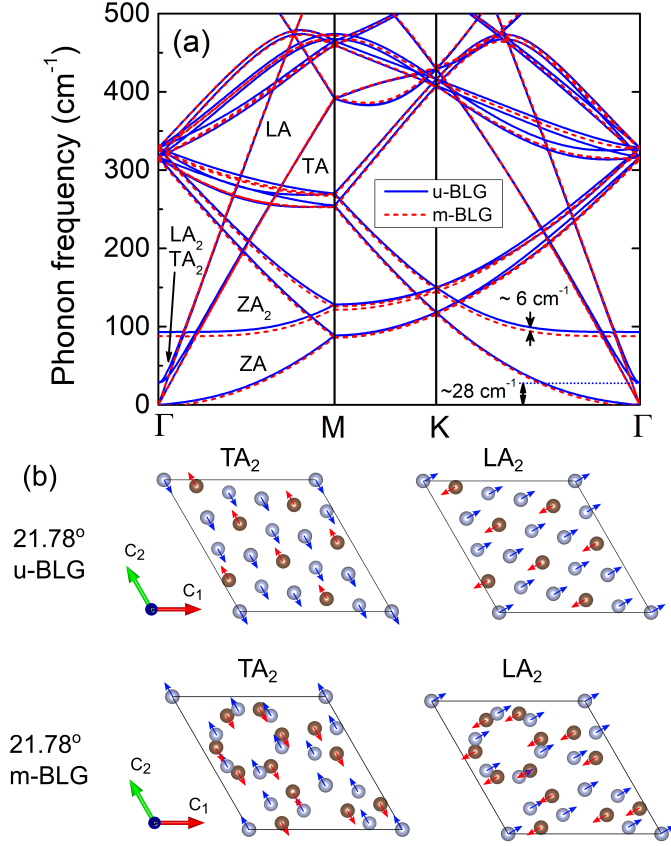
Figure 3.4: Phonon dispersion of unrotated bilayer graphene (solid line) and misoriented bilayer graphene (dash line) of $\theta = 21.78°$, in the low frequency region; (b) atomic vibrations of quasi-acoustic phonon modes (TA_2/LA_2), before and after rotation.

misorientation (see DFT values in Table 3.1) is also consistent with the softening of this shearing mode.

The quasi-acoustic modes TA_2/LA_2 in u-BLG are not captured in non-equilibrium molecular dynamic (NEMD) simulations [183, 122]. An empirical model, with a Born-von Karman potential for the in-plane C-C interaction and either a spherical potential (BVK-Sph) [165] or a Lennard-Jones potential (BVK-LJ) [37] for the interlayer interaction, does capture the TA_2/LA_2 mode [37]. However, the ability of the empirical model to predict the

mode frequency as a function of rotation angle is uncertain, since the force constants are parameterized for the unrotated crystal structure. Unlike DFT, the empirical force-constant model finds that the quasi-acoustic frequencies are little affected by the misorientation. For AB-BLG, the model-predicted shearing mode frequency is 13.4 cm^{-1}, whereas for m-BLG, the frequency rather increases to 14.7 cm^{-1} [37]. An earlier study [94] using an empirical force constant model found the LA$_2$/TA$_2$ frequency of AB-BLG to be 30.2 cm^{-1}, which is closer to the values from our DFT calculations (Table 3.1). Symmetry analysis shows that the LA$_2$/TA$_2$ mode of AB-BLG will be Raman active [94]. Raman signature of such shearing mode in AB-BLG has also been reported around 31 cm^{-1} in recent experiments [205], which is also consistent with our DFT predicted values. However, accurate Raman experiment identifying the shearing mode in m-BLG system is not available yet [145, 82, 183].

Going beyond the acoustic and quasi-acoustic phonon branches, many of the optical phonon branches show slight shift with rotation. One such mode is the breathing mode (ZA$_2$), which is characterized by the out-of-phase rigid motion of the top and bottom graphene layers. Since the interlayer vdW distance increases with misorientation, ZA$_2$ frequency goes down by ~ 6 cm^{-1} with rotation (Table 3.1), which can be used as a signature of twisting present in the system. The empirical models also predicts similar red shift of ZA$_2$ mode [37]. As seen in Fig. 3.4 (a), some of the other optical modes above ZA$_2$ also exhibit frequency change or breaking of degeneracy. This can be attributed to the modified interlayer interaction between the phonon branches of the top and bottom monolayer, as they rotate with respect to one another. The atomic vibrations show that these phonon modes are actually hybrid ZA$_2$ mode, characterized by their in-phase and
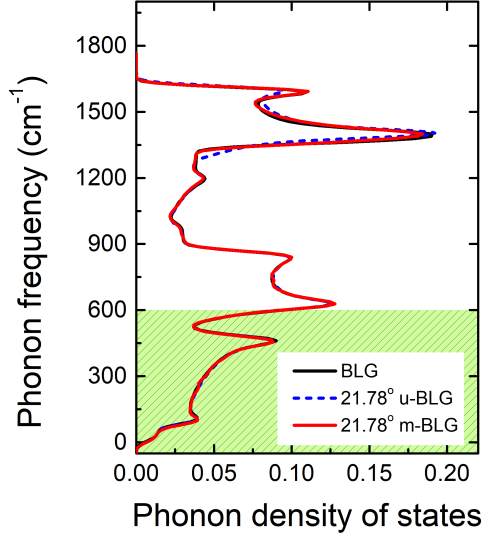
Figure 3.5: Phonon density of states of u-BLG and m-BLG for 21.78° rotations, when normalized by the atom number in the unit-cell. Calculated phonon DOS is little affected by rotation, except the high-energy region beyond 1200 cm^{-1}.

out-of-phase ripple-like motion of monolayer surface. The higher optical modes after 500 cm^{-1} shows very little effect of misorientation, expect the modes around 1300~1600 cm^{-1} (see Fig. 3.6 a, b). However, these high-energy optical modes are irrelevant from the point of thermal excitation and heat conduction.

From the phonon dispersion calculations, it is clear that, except the modification of quasi-acoustic modes (TA$_2$/LA$_2$) around Γ and the slight shift of certain low-energy modes, the phonon dispersions remain almost invariant to misorientation, specifically when considered over the whole BZ. To see how these changes can affect the phonon dynamics, when integrated over the whole BZ, we have calculated the phonon density of states. We find that the integrated phonon density of states do not change much with misorientation (see Fig. 3.5 a), which agrees with prior empirical models [37]. Since the thermal conductivity

is also an integrated quantity of the BZ, we can conclude that the changes in phonon modes are not significant enough to affect the thermal conductivity. However, to explore how these modification can affect the velocity of the heat-carrying channels inside the BZ, we will calculate the phonon velocity distribution in the next section.

3.4.3 Phonon velocity distribution in m-BLG

One of the important parameters that determines thermal conductivity is the phonon group velocity v_λ^x. As evident from Eq. (3.2), thermal conductivity (κ) is directly related to $(v_\lambda^x)^2$ when the thermal gradient is along the x direction. Figure 3.6 (a)-(b) show the x-component of the phonon group velocity as a color-map over the dispersion lines. The LA mode has almost two-times higher velocity than that of TA mode, making it the dominant conduction channel, whereas the group velocities for out-of-plane ZA mode is almost one order lower than LA mode velocity. The velocities of the zone-folded hybrid modes below 600 cm^{-1} are also in the same order as the TA mode, signifying that their contribution to κ is as important as TA mode. Note that, around 300 cm^{-1}, interlayer rotation decreases the velocity of some optical modes, specifically along $\Gamma - M$ and $\Gamma - K$ direction.

To understand the overall effect of the phonon velocity changes, specifically on the heat carrying channels distributed in the irreducible Brillouin zone, we have calculated the absolute phonon velocity ($|v|$) for each $\mathbf{q}$ point in the BZ, as shown in Fig. 3.7 (c). We find that there are mainly three velocity channels: high-velocity of LA-like modes ($|v| = 16 \sim 21$ km/s), medium-velocity of TA-like modes ($|v| = 8 \sim 14$ km/s), and low-velocity
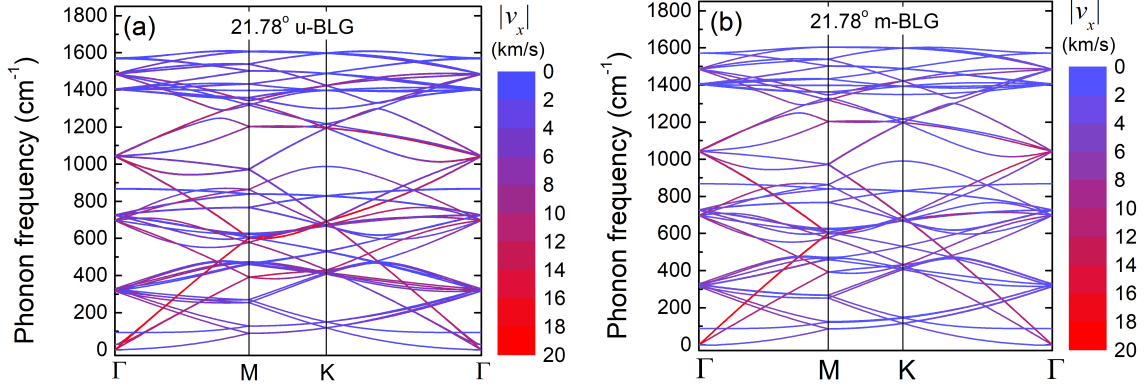
Figure 3.6: Phonon group velocity along the C_1 direction, color-coded over the dispersion as indicated by the sidebars: (a) 21.78° u-BLG, (b) 21.78° m-BLG.

quasi-acoustic and hybrid optical modes ($|v| = 0 \sim 8$ km/s). Around $30 \sim 100$ cm^{-1}, several modes near LA-like and TA-like modes have $1.1 \sim 1.3$ times lower velocity than the corresponding modes in m-BLG, where these modes in u-BLG arise from LA$_2$/TA$_2$ branches. Although this may seem that the m-BLG will have higher thermal conductivity, the number of such heat channels is very small. Significant velocity redistribution happens in m-BLG around low-velocity region between $250 \sim 450$ cm^{-1}, arising from the zone-folded modes. Reduction of velocity suggests m-BLGs will have lower thermal conductivity. Although the velocity of these modes can show almost one-order reduction, their overall effect is insignificant, considering that the velocity is already much low, even before misorientation. The velocity distribution suggests that there is an opposite but compensating effects between the high-velocity and low-velocity heat channels, indicating that the change in phonon velocity might not be the reason behind reduction of κ.

To rule out the combined effect of phonon frequency and phonon occupation
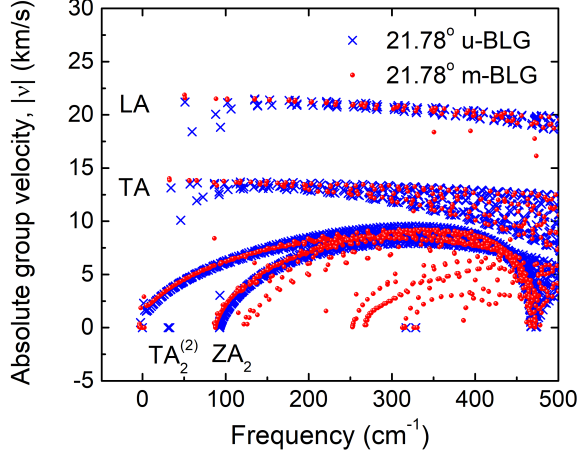
Figure 3.7: Distribution of the absolute velocity $|v|$ of the phonons in the irreducible BZ, focusing only the low-energy modes.

(Boltzmann distribution) f_λ^0, we have also calculated the heat capacity, $C_v = (\partial E/\partial T)_v$, where the harmonic phonon energy is given by, $E = \sum_\lambda \hbar\omega_\lambda[\frac{1}{2} + 1/(e^{\hbar\omega_\lambda/K_B T} - 1)]$. Since thermal conduction depends directly on the heat capacity as, $\kappa = \frac{1}{NV} \sum_\lambda C_v v_\lambda^\alpha v_\lambda^\beta \tau_\lambda$, it is imperative to see how the heat capacity behaves with misorientation. We find that the heat capacity is almost invariant to misorientation (see Fig. 3.8). Existing empirical model [123] also agrees well with DFT calculated heat capacity. Therefore, one can expect that the changes of phonon modes and phonon activation, caused by misorientation, will not affect the overall thermal conduction. Phonon-phonon scattering (τ_λ) remains to be the only factor that can explain the reduction of κ in m-BLG system. In the next section, we will explore the three-phonon scattering mechanism to understand the nature of thermal transport in m-BLG system.
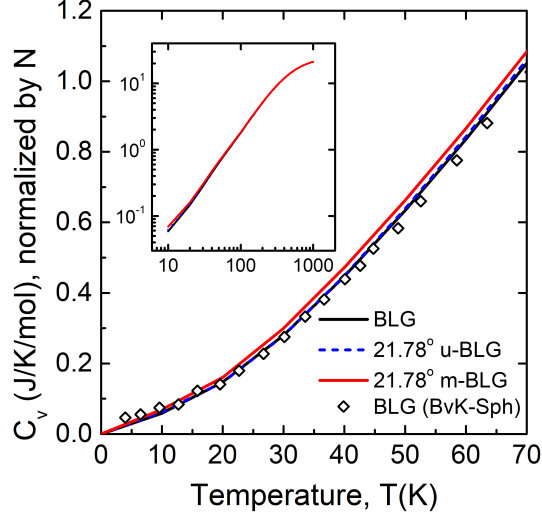
Figure 3.8: Heat capacity of AB-BLG, u-BLG and m-BLG, normalized by the number of atoms in the unit cell (N). The heat capacity remains almost same in the BLG system, irrespective of interlayer rotation. The symbols indicate the heat capacity reported by empirical model [37]. The inset shows the log-scale behavior up to T = 1000 K. Beyond T = 100 K, heat capacities of u-BLG and m-BLG do not show any difference.

3.4.4 Phonon-phonon scattering in m-BLG

The lowering of QA phonon branches and changes in low-energy optical phonon modes can introduce significant phonon scattering among the heat-carrying channels in m-BLG. To study the effect of phonon scattering on κ, it is necessary to calculate the scattering lifetime explicitly, both before and after misorientation. Figure 3.9 shows the calculated scattering lifetime for 21.78° u-BLG and 21.78° m-BLG. As evident from the scattering distribution, the m-BLG has ∼2 times lower lifetime (hence ∼2 times higher phonon scattering), when compared to u-BLG, specifically in the low-frequency range ($<$ 600 cm^{-1}). The higher scattering in acoustic and quasi-acoustic phonon branches can explain the two-times reduction of thermal conductivity seen in Fig. 3.2.

Note that, we have compared scattering lifetime between u-BLG and m-BLG cases,

both having same BZ size. Therefore, the BZ reduction and reorientation are certainly not the reasons behind such increased phonon scattering rate in m-BLG. One speculation is that the change in the phonon dispersion may introduce new phonon scattering channels and hence negatively affect the κ. Another explanation could be the increase in the phase space of existing phonon channels, allowing more scattering. With the explicit solution of phonon BTE at hand, we can evaluate and quantify these claims more effectively. For the misoriented BLG, either or both can be the underlying reason. Figure 3.9 shows that, although the extinction of flat LA_2/TA_2 modes in m-BLG increases the phonon scattering around ~ 28 cm^{-1}, the overall numbers of such channels are insignificant. On the contrary, almost all the existing acoustic phonon and ZA_2 phonon modes up to 100 cm^{-1} almost uniformly exhibit $2 \sim 2.5$ times higher scattering in m-BLG system.

The scattering mechanism that limits the heat conduction is the three-phonon normal and umklapp scattering. One of the unresolved questions for κ in m-BLG is to explain the contribution of the underlying normal and umklapp processes. To answer that, we calculate the ratio of κ of the RTA solution to κ of the iterative phonon BTE solution, $\gamma = \kappa_{\text{RTA}}/\kappa_{\text{Iterative}}$, as seen in Fig. 3.9 (b). RTA approach of solving BTE neglects the momentum-conserving N-process and underestimates κ. Hence, γ can work as an effective parameter indicating the strength of normal scattering processes compared to the umklapp scattering processes. Moreover, at low temperatures (less than Debye temperature), the resistive umklapp processes freeze out, while normal process dominates [19]. Hence, the response of γ with temperature, as shown in Fig. 3.9 (b), can shed light on the underlying nature of these processes in the presence of misorientation.
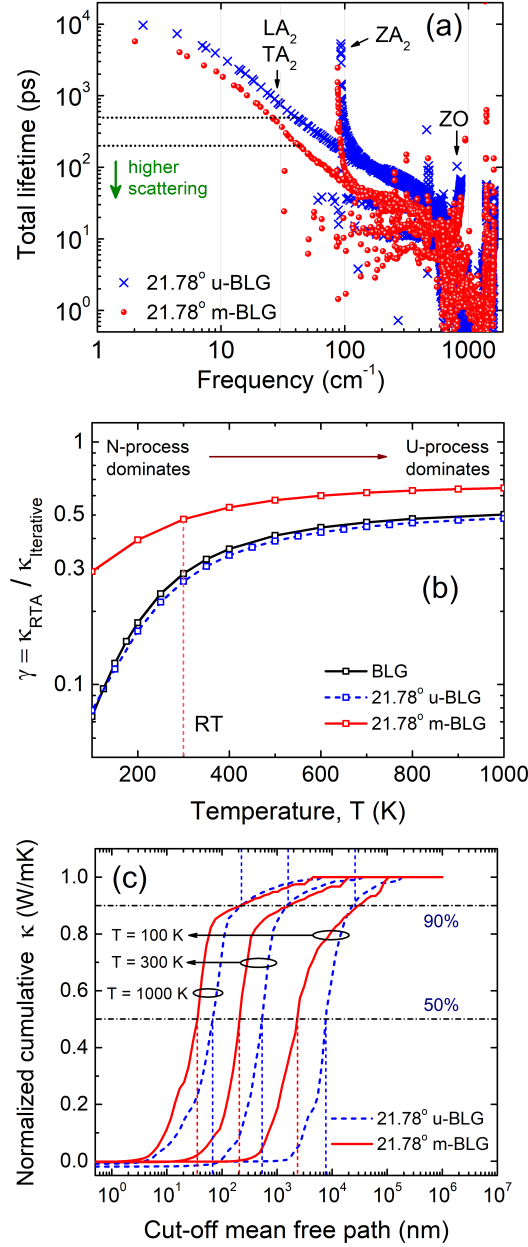
Figure 3.9: (a) Three-phonon scattering lifetime of unrotated BLG (u-BLG) and misoriented BLG (m-BLG) for $\theta = 21.78°$. (b) The ratio of thermal conductivities obtained from RTA approximation and full iterative approach, for all the u-BLG and m-BLG structures. At low temperature end, the normal (N-) process dominates, while at high temperature limit, the umklapp scattering becomes significant. (c) Cumulative thermal conductivity for $21.78°$ u-BLG and m-BLG, normalized to respective maximum values of κ, as a function of cut-off mean free path λ. The critical mean free path is a strong function of temperature.

At low temperature limit and for $21.78°$ u-BLG case, κ_{RTA} is 10 times lower than $\kappa_{\text{Iterative}}$ ($\gamma \sim 0.1$), indicating that RTA fails to account for the dominating N-process in this range. However, in case of misorientation, γ increases by almost three times, which indicates that some of the N-processes get suppressed due to twisting and hence RTA results are improved. On the other hand, at high temperature limit, umklapp scattering starts to dominate over N-process and as a result, the RTA prediction again improves. Note that, for both u-BLG and m-BLG, κ_{RTA} is still almost half of $\kappa_{\text{Iterative}}$, indicating that N-process is very much comparable to U-process. Similar dynamics between N- and U-process has been observed in penta-graphene [212] and other Carbon allotropes [218, 132]. Note that, at this high temperature range, the effect of misorientation is quite suppressed. This may be one of the reasons why the experiments shows similar thermal conductivity for u-BLG and m-BLG at the high temperature limit, as seen in Fig. 3.3.

Interestingly, between these two temperature extremes, misorientation plays a significant role. At room temperature, γ is ~ 0.25 in u-BLG, which is similar to the graphene system (~ 0.2) [16, 119]. However, in the presence of misorientation, γ increases to ~ 0.5. This signifies that although umklapp scattering is less dominant compared to N-process in u-BLG, after misorientation, umklapp scattering increases, making U-process equally dominant as N-process in m-BLG. Therefore, we conclude that the increase in umklapp scattering over the normal scattering is the reason behind the reduction of phonon lifetime in Fig. 3.9 (a), which in turns reduces the thermal conductivity in m-BLG.

The calculation of Grüneisen parameter (γ_G) also supports the conclusion. Grüneisen parameter is a measure of phonon-phonon scattering intensity and indicates the strength
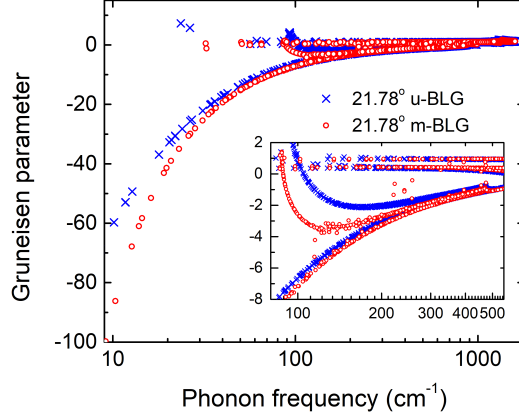
Figure 3.10: mode-decomposed Grüneisen parameter γ_G, calculated within the irreducible BZ. In presence of misorientation, the acoustic phonon modes shows larger negative γ_G, indicating high anharmonicity in m-BLG.

of anharmonicity present. As seen in Table 3.2, m-BLGs have almost two-times larger values of γ_G and hence larger anharmonic contribution to scattering. Furthermore, mode-decomposed Grüneisen parameter calculation (see Fig. 3.10) suggests that the phonon modes in the range of $0 \sim 200$ cm^{-1} mostly encounter significant anharmonicity, which is consistent with the higher scattering distribution in Fig. 3.9 (a).

Finally, we discuss the length-dependence of the thermal conductivity, with respect to the misorientation. In macroscopic samples, the heat conductivity is described by the Fourier's law, which can be translated to the microscopic thermal picture of phonon-phonon scattering, only when the experimental sample size (L) exceeds certain critical mean free length [212]. In Fig. 3.9 (c), we plot the cumulative contribution of mean free path (MFP) length to the normalized thermal conductivity, for 21.78° u-BLG and 21.78° m-BLG structure, at different temperatures. At RT and in case of u-BLG, phonon branches having MFP shorter than 550 nm contribute to 50% of κ, whereas modes with MFP exceeding

48

Table 3.2: Mode-averaged Grüneisen parameter (γ_G) and representative mean free path (λ_R) of heat carrying phonons in 21.78° u-BLG and 21.78° m-BLG, at T = 300 K.

	γ_G	λ_R (nm)
21.78° u-BLG	-1.3	513.35
21.78° m-BLG	-1.89	232.44

1.6 μm contribute only about 10%. In case of m-BLGs, only phonons with MFP less than 200 nm can contribute to 50% of κ, while longer MFP modes as 1.6 μm still contributes ~10%. This indicates that the thermal conduction in m-BLG systems is more resilient to nanostructuring than corresponding u-BLGs. If the grown BLG sample size is around 550 nm, u-BLG will show ~50% of κ (~889.3 W/m·K), whereas m-BLG will show ~84% of κ (~708.2 W/m·K), effectively masking out any effect of misorientation. Similar behavior is observed in case of other misorientation angles. Hence, the experimental sample size is an important factor when comparing with macroscopic κ, since longer MFP phonons may not be activated to carry heat due to small length scale of the samples. Given that, the acoustic phonons have larger MFP than the optical ones, it also signifies the importance of acoustic branches on determining κ. The significance of acoustic and quasi-acoustic modes is also apparent from the mode-accumulated κ calculation, where the phonon modes up to 600 cm^{-1} carries almost 90% of total κ at RT (see Fig. 3.11).

To obtain a representative mean free path (λ_R) of heat carrying phonons, the cumulative kappa with respect to maximum MFP allowed (λ_{max}) can be fitted to a single parametric function, [126]

$$\kappa\left(\lambda < \lambda_{max}\right) = \frac{\kappa_0}{1 + \lambda_R/\lambda_{max}}, \tag{3.3}$$
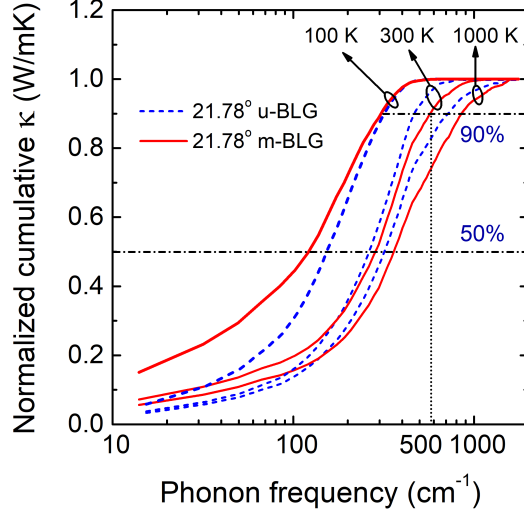
Figure 3.11: Cumulative thermal conductivity κ as a function of phonon frequency, when normalized to respective maximum. 90% of the thermal conduction is contributed by the phonon modes up to $\sim$600 cm^{-1}.

where, κ_0 is the maximum thermal conductivity. As tabulated in Table II, MFP λ_R for 21.78° is very close to the AB-BLG value (499.51 nm). It is clear that the representative MFP λ_R gets reduced by almost half in m-BLGs.

Changing temperature broadens the mean free path range from 5 nm to 100 μm. As evident from Fig. 3.9 (c), the effect of misorientation on length scale is less pronounced at high temperature, but amplified at low temperature. With twisting, the representing MFP at 1000 K for 21.78° structure reduces from 64.14 nm to 34.39 nm, whereas MFP at 100 K goes down from 8.32 μm to 2.78 μm with misorientation. The length scale of the samples used for κ measurement [123] can also be one of the reasons why the experimental κ for twisted BLG is in the same order as the untwisted one. A large size of the sample (50 $\sim$ 100 μm) will ensure that the heat transport by phonons are in diffusive range and hence eliminate the unwanted effect of reduced MFP length [212].

3.5   Conclusion

We have calculated the phonon dispersion and thermal conductivity of twisted bilayer graphene, for commensurate rotational angles of 21.78°. Instead of relying on the parametric approximation of interatomic force constant, we calculate the second-order harmonic and third-order anharmonic force constant using ab initio density functional theory, and use them to self-consistently solve the linearized phonon Boltzmann transport equation, within three-phonon scattering framework. We find that misorientation reduces the intrinsic thermal conductivity of m-BLG to almost half when compared to that of AB-BLG. By calculating the phonon dispersion, group velocity, density of states and heat capacity, we conclude that the modification in phonon frequency, velocity distribution and phonon occupation has insignificant effect on thermal conduction. On the other hand, explicit calculation of phonon-phonon scattering reveals that, the reduction in three-phonon scattering lifetime is the reason behind the reduced thermal conductivity in misoriented bilayer graphene system. We also identify that, in misoriented bilayer graphene, umklapp scattering becomes more dominant compared to the normal process, due to the increased anhamonicity introduced by the moiré patterns in such twisted system.

Chapter 4

Ab initio thermal conductivity of quasi-1D materials: TaSe$_3$ and NbS$_3$

4.1 Introduction

Low dimensional materials, specifically the graphene and 2D transition metal dichalcogenides (TMDs), have emerged as promising candidates for better electronic, opto-electronic and thermoelectric devices, due to their diverse electron and phonon functionalities inherent in the atomically-thin dimensions [214, 26, 36, 228, 57, 18, 152]. Going beyond two-dimensions, transition metal trichalcogenide (TMTs) present themselves as even more attractive choice in this direction. TMTs have lower in-plane structural symmetry, which can give rise to pseudo one-dimensional behavior [89], exhibiting some attractive capabili-

ties, e.g. superconductivity [192, 79, 229], CDW formation [180, 253], and high breakdown current [135]. Besides, due to the possibility of reduced backscattering from hot electron [23, 3], the anisotropy inherent in TMTs can provide additional benefit for next generation electronics, contacts, polarizers and photo-detectors [243, 235].

The lattice structure of TMTs consists of a metal (M) atom, contained at the center of the trigonal prism made by chalcogen (X) atoms. Such MX_3 prisms create long infinite chains arranged side-by-side, which effectively makes it a two-dimensional layer of one-dimensional chains [52], giving them the apt name of quasi-1D materials. Although the metal-metal distance along the chain is comparable to the inter-metallic distance in pure metal, the interchain distance is comparatively larger, giving rise to directional anisotropy in electrical and optical properties [184, 95, 41, 88, 172, 40, 110]. Electronic properties of some quasi-1D materials, specifically the resistivity, superconductivity, photo-electron spectroscopy, CDW transition, and band properties have been studied for quite a time [52, 89]. However, the accurate phonon properties of quasi-1D materials have remained little explored [221]. Moreover, to date, there is a lack of investigations of thermal conduction in TMT materials, both from experiment and theoretical perspective.

Another motivation to explore the low-dimensional materials is due to their potential of exhibiting higher thermoelectric efficiency, $i.e.$ higher figure of merit, $ZT = S^2 \sigma T / (\kappa_e + \kappa)$. Here, S is the Seebeck coefficient, σ is the electrical conductivity. κ_e and κ are the electrical and lattice contribution to the thermal conductivity. The electrical part of thermal conductivity can be calculated from the Wiedemann-Franz law, $\kappa_e = L\sigma T$, where L is the Lorentz number. However, to evaluate ZT, accurate phonon-limited intrinsic ther-

mal conductivity κ is necessary. As theoretically suggested [49], low-dimensional systems could have dramatically larger ZT values than the corresponding bulk materials because of decreased thermal conductivity caused by phonon boundary scattering and improved power factors on account of quantum confinement. Hence, understanding the phonon scattering mechanism in quasi-1D materials is not only interesting from the fundamental physics point of view, but also interesting from the engineering perspective of designing thermoelectric devices. To be a good thermoelectric system, the material has to be a bad conductor for phonon but a good conductor for electron. Quasi-1D metals like $TaSe_3$ seems to be a promising candidate that meets this contradictory criteria. To evaluate the thermal performance of $TaSe_3$, we calculate the phonon properties and phonon-limited heat conductivity in this materials. Along with that, we also explore the thermal conduction of another member of quasi-1D material family, semiconducting NbS_3, to present a comparative analysis of phonon transport behavior in such low electron-conducting system. Their comparative analysis will allow us to understand the nature of thermal transport in both electron-rich and electron-deficient quasi-1D materials.

Note that, many quasi-1D materials show charge density wave (CDW) transition. However, both $TaSe_3$ and NbS_3, although expected to show CDW, do not exhibit any CDW transition [62, 199, 53]. This makes them good example for studying thermal properties, since the conduction behavior will not get affected by any unexpected CDW instability. In this paper, we will use ab initio density function theory and phonon Boltzmann transport equation, to explore the lattice thermal conductivity of $TaSe_3$ and NbS_3, and study the nature of phonon interaction in these two representative quasi-1D materials.
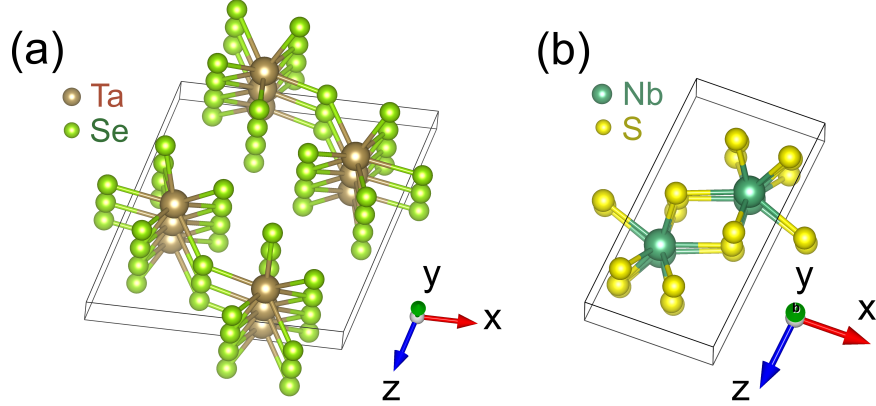
Figure 4.1: Crystal structure of (a) TaSe$_3$ and (b) NbS$_3$. The wires grow along the **b** direction.

TaSe$_3$ has monoclinic crystal structure with space group P2$_1$/m, having [11] $a = 10.411$ Å, $b = 3.494$ Å, $c = 9.836$ Å, and $\beta = 106.36°$. The atomic configuration is shown in Fig. 4.1 (a). The nanowires are grown along the y direction, whereas along the slanted z-direction, they are inter-connected by the van der waals force. Although similar prismatic structure NbSe$_3$ shows CDW phase, no CDW phase is observed in TaSe$_3$, because of comparatively much stronger dispersion along x-z plane [24]. However, superconductivity has been observed in this material below $T_c = 2.1$ K [192, 79, 229, 158, 157], with a negative pressure coefficient of T_c [232]. The electrical resistivity of TaSe$_3$ at room temperature is reported to be ~6 × 10^{-6} Ω·m [79] and it remains metallic up to the helium temperature [192, 79]. A T^2-dependence of resistivity has been observed, which has been attributed to arise from the dominant electron-electron umklapp scattering (U) process [79]. A high-pressure phase of TaSe$_3$ has also been reported, although electronic properties remain same as the conventional TaSe$_3$ phase [106].

On the other hand, NbS$_3$ is a semiconductor, having a triclinic structure of P$\bar{1}$

symmetry [96, 188, 147]. Although several other phases of NbS_3 have been reported, NbS_3 phase-I is the most well documented phase (we will denote it as NbS_3 for simplicity). NbS_3 remains semiconducting over a wide range of temperature from 4.2 K to 650 K [53]. Figure 4.1 (b) shows the atomic configuration of this phase. Weak van der Waals interactions exist between the S atoms between the neighboring chains. The Nb atoms are displaced by 0.16 Å from the mirror plane, causing a linear peierls distortion [188]. Nb-Nb pairing through $d^1 - d^1$ bond is the reason for NbS_3 being a semiconductor [120], which is also supported by the density of states calculation [25] and X-ray photoelectron spectroscopic (XPS) [53].

4.2 Methodology

We perform the structural optimization of $TaSe_3$ and NbS_3, within the framework of density function theory using projector-augmented-wave (PAW) pseudopotentials [14] and Perdew-Burke-Ernzerhof (PBE) exchange correlation functionals [175], as implemented in VASP [115, 114]. The van der Waals interactions are included by semi-empirical correction of Grimme-D2 [77]. For structural relaxation of $TaSe_3$ (NbS_3), a converged k-point grid of $9\times9\times3$ ($8\times8\times4$), respectively. All structures are relaxed until the forces on the atom is less than 10^{-5} eV/Å and the energy convergence reaches 10^{-8} eV. The relaxed lattice constants of $TaSe_3$ and NbS_3 are within 1% of the experimentally reported values.

To obtain the phonon frequency dispersion and other thermodynamics properties, the second-order (harmonic) interatomic force constants (IFCs) is required. The second-order IFCs are calculated within supercell approach using the Phonopy package [206]. For the phonon dispersion of $TaSe_3$ (NbS_3), a supercell size of $2\times2\times2$ ($2\times2\times2$), has been used,

with a K-point grid of 2×6×2 (9×9×3), respectively.

The thermal conductivity along certain direction α, can be calculated using the Boltzmann phonon transport equation, within the three-phonon scattering framework [129]

$$\kappa_{\alpha\beta} = \frac{1}{K_B T^2 N V} \sum_\lambda f_\lambda^0 (f_\lambda^0 + 1)(\hbar \omega_\lambda)^2 v_\lambda^\alpha v_\lambda^\beta \tau_\lambda. \tag{4.1}$$

Here, ω_λ is the phonon energy of each phonon mode λ, f_λ^0 is the equilibrium Boltzmann distribution of that mode, v_λ is the group velocity, ∇T the temperature gradient along the direction β and τ_λ is the phonon-phonon scattering lifetime. λ represents both phonon branch index p and wave vector $\mathbf{q}$. V is the volume and N is the number of uniformly doped $\mathbf{q}$ points in the irreducible Brillouin zone. The scattering lifetime τ_λ in Eq. (4.1) is given by [148], $\tau_\lambda = \tau_\lambda^0(v_\lambda^\beta + \Delta_\lambda)$, where, τ_λ is the lifetime obtained under relaxation time approximation (RTA), and Δ_λ is a correction to RTA, providing an iterative solution to BTE.

To calculate the three-phonon scattering matrix and subsequently the thermal conductivity, we have calculated the third-order (anharmonic) IFCs for $TaSe_3$ and NbS_3. A 2×2×1 supercell have been used to calculate the anharmonic IFCs, which generates 3472 and 1344 configurations for $TaSe_3$ and NbS_3, respectively. Both relaxation time approximation (RTA) and full iterative approach, are used to solve the phonon BTE, as implemented in the ShengBTE package [126, 130]. The convergence of κ for a certain Nq×Nq×Nq integration grid is tested with a precision of 10^{-5} difference between the iterative steps. The atomic interaction up to 5th-nearest neighbor is considered. Moreover, the convergence with respect to different Nq×Nq×Nq mesh-grid is also checked (see Fig. 4.2). We use converged Nq-grid of 14×14×6 for both $TaSe_3$ and NbS_3. The effect of born effective charge is included in the
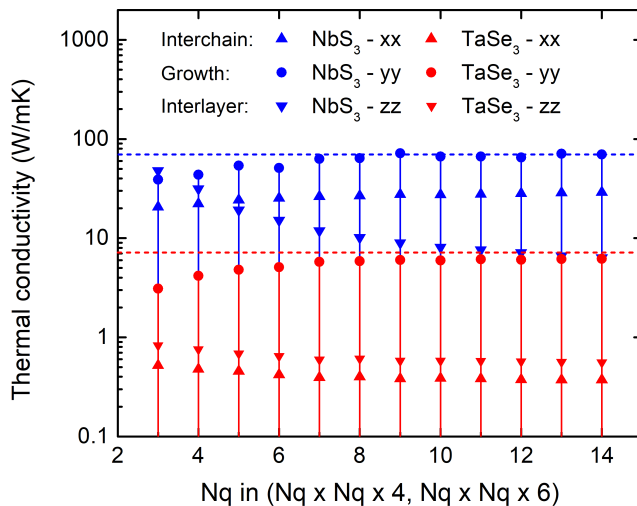
Figure 4.2: Convergence of κ with respect to Nq×Nq×4 (Nq×Nq×6) for NbS$_3$ (TaSe$_3$).

phonon calculation, although the non-analytical corrections to the phonons are found to be negligible in both cases.

4.3   Results and discussions

4.3.1   Phonon dispersion

We show the phonon dispersion of TaSe$_3$ in Fig. 4.3 (a). The color scheme indicates the absolute group velocity at each phonon **q**-vector and phonon branch. The large number of atoms in the unit cell creates complex Raman spectra with closely spaced lines. The vibrational modes in TaSe$_3$ in given by [221],

$$\Gamma_{\text{TaSe}_3} = 8A_u + 8B_g + 16B_u + 16A_g. \tag{4.2}$$

The A_g modes have vibrations limited to the x-z plane, whereas the B_g modes are polarized

along y axis. The experimental peaks, as indicated by the symbols in Fig. 4.3 (a), match well

with the DFT calculated phonon dispersion. From the mode eigenvalues, we can identify the

shearing vibration of the chains (B_g) at 74.68 cm^{-1}, where each adjacent chains slides out-

of-phase with respect to one another. The calculated frequency is also close to the shearing

frequency in ZrSe$_3$ (77 cm^{-1}) [221]. Besides, we can identify the rotation/liberation mode

at 51.74 cm^{-1} and 70.18 cm^{-1}, which is close to the observed Raman peak for this mode (52

cm^{-1} and 60 cm^{-1}). The DFT predicted peaks are more consistent with experiment, when

compared to prior bond-theory model [221]. The highest frequency (268.5~269.4 cm^{-1})

modes arise from the Se-Se motion from the two out of four MX$_3$ units, specifically from

the ones with shortest Se-Se bonds.
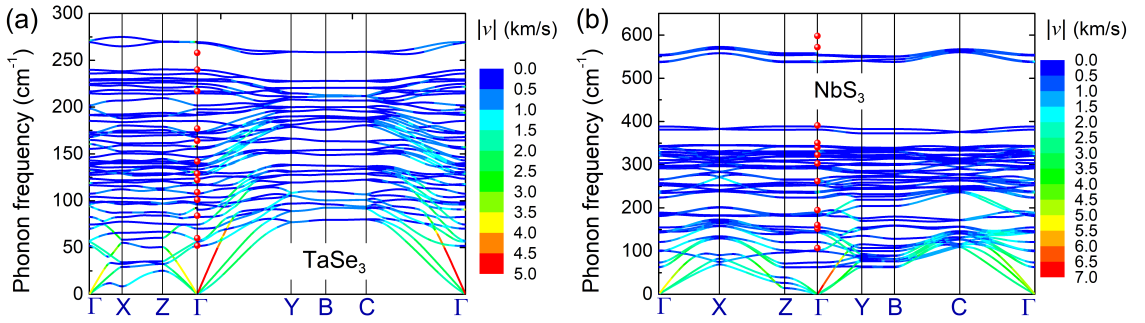
Figure 4.3: Phonon dispersion of (a) bulk TaSe$_3$, (b) bulk NbS$_3$. The color indicates the absolute group velocity at each **q** and phonon modes. The symbols indicate the experimental Raman peaks at 300 K, for TaSe$_3$ [221] and NbS$_3$ [201].

We have also calculated the phonon dispersion of NbS$_3$, as shown in Fig. 4.3 (b).

NbS$_3$ belongs to the $P1$ (C$_i^1$) space group, also having 48 normal modes [251],

$$\Gamma = 24A_g + 24A_u. \tag{4.3}$$

Only 24 even-parity modes show Raman activity, whereas 21 odd-parity modes are infrared active. The symbols in Fig. 4.3 (b) indicate the prior Raman data from the literature [251, 201]. Unlike other chalcogenides, NbS$_3$ phonon modes cannot be classified by the vibration along the chain and perpendicular to chain directions, due to the symmetry breaking of the screw axis [251]. The high frequency bands beyond 500 cm^{-1} is characterized by the stretching motion of (S$_2$)$^{2-}$ pairs inside the prismatic chains. The top two modes of NbS$_3$-I (554.27 cm^{-1} and 552.69 cm^{-1}), the (S$_2$)$^{2-}$ bonds of top and bottom chains vibrate in phase. On the other hand, for the next two phonon branches (537.36 cm^{-1} and 538.29 cm^{-1}), the top (S$_2$)$^{2-}$ bond stretches, while the bottom one shrinks. The high frequency of these modes are an indirect indicator that the (S$_2$)$^{2-}$ bonding in NbS$_3$ is stronger than other transition metal trichalcogenides like ZrSe$_3$, HfS$_3$ [201].

It is evident from the color-coded normalized velocity plot in Fig. 4.3, the acoustic phonon and low-energy phonon branches are the significant phonon modes to thermal conduction, due to their higher velocity. Moreover, the directional dependence of the phonon velocity seen in Fig. 4.3 is a clear indicator of the anisotropy inherent in these quasi-1D materials. In TaSe$_3$, the maximum velocity along growth direction (Γ-Y) is ∼5 km/s, whereas the inter-chain and vdW direction, it is around 4 km/s. On the other hand, in case of NbS$_3$, the maximum velocities (LA mode) along growth, inter-chain and vdW direction are ∼7 km/s, ∼5 km/s and ∼3 km/s, respectively. It seems NbS$_3$ shows higher anisotropic behavior, compared to TaSe$_3$, although we cannot be certain without explicit calculation of

κ, since thermal conductivity is not merely a function of velocity. Comparing between the materials themselves, we can see NbS_3 velocities are 40% higher along the growth direction than that of $TaSe_3$, indicating that NbS_3 possibly would be a better phonon conductor than $TaSe_3$.

Another feature of the phonon dispersion of these quasi-1D materials are the presence of several flat bands, as we have discussed earlier. From the velocity point of view, these flat optical modes cannot contribute much to the thermal conduction. However, they can introduce additional physics in heat transport by allowing significant phonon-phonon scattering. The flat bands can work as phonon scattering centers and hence reduce the mobility of heat-carrying phonons. To find out the final thermal conductivity, by simultaneously considering the competing effects of velocity and scattering, we will use the ab initio DFT calculation coupled with phonon BTE equation in the next section.

4.3.2   Thermal conductivity

In Fig. 4.4, we calculate the thermal conductivity for $TaSe_3$ and NbS_3, by solving the BTE using full iterative approach. We find that, the thermal conductivity of $TaSe_3$ along the growth direction is low (6.33 W/m·K at 300 K), but similar to other metallic TMD materials [46]. Along the interchain and interlayer direction, κ is almost same (0.37 and 0.57 W/m·K, respectively). The reason for such similar κ in those directions is the byproduct of the way the lattice vectors are defined in $TaSe_3$ unit cell. Unlike NbS_3, $TaSe_3$ has a corrugated atomic surface. As seen in Fig. 4.1 (a), x direction is not true inter-chain direction, rather it also contains a vdW gap due to its slanted nature. Similarly, z is not purely perpendicular to the true interchain direction. Due to the vdW gap present in both
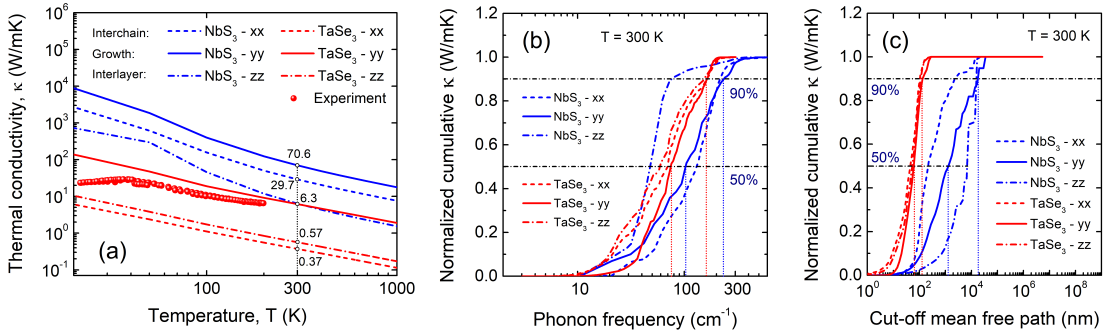
Figure 4.4: (a) Lattice thermal conductivity of bulk TaSe$_3$ and NbS$_3$. (b) The normalized κ as a cumulative function of phonon frequency, (c) The normalized κ as a cumulative function of mean free path.

case, we see a reduced but similar κ in both orientations. However, this does not limit us in estimating a relative strength of anisotropy between growth direction and in-plane direction. The anisotropy ratio of the κ along the chain to the κ along the vdW gap is at least one-order higher (17 ∼ 18) in TaSe$_3$.

On the other hand, calculated κ in semiconducting NbS$_3$ is already one-order higher (67 W/m·K at 300 K) along the growth direction, when compared to TaSe$_3$ case. Along the interchain and interlayer direction, κ is 29.7 W/m·K and 6.3 W/m·K, exhibiting an anisotropy factor of 2.25 and 10.63, respectively. Note that, anisotropy along the vdW direction is one-order lower, similar to TaSe$_3$ case. However, from the higher anisotropy strength along the vdW direction, we can say TaSe$_3$ is more two-dimensional in nature than NbS$_3$.

The experimental reports of thermal conductivity of quasi-1D materials are very rare, due to the difficulty in measuring the thermal conduction in such ribbon-like geometries [240]. To our knowledge, only one study of thermal conductivity measurement of TaSe$_3$ has

Table 4.1: Representative mean free path (λ_R) of heat carrying phonons in TaSe$_3$ and NbS$_3$, at T = 300 K.

	λ_R (nm)		
	inter-chain	growth	inter-layer
TaSe$_3$	7.34	10.58	8.5
NbS$_3$	53.41	242.33	937.03

been reported using parallel thermal conductance (PTC) technique [239]. As shown in Fig. 4.4 (a), we have compared the measured κ with the calculated values. There is almost one-order difference between the theory and experiment at low-temperature end. The mismatch becomes smaller around T = 200 K (experiment: 6.62 W/m·K, theory: 9.11 W/m·K), when the phonon-phonon scattering mechanism starts to dominate at high temperature range. From the experimental side, the accuracy of PTC technique to handle chain-structures like TaSe$_3$ is still under question [240]. From the modeling side, the experimental samples may contain impurities and phonon boundaries, which are not included in the simulation. The impurity scattering and boundary scattering will certainly reduce the thermal conductivity in TaSe$_3$. In case of NbS$_3$, no thermal measurement of κ is available to date, to compare with the DFT calculation.

To understand which phonon modes contribute most to the thermal conductivity, we look in to the normalized κ as a cumulative function of phonon frequency in Fig. 4.4 (b). In case of TaSe$_3$, 50% of κ along the chain is contributed by the modes below 80 cm^{-1}, whereas the phonons up to 160 cm^{-1} carry 90% of the heat. On the other hand, in NbS$_3$, phonons up to 100 cm^{-1} carry 50% of heat along the chain, while the modes up to 230 cm^{-1} are responsible for 90% of conduction. For both cases, the optical phonons beyond
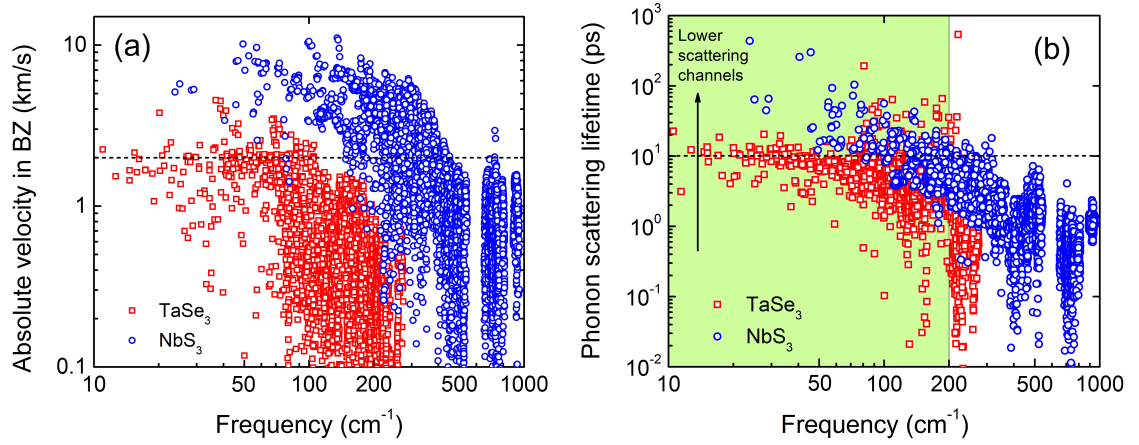
Figure 4.5: (a) Absolute velocity of phonon modes $\mathbf{q}$ in the irreducible BZ of TaSe$_3$ and NbS$_3$. (b) Scattering lifetime for phonon-phonon scattering process in TaSe$_3$ and NbS$_3$.

roughly 200 cm^{-1} has limited contribution to thermal conductivity.

Another important direction for modulating the thermal performance of quasi-1D materials is to know how the conductivity will get affected when the chains are scaled down in certain direction. To explore the effect of nanostructuring, we calculate the normalized κ at RT as a cumulative function of cut-off mean free path, as shown in 4.4 (c). The mean free path of phonons responsible for carrying 90% of heat is around 100 nm in TaSe$_3$, while the corresponding mean free path in NbS$_3$ is $\sim$2 μm, two-order longer. Typically the acoustic phonons carry the longer phonon MFP. Moreover, the range of the spectrum of phonon mean free path is much broader in NbS$_3$ than TaSe$_3$. In TaSe$_3$, phonon MFP between 10 $\sim$ 100 nm is mostly responsible for determining κ, while in NbS$_3$, wide range of phonons having MFP between 100 nm to 10 μm can effectively contribute towards thermal conduction.

To obtain a representative mean free path (λ_{R}) of heat-carrying phonons in these

64

quasi-1D materials, the cumulative κ with respect to maximum MFP (λ_{max}) in Fig. 4.4 (c), is fitted to a single parametric function, [126]

$$\kappa\left(\lambda < \lambda_{\mathrm{max}}\right) = \frac{\kappa_0}{1 + \lambda_{\mathrm{R}}/\lambda_{\mathrm{max}}}, \tag{4.4}$$

where, κ_0 is the maximum thermal conductivity. As tabulated in Table 4.1, MFP λ_{R} along the growth direction is one-order larger in NbS$_3$, whereas along the inter-layer direction, it is two-order higher.

To explain why there is a significant difference between the conduction in TaSe$_3$ and NbS$_3$, we look in to the phonon velocity as well as phonon scattering of the thermal modes, in both materials. Figure 4.5 (a) shows the absolute velocity distribution of the heat-carrying phonons, for each phonon modes $\mathbf{q}$ inside the irreducible Brillouin zone (BZ). From the distribution, it is clear that most of the phonon channels in TaSe$_3$ have five to ten times lower velocity than that of NbS$_3$. Between $20 \sim 80$ cm^{-1}, some of the phonon modes of TaSe$_3$ have slightly higher velocity, but still lower than NbS$_3$. However, to explore how these high-velocity modes will get compensated by unwanted phonon scattering, we also look in to the scattering rate of these channels. As seen in Fig. 4.5 (b), the scattering lifetime in TaSe$_3$ are distributed around $10 \sim 20$ ps in the low-energy range ($20 \sim 80$ cm^{-1}). Beyond 100 cm^{-1}, the lifetime improves in TaSe$_3$ (scattering reduces) by almost $5 \sim 10$ times, but unfortunately the velocity of these modes starts to become low at that point. It is clear that the higher-velocity phonons undergoes higher scattering in TaSe$_3$, resulting in poor thermal conduction. On the contrary, in NbS$_3$, the low-energy modes up to 100 cm^{-1} exhibit higher velocity as well as lower phonon scattering. Beyond 100 cm^{-1}, the scattering rate becomes similar to TaSe$_3$ case, but the velocity still remains one-order higher. Hence,

both higher velocity and larger lifetime in NbS$_3$ are the reason behind the one-order higher κ observed in Fig. 4.4 (a).

We also discuss the normal and umklapp three-phonon scattering mechanism in TaSe$_3$ and NbS$_3$, to get an insight on the competition between these two phonon scattering processes in quasi-1D materials. Figure 4.6 shows the κ ratio of the RTA solution and iterative solution of phonon BTE, as $\gamma = \kappa_{\mathrm{RTA}}/\kappa_{\mathrm{Iterative}}$. RTA approach of solving BTE neglects the momentum-conserving N-process and underestimates κ. Hence, γ is an effective parameter that can indicate the strength of normal scattering processes compared to the umklapp scattering processes. As we see in Fig. 4.6, the RTA calculation in NbS$_3$ matches well with the iterative solution ($\gamma \sim 1$), indicating that normal process is insignificant in NbS$_3$; rather, even at low temperature limit, the umklapp process is the dominating scattering mechanism in this quasi-1D materials. This is in stark contrast with the phonon scattering process in two-dimensional materials like graphene, where both umklapp and normal process contribute almost equally to conduction ($\gamma \sim 0.3$). Similarly, in TaSe$_3$, value of γ along the growth direction is almost 0.7, even at temperature as low as 100 K. This indicates that although normal process plays a role in thermal conduction, umklapp process still remains to be a dominant scattering mechanism in metallic TaSe$_3$. In general, the umklapp scattering mechanism seems to be the ultimate determining factor for phonon-limited κ in quasi-1D materials.
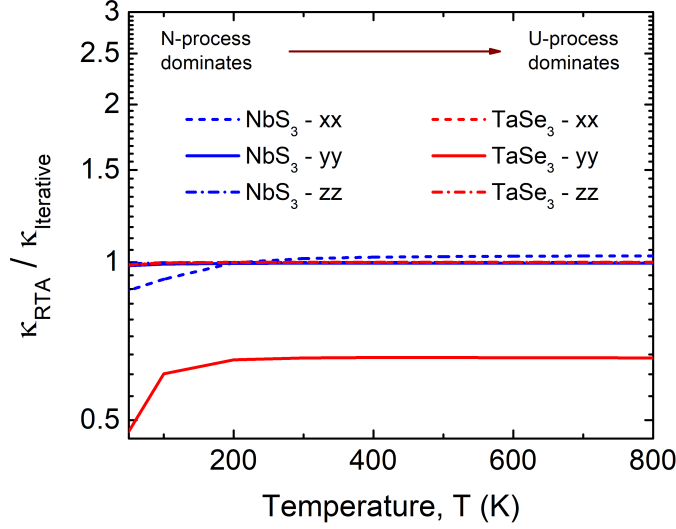
Figure 4.6: Ratio of κ of RTA solution by iterative solution.

4.4 Conclusion

We have calculated the phonon dispersion and lattice thermal conductivity of TaSe$_3$ and NbS$_3$, using density functional theory and phonon BTE. The phonon dispersion of both quasi-1D materials exhibit several flat bands, while the low-energy modes contribute most due to their higher velocity. A comparison of experimental Raman peaks with the phonon dispersion show good match with the theory. The thermal conductivity of bulk TaSe$_3$ system is found to be one-order lower than that of bulk NbS$_3$. Both systems show one-order higher anisotropy along the chain growth direction, compared to the van der Waals direction. TaSe$_3$ shows lower phonon velocity and higher scattering rate at the low-energy limit, while NbS$_3$ exhibit opposite behavior. The maximum limit of mean free path of phonons responsible for heat conduction is found to be one-order higher along the growth

direction in NbS$_3$. Finally, we find that umklapp scattering is the dominant phonon-phonon

scattering mechanism in these quasi-1D material system.

Chapter 5

Electronic and vibrational properties of different polymorphs of quasi-one dimensional transition metal trichalcogenides NbS$_3$

5.1 Introduction

Layered materials have attracted much attention since the seminal discovery of graphene in 2004 [166]. Although high mobility of graphene makes it a promising channel material for future electronics, the absence of band gap severely limits its application for field effect devices [69, 161, 68]. As a solution to graphene's limitations, the transition metal dichalcogenides (MX$_2$), another class of layered materials, have been widely explored for

potential electronic, optical and spintronic applications [214, 26, 36, 228, 57, 18, 152]. In the ongoing effort for finding efficient layered materials, transition metal trichalcogenides (MX_3) have emerged as superior alternatives, due to their quasi-one-dimensional structures and highly anisotropic behavior [97, 85, 254]. Trichalcogenides are known since the 70's for their characteristic low-dimensional properties, *e.g.* intercalation [231, 225], CDW fluctuations, non-linear effects [73] and superconductivity [91]. Moreover, due to their chain-like growth formation, a single exfoliated chain of MX_3 can work as an ideal channel material [56], which can facilitate the current technological push towards miniaturization of nanoscale field effect transistor (FET) [4, 134]. The high current-carrying capacity and high break-down voltage of these chains have already been demonstrated for certain members of this family [135]. Along with mechanical exfoliation, the electronic properties can also be engineered by nanostructuring [95, 89]. Recently, several new phases of the quasi-1D trichalcogenide NbS_3 have been reported [15]. However, the basic electronic and vibrational properties of NbS_3, as well as their scaling effect, still remain poorly understood [15].

NbS_3 is a layered transition metal trichalcogenide with chain-like formation, which allows mechanical cleavage and is a potential material for hosting charge density waves (CDW) [180]. Niobium-Sulfur system has been studied since the 70's for its rich chemistry, stoichiometry, and numerous phases [96], *e.g.* NbS_3, 2s-NbS_2, 3s-NbS_2, 2s-$Nb_{1+x}S_2$, 3s-$Nb_{1+x}S_2$, Nb_3S_4, $Nb_{1-x}S$, $Nb_{21}S_8$, as well as ring-like structures *e.g.* NbS_3 Möbius strip [54]. Similar to other trichalcogenides, NbS_3 is a fibrous crystal, characterized by linear chain of metal atoms (Nb) along the fiber axes, surrounded by bicapped trigonal prismatic coordination of chalcogens (S). The stronger Nb-Nb bond along the chain or column di-

rection results in a highly anisotropic one-dimensional behavior in NbS_3 [17]. The chains themselves are interconnected together as a bundle by Nb-S inter-chain bonds. Each of these chain bundles are separated from each other by weak van der Waals force.

Historically, NbX_3 has been used as high energy density cathode material for rechargeable battery cells due to its intercalation reaction properties [219, 231, 104, 185, 236, 191] and as an efficient catalyst [42] that can cleave C-N and C-C bonds. In recent times, NbS_3 has attracted renewed attention with the discovery of two new phases [15]. To date, six different phases of NbS_3 has been confirmed: NbS_3-I, NbS_3-II, NbS_3-III, NbS_3-HP, NbS_3-IV and NbS_3-V. However, the correlation between the atomic structure of different phases and the corresponding electronic properties have not been well established.

The electronic properties of 1D materials are very different from 3D materials. The 3D metals can be described by Fermi-liquid theory, whereas the 1D metals are well described by Luttinger liquid theory, given that the Fermi liquid picture in purely 1D system becomes inadequate due to interlayer correlations [47]. Electrically, MX_3 materials can be a 1D insulator or a 1D conductors, or both [73]. NbS_3, due to its rich chemistry, exhibits several metallic and semiconducting phases. There are subtle differences between the Nb-Nb and S-S bond length of different phases, giving rise to various physical properties. The size of the unit cell depends on the number of prismatic MX_6 columns and their stacking arrangement, which typically ranges from just two columns (as in $ZrSe_3$) to 24 columns (as in orthorhombic TaS_3) [180].

Structurally, NbS_3 exhibits four different types of chain configurations. In one chain configuration, only one type of S-S bond exists, *e.g.* as in $ZrSe_3$; NbS_3-V belongs

to this category. NbS$_3$-I also belongs to this category, but shows a $2b$ superstructure [73]; NbS$_3$-IV, being a superstructure of phase-I itself, also belong to this category. On the other hand, NbS$_3$-HP belongs to another type of chain configuration which contains three different prismatic chains in the unit cell, having three different S-S bond length [73]. Finally, NbS$_3$-II has four different types of chains [250], out of total eight chains in the unit cell. Presence of different numbers and different types of prismatic chains is one of the reasons for observing such phase variation in NbS$_3$. The S-S bond-length is an important factor in determining the electron density available to Nb chains [73]. The chains with longer S-S bond indicate electron transfer from Nb atom to S atom, indicating possible insulating behavior in those chains. On the other hand, chains with shorter S-S bond are more prone to exhibiting metallic behavior and CDW properties.

The transport properties of the quasi-1D material also varies widely depending on the number of the prismatic chain in the unit cell. On top of that, small differences in the arrangement and stacking between the chains can lead to significantly distinct properties [25]. Hence, it is interesting to know how does the electronic properties evolve from one phase to the next. Moreover, the dynamical stability and phonon studies for most of the NbS$_3$ phases are still absent in literature.

NbS$_3$-I is the most well known phase of NbS$_3$, having a triclinic structure of P$\bar{1}$ symmetry [96, 188]. At room temperature, NbS$_3$ is described as a Peierls semiconductor [147]. Figure 5.1 (a) shows the atomic configuration of this phase, whereas the lattice parameters are listed in Table 5.1. Due to the metal-metal bond along the chain, the Nb atoms are displaced by 0.16 Å from the mirror plane, causing a linear peierls distortion,
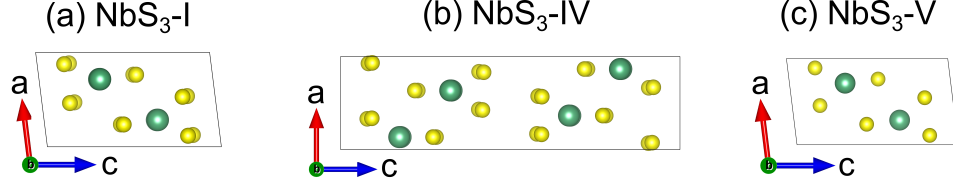
Figure 5.1: Atomic configurations (top view) of different phases of NbS$_3$: (a) phase-I, (b) phase-IV, (c) phase-V. The structural element common to all phases is the prismatic columns of NbS$_6$ trigonal prisms, where these columns or chains grow out of the page of the paper (**b** direction). The number and stacking of trigonal MX$_6$ blocks vary from phase to phase.

which in turns reduces the symmetry from monoclinic to triclinic [188]. This commensurate CDW distortion reduces the space group from P2$_1/m$ to P$\bar{1}$ [180]. Nb-Nb pairing through $d^1 - d^1$ bond is the reason for NbS$_3$-I being a semiconductor [120], as corroborated by calculated density of states [25] and X-ray photoelectron spectroscopic (XPS) [53].

NbS$_3$-I remains semiconducting over a wide range of temperature from 4.2 K to 650 K [53]. Although alternating Nb-Nb bond implies possible CDW formation, no CDW-normal transition has been observed in temperature-dependent conductance measurement [53]. Weak van der Waals interactions exist between the chalcogen (X) atoms of neighboring chains. Within the chain, one of the X-X bond in the MX$_6$ triangular prism is quite short (2.05 Å) [73], indicating the formation of disulfide anion [X–X]$^{2-}$, which makes the formal charges on the atoms are M^{4+}(X$_2$)$^{2-}$X^{2-}. This is consistent with the non-metallic behavior of NbS$_3$-I phase [73]. However, under pressure, an insulator to metal transition has been reported [47].

NbS$_3$-II is a incommensurately modulated superstructure of phase-I, where the periodicity is suggested to be 3**b** along the chain direction [39, 241]. Electron diffraction study also suggests that NbS$_3$-II is a monoclinic phase with trimerization [254], having same

P2$_1$/m symmetry [180]. Nb-Nb pairing along the **b** direction is absent in this phase [216]. The structure has not been fully determined yet, but possible atomic configuration has been proposed. The proposed unit cell [180, 216] of NbS$_3$-II contains 8 trigonal prisms, of which two are equilateral and six are isosceles. Very recently, a basic and a CDW modulated structure of NbS$_3$-II have been reported [250].

Although the overall behavior remains semiconducting, the resistivity of phase-II is three-order of magnitude lower (8×10^2 ω cm) than that of phase-I ($\sim 80 \times 10^2$ ω cm). Unlike phase-I, temperature-dependent resistivity study shows three Peierls transitions, one at 150 K [252], one around 340–355 K [216], and one at high-temperature range 620–650 K [253]. Out of 8 chains, at most 2 chains contribute to the CDW transport at each CDW state [252]. NbS$_3$-II phase can retain its CDW transport properties down to nanometer scale. The room-temperature CDW transition in this phase has been reported to exhibit promising transport velocity as well as sliding coherence [253]. Room temperature sliding CDW properties makes this phase very prospective for realizing CDW-based nano-oscillator that can operate at room temperature [134].

Like phase-II, NbS$_3$-III is also a superstructure of phase-I, but the monoclinic angle is slightly larger than that of phase-I ($98-99$) [241]. From 100 K to 150 K, this phase follows semiconducting behavior, whereas after $T_{MI} = 155$ K, it undergoes a insulator-to-metal phase transition. The experimental findings of large microwave conductivity and dielectric constant in this phase have been attributed to weakly pinned charge density wave [241]. Moreover, temperature-dependence gating response of phase-III shows that below T_{MI}, there is non-linear conduction beyond a threshold voltage V_{Th}. Similar to sliding

Table 5.1: Lattice parameters of NbS$_3$ phases: **b**, **a** and **c** axes are parallel to the chain, inter-chain, and interlayer directions, respectively. The values in parentheses are converged lattice parameters obtained from DFT calculations.

	a ($\mathring{A}$)	b ($\mathring{A}$)	c ($\mathring{A}$)	β ($°$)
NbS$_3$-I [96, 188]	4.96	6.73	9.14	97.17
(DFT)	(4.98)	(6.78)	(9.25)	(97.16)
NbS$_3$-II [180]	9.90	3.40	18.30	97.00
NbS$_3$-II [250]	9.65	3.35	19.86	110.71
NbS$_3$-III [241]	–	–	–	98~99
NbS$_3$-HP [106]	9.68	3.37	14.83	109.9
NbS$_3$-IV [15]	4.97	6.75	18.13	90.12
(DFT)	(4.98)	(6.78)	(18.29)	(90.11)
NbS$_3$-V [15]	4.95	3.36	9.08	97.35
(DFT)	(4.98)	(3.36)	(9.17)	(97.06)

CDW phenomenon observed in NbSe$_3$ and TaS$_3$, the sharp threshold required for the onset of non-linear conduction has been explained as the driving mechanism which can initiate CDW sliding. However, there is still much uncertainty about whether phase-III and phase-II are essentially the same phase of NbS$_3$, or at least sub-phase of one another [254]. A high-pressure monoclinic phase of NbS$_3$ (NbS$_3$-HP) has also been reported [106]. Similar to Phase-I, this phase is a semiconductor having resistivity of 10^2 Ω·cm at room temperature and does not exhibit any charge density wave transition.

Recently, two new phases of NbS$_3$ have been reported [15]: phase-IV and phase-V. Phase-IV has twice as many chains as phase-I with a doubled **c**-axis, as seen in Fig. 5.1. Phase-V has same structure as phase-I, but the unit cell is halved along the **b** axis and no distortion of Nb atom has been observed. It is quite possible that phase-IV and

phase-V are not a new discovery. Structures similar to phase-IV has been grown earlier having same lattice parameters as phase-IV, and speculated to have monoclinic unit cell [92, 96]. Similarly, a metallic phase similar to phase-V has been reported earlier, exhibiting the superconducting properties around 2 K [91]. However, the structural information and atomic coordinates of NbS_3-IV and NbS_3-V unit-cells have been reported only recently [15].

This paper focuses on the atomic structure of three phases of NbS_3, as shown in Fig. 5.1, which has well established atomic structural information in the literature, namely, NbS_3-I, NbS_3-IV, and NbS_3-V. To discuss their conductivity and transport properties, we study the electronic band dispersion and density of states of NbS_3, using ab initio density functional theory. Moreover, we look into the dynamical instability of each phases by calculating the phonon dispersion and phonon density of states. We also compare the Γ-centered phonon branches with the existing experimental measurement to identify the observed Ramam peaks, as well as to predict any possible CDW ground state.

5.2 Methodology

We perform the structural optimization of all phases of NbS_3, within the framework of density function theory using Perdew-Burke-Ernzerhof (PBE) exchange correlation functionals [175], as implemented in VASP [116, 117]. The plane-wave energy cutoff is chosen as 400 eV. The atomic positions are optimized through the minimization of energy using Hellman-Feynman forces acting on atoms with the Broyden-Flecher-Goldfarb-Shanno (BFGS) scheme. To include van der Waals interaction between the chains, we have applied the semiempirical DFT-D2 Grimme's method [77, 22]. The structure is relaxed until the

forces were less than 10^{-4} eV/Å. A plane wave basis set with kinetic energy cutoff of 400 meV is used to expand the electronic wave functions. A converged Monkhorst Pack k-point mesh of 9×9×3, 8×8×2 and 8×8×4 is adopted for the integration over the first Brillouin zone, for phase-I, phase-IV and phase-V respectively. The optimized lattice constant is within 1% of the experimental lattice constant, as shown in Table 5.1. the high-symmetry points are: **X** (0.5, 0, 0), Γ (0, 0, 0) **Z** (0, 0, 0.5), **Y** (0, 0.5, 0), **B** (0, 0.5, 0.5), **C** (0.5, 0.5, 0).

The phonon dispersion along the BZ path is calculated using a finite displacement scheme implemented in Phonopy [207]. For phase-I, phase-IV and phase-V, the supercell size (k-grid size) is 2×2×2 (10×10×4), 2×2×2 (4×4×2), and 3×3×3 (16×16×2), respectively. The asymptotic long-range dipole-dipole interaction is included as a correction to the interatomic force constants, by calculating the Born effective charge and dielectric tensor.

5.3 Results and discussions

5.3.1 Electronic band structure

In order to understand the CDW transition and anomalous transport properties of different phases of NbS$_3$, it is necessary to calculate the accurate band structure, as well as to figure out the nature of the bands around the Fermi level. NbS$_3$ belongs to group-V chalcogenides. The electronic nature of group-V trichalcogenides, i.e., whether it can be metal, semiconductor or insulator, can be qualitatively understood by the nature of S-S bond [25, 198]. If the S-S bond of the MX$_3$ prismatic chain has stronger covalent p-p bonding (chain type-**A**), the anti-bonding orbital σ_A^* will be higher than the bonding

orbital σ_A. This will ensure semiconducting bands with gap near the Fermi level. On the other hand, when the S-S bond in the chain (type-**B**) is weaker (longer bond length), The bonding orbital is closer to the anti-bonding orbital, revealing more semimetallic or metallic nature of bands. Depending on the number of electron and the chain type **A** and **B**, the electrical properties of quasi-1D materials vary. In case of NbS_3 phase-I and phase-IV, the S-S bond length is 2.014 Å (type-**A**). On the other hand, in NbS_3–V, S-S bond length is 2.14 Å (type-**B**). Hence, we expect NbS_3-I and NbS_3-IV to be semiconducting, whereas NbS_3-V to be metallic or semimetallic. However, depending on the inter-chain interaction, the relative position of anti-bonding band σ_A^* will ultimately determine the actual electrical properties. To resolve the issue, we calculate the complete band structure using *ab initio* density functional theory.

Figure 5.2 show the electronics band structure for phase I, IV and V, at the PBE level of theory. The color profile indicates the % contribution from Nb atom at each band and each k-point of the irreducible Brillouin zone. The Brillouin zone path is shown in supplementary Fig. S1. Due to the dimerization of Nb-Nb bonds, both NbS_3-I and NbS_3-IV are semiconductor, having PBE band gap of 0.30 and 0.22 eV, respectively.
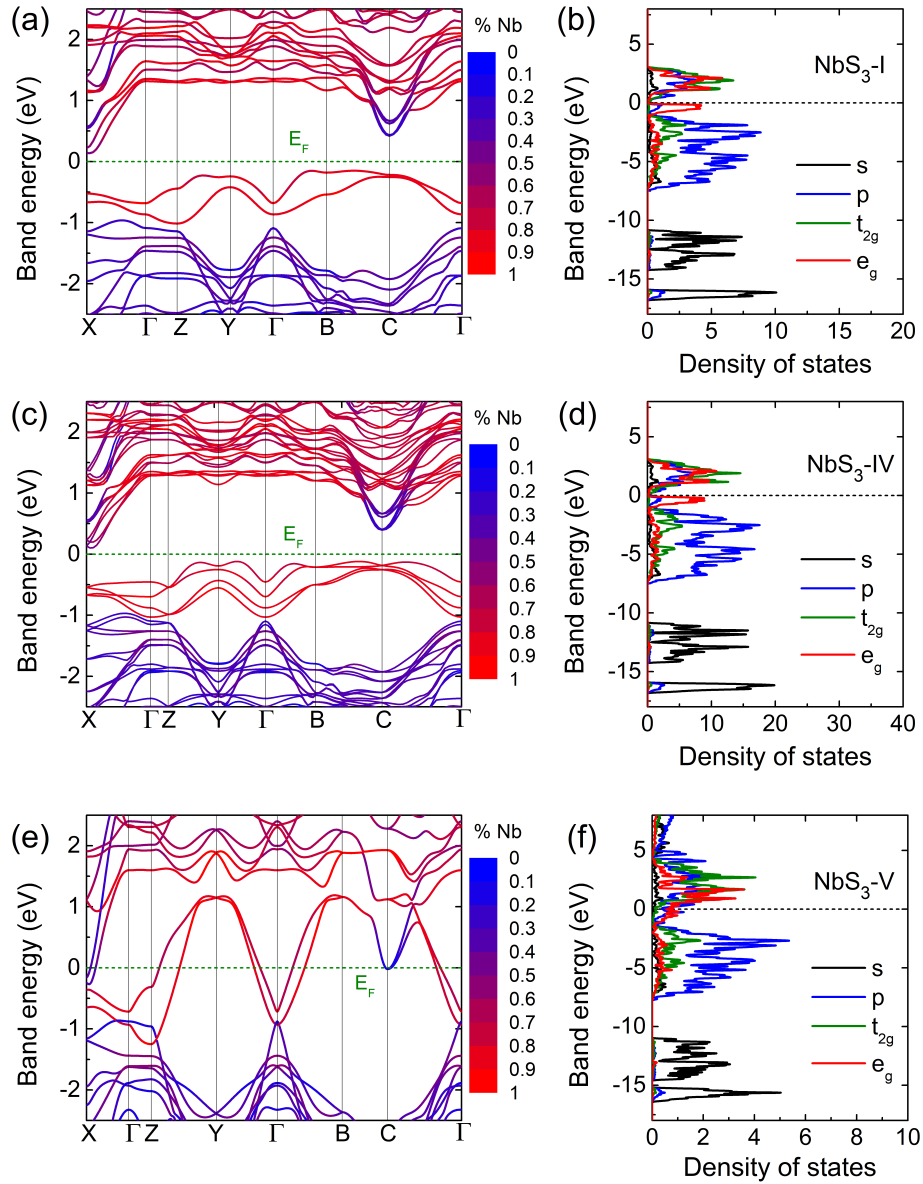
Figure 5.2: Electronic band structure and density of states of NbS$_3$: (a)-(b) Phase-I, (c)-(d) Phase-IV, (e)-(f) Phase-V. The red (blue) color indicates the % contribution of Nb (S) atom at each band. The bands below the Fermi level are dominated by the Nb atom, where the band above the Fermi level is equally controlled by Nb and S atom. The corresponding density of states shows the orbital composition over a wide range of band energy. The relative position of the e$_g$ orbital (red curve), specifically dz^2-orbital, determines the metallic or semiconducting nature of the NbS$_3$ phases. Besides, the similarity between the DOS of NbS$_3$-I and NbS$_3$-IV suggests that these phases are electrically almost identical.

As evident from the band dispersions in Fig. 5.2 (a) and (c), there are certain similarities between the energy bands of phase-I and phase-IV. From the atomic structures in Fig. 5.1 (a)-(b), it is apparent that in case of NbS$_3$-IV, one additional layer of MX$_6$ trigonal prisms is stacked along the van der Waals (vdW) gap direction (**c** direction). Since NbS$_3$ chains are weakly coupled across the vdW gap, phase-IV has almost similar band dispersion as phase-I. However, due to the inter-chain interaction, each phase-IV band in Fig. 5.2 (c) splits into two more bands. The band-splitting is more dominant for the Nb-controlled (red colored) valance bands, whereas the S-controlled bands (blue colored) have very little splitting. This splitting is also the reason for the slightly lower band gap in phase-IV, compared to phase-I.

To understand the degree of anisotropy and nature of one-dimensionality between the phases, we look into the nature of the dispersion along different directions. Both NbS$_3$-I and NbS$_3$-IV valance bands are more dispersive along the chain (Γ-Y direction), whereas bands are less dispersive along the inter-chain direction (Γ-X) and even flatter along the vdW gap direction between the chain bundles (Γ-Z). This explains the anisotropic nature of these semiconducting phases. However, the dispersive nature of the bands along both Γ-Y and Γ-X direction makes these phases more similar to other 2D layered materials, hence NbS$_3$ is more aptly known as quasi-1D material. Moreover, Fig. 5.2 (a) and (c) show that phase-IV valance bands are less dispersive compared to phase-I, specifically for the valance bands near the E_F. Since there are more flat Fermi surfaces in NbS$_3$-IV, we can expect possible nesting vectors, allowing CDW states formation in phase-IV. It should be mentioned that phase-I bands are also relatively flat, but no CDW transition has been

observed yet. However, from the Fermi-surface nesting point of view, phase-IV seems to have higher possibility of exhibiting CDW transition.

Figure 5.2 (b) and (d) show the orbital-decomposed density of states over a wide range of band energy. We can identify four regions in electronic bands having different orbital contributions. Below -10 eV, the orbital composition is dominated by the $3s$ orbital from S atoms. The lowest (around -17 eV) and highest (-14 eV $\sim$ -11 eV) peak regions correspond to the $3s$ bonding and anti-bonding orbitals, and the splitting between them reflects the separation between the two S atoms. Between -1 eV and -7 eV, we can see an admixture of S $3p$ and Nb $4d$-t_{2g} (d_{xy}, d_{yz}, d_{xz}) states, making the Nb-S bond to be ionic in nature, that comes from the weak inter-chain interaction. Above that region and just below the Fermi level, the valance bands are completely dominated by the Nb $4d$-e_g orbitals (d_{z^2}, $d_{x^2-y^2}$), and has a mixture of S $3p$, making the Nb-S atomic to have covalent bonding within the same chain. Hence, the bonding bands below the Fermi level is an admixture of both ionic and covalent character. Above the Fermi level, mostly Nb d-orbital dominates, although near the edge of the conduction bands, S p-orbital also contributes equally. All the three phases show these four regions and their relative position changes from phase to phase.

The mixing of $d_{x^2-y^2}$ and d_{xy} orbitals with the d_{z^2}-orbital influences the shapes of the Fermi surfaces and CDW characteristics [198]. The pairing of the Nb atoms along the metal chain splits the half-filled d_{z^2}-orbital into a filled and empty zone with an energy gap of 0.3 eV [104]. Interestingly, all these orbital-decomposed regions in Fig. 5.2 (b) and (d) look almost same for NbS$_3$-I and NbS$_3$-IV, except the obvious doubling of bands

due to doubled prismatic units in the phase-IV unit cell. Similar to the band structure, this is again an indication that NbS_3-IV is very similar to NbS_3-I, when considered from the electrical and transport point of view. Our calculated density of states of NbS_3-I is consistent with the measured X-ray photoelectron spectra (XPS) [104], which reveals that metal $4d$ levels contribute to the valance band zones, where the chalcogen $3p$ fills the deeper part of the valance band. No XPS studies of NbS_3-IV has been reported in literature yet.

The similarity between the band structures of phase-I and phase-IV can be explained by taking a closer look at their atomic configurations. As evident from Fig. 5.3, phase-IV not only has two times more trigonal prismatic chains along the **c** direction, but also hosts several stacking faults. Comparing the unit cell of phase-I (solid blue box) with the unit cell of phase-IV (black dot box), we find that the top layer of phase-IV is shifted by almost $a/2$ along a direction, hence the need for a larger unit cell to capture this translational shear in NbS_3-IV . This kind of stacking fault is very easy to occur in such weakly-connected chain systems, and reported in other quasi-1D materials like $ZrSe_3$ [90].
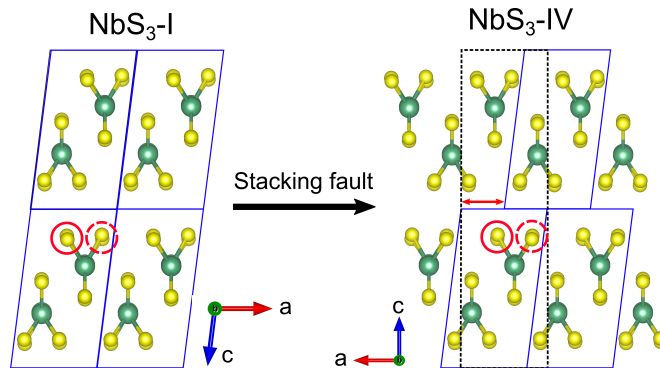
Figure 5.3: Structural differences of NbS_3-IV and NbS_3-I. The unit cell of NbS_3-I is shown in blue, whereas the unit cell of NbS_3-IV is shown in black. NbS_3-IV can be generated by shifting the top layer of NbS_3-I unit-cell by $\sim a/2$ along the a direction, as well as introducing some chiral faults along the b direction.

Moreover, there is a second stacking difference between NbS_3-I and NbS_3-IV, along the growth (**b**) direction. In one of the chain-pairs along **b**, the chirality of the in-plane S-Nb-S bonds switches from being left-handed to right-handed, while unaffecting the other chain-pair in unit cell (marked by red circles). Hence, NbS_3-IV structure is not just a superstructure of NbS_3-I. Given that the layers along **c** direction are loosely connected by the van der Waals interaction, we can expect the sliding and chirality effect will not be that significant along $\Gamma - Z$ direction. Indeed we see that $\Gamma - Z$ bands in phase-IV are merely the zone-folded bands of phase-I. On the contrary, the chirality effect will certainly affect the dispersion along $\Gamma - Y$ (growth) direction, as well as along the $\Gamma - X$ (inter-chain) direction. This is reflected in the dispersions of Fig. 5.2 (a) and (c), where bands along those direction exhibit significant splitting. Note that the valance band along growth direction undergoes major restructuring due to this chirality difference, and creates a Mexican hat type dispersion at Y.

Finally, we look into the third phase of NbS_3, phase-V, in Fig. 5.2 (e)-(f). Contrary to prior two phases, NbS_3-V is a metal. This is expected given that there is no dimerization or Peierls transition in this phase. Moreover, the bands along the chain direction (Γ-Y) and inter-chain direction (Γ-Z) are more dispersive than the vdW direction. It seems, the electrical bands of NbS_3-V are more like quasi-2D in nature than its semiconducting counterpart. The density of states, shown in Fig. 5.2 (f), also have some distinguished features. The deep s-orbitals and p-orbitals arising from S atoms are almost similar to prior phases. However, Note that, the separation between the $3s$ bonding and anti-bonding orbitals is smaller than phase-I and phase-IV. This is expected since the S-S bond are relatively weaker

(type-B) in this phase. Moreover, the e_g orbital no longer have the sharp characteristics, rather it shows a broad spread across the Fermi level, resulting in metallic behavior. In this case, the d_{z^2}-orbital undergoes an incomplete splitting, causing the valance band and conduction band to overlap with each other. Similar to intercalated $NbSe_3$ material [104], intercalation of this phase with Lithium may increase the splitting between the filled and free band zones and exhibit a metal-to-semiconductor transition.

We have also explored the dimensionality effect of phase-I and phase-V (for phase-IV, see chapter 6). In the monolayer limit, only the valance band undergoes some changes, although the overall nature of respective semiconductor or metallic behavior does not change (see Fig. 5.4).
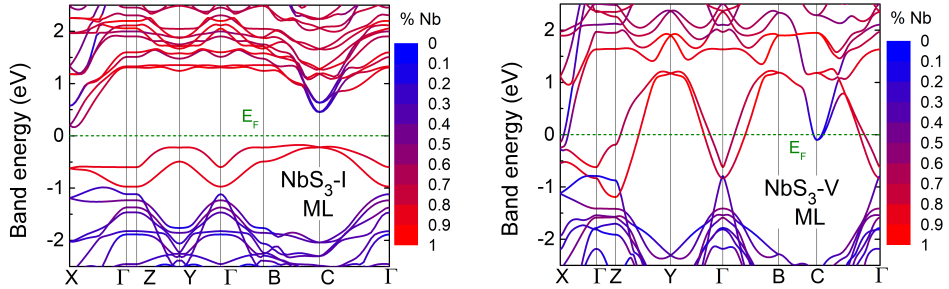
Figure 5.4: Electronic band structure of NbS_3 monolayers. The red (blue) color indicates the % contribution of Nb (S) atom at each band.

5.3.2 Phonon dispersion

To study the dynamical stability of the phases, we have calculated the phonon dispersion of NbS_3-I, NbS_3-IV and NbS_3-V. NbS_3-I belongs to the $P1$ (C_i^1) non-symmorphic space group, and the irreducible representation of this point group symmetry gives 48 normal modes [251], $\Gamma = 24A_g + 24A_u$. Only 24 even-parity modes show Raman activity, whereas

21 odd-parity modes are infrared active. Prior works on phase-I have tried to explain the Raman signatures of NbS_3, by comparing the zone-folded phonon dispersion of ZrS_3 [251]. Although ZrS_3 have similar structure as NbS_3, the dimerization of NbS_3 along the **b** axis is absent in ZrS_3, which introduces uncertainty in translating the results. In this paper, we avoid that by directly calculating the phonon modes using first principle calculation.

Figure 5.5 (a) and (c) show the calculated phonon dispersion along the high symmetry points, for phase-I and phase-IV, respectively. The symbols indicate the prior Raman data in the literature [251, 201, 15]. Unlike other chalcogenides, the NbS_3-I and NbS_3-IV phonon modes cannot be classified by the vibration along the chain and perpendicular to chain directions, due to the symmetry breaking of the screw axis [251]. The high frequency bands beyond 500 cm^{-1} is characterized by the stretching motion of $(S_2)^{2-}$ pairs inside the prismatic chains. As evident in Fig. 5.6, for the top two modes of NbS_3-I (554.27 cm^{-1} and 552.69 cm^{-1}), the $(S_2)^{2-}$ bonds of top and bottom chains vibrate in phase. For the next two phonon branches (537.36 cm^{-1} and 538.29 cm^{-1}), the top $(S_2)^{2-}$ bond stretches, while the bottom one shrinks. The frequency and behavior of these modes are similar for NbS_3-IV. The high frequency of these modes are an indirect indicator that the $(S_2)^{2-}$ bonding in NbS_3-I and NbS_3-IV are stronger than other transition metal trichalcogenides like $ZrSe_3$, HfS_3 [201].

Figure 5.5 (a) and (c) also compares the phonon dispersion with experimental Raman spectra. It is clear that the phonon frequencies at Γ can explain the Raman peaks of NbS_3-I, specifically the highest optical modes around 550 cm^{-1}, as well as the second set of flat bands around 380 cm^{-1} at 70 K. However, the Raman data from Ref. [201] shows one

additional peak in the energy gap region of $400 \sim 500$ cm^{-1}, which might arise due to the overtone of lower phonon branches. In case of phase-IV, the reported Raman peaks show even better agreement with calculated phonon modes. We also look in to the contribution of the atom species on the phonon spectra, by calculating the phonon density of states. As evident from Fig. 5.5 (b) and (d), most of the optical branches in NbS$_3$ phases are controlled by the motion of light Sulfur atoms. However, there is one difference of NbS$_3$-IV bands around 380 cm^{-1}, where the nature of bands changes from being controlled by S atoms to Nb atoms.
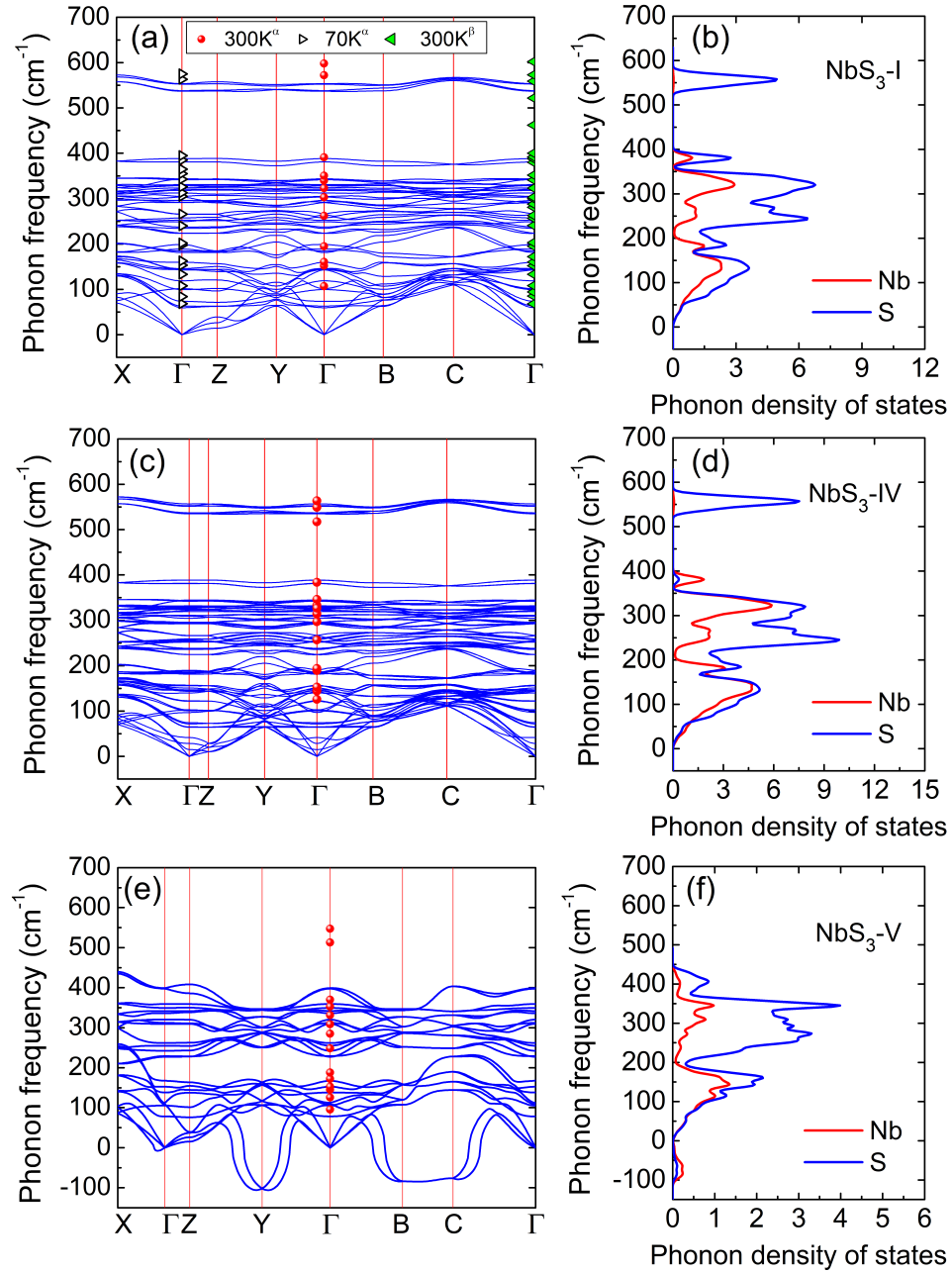
Figure 5.5: Phonon dispersion and phonon density of states of NbS$_3$: (a)-(b) Phase-I, (c)-(d) Phase-IV, (e)-(f) Phase-V. The symbols ∘ and ▷ (symbol ◁) in (a) are the observed Raman peaks from Ref. [251] (Ref. [201]). The symbols in (c) and (e) are from Ref. [15]. The corresponding phonon density of states shows the contribution of the atomic motion from certain type of atom.

Figure 5.5 (e) shows the phonon dispersion of phase-V. NbS$_3$-V belongs to the P2$_1$/m symmetry group, which has twofold screw symmetry axis parallel to b-axis, an inversion center and a mirror plane. Similar to ZrSe$_3$, the expected 24 normal phonon modes from NbS$_3$-V can be decomposed in to the following irreducible representation at Γ point: $\Gamma = 8A_g + 4B_g + 4A_u + 8B_u$. Among them, the optical modes 8A$_g$ and 4B$_g$ are Raman-active even-parity modes, whereas the rest 2A$_u$ and 7B$_u$ are infrared-active odd-parity modes. However, when we calculate the full phonon dispersion using the reported atomic structure of NbS$_3$-V [15], several negative phonon branches appear in the dispersion. This negative modes are an indicator of possible instability present in this phase, making it a promising candidate for hosting CDW. As seen in Fig. 5.5 (e), two phonon modes become unstable (negative) after $^3/_5 \sim {}^4/_5$ of the Brillouin zone along $\Gamma - Y$ (growth) direction (specifically after 73.8% and 58.6% of BZ length for the two modes), Similarly, one mode along $\Gamma - X$ (inter-chain) direction becomes negative up to almost $^1/_3$ (22.4%) of the BZ.
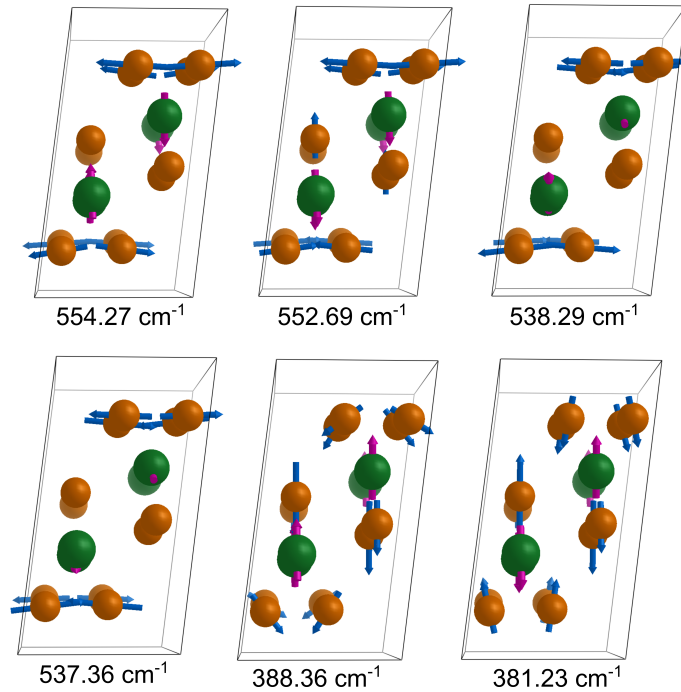
Figure 5.6: Six highest phonon modes of NbS$_3$-I.

The instability in the phonon dispersion reveals two important things. First, the reported structure is not a CDW commensurate ground state, rather a high-temperature incommensurate phase of NbS$_3$-V. Second, the possible CDW ground state, which will suppress these instabilities, will be a supercell structure of NbS$_3$-V, where the supercell will be 3 times longer along inter-chain (**a**) direction and 5 times longer along growth (**b**) direction. The elongation of the original phase-V supercell will ensure that the Nb atoms in those direction can dimerize and subsequently lower the energy of the NbS$_3$-V CDW ground state. This is also in agreement with prior literature, where such large supercell structures have been speculated to be the case for some others phases of NbS$_3$. This insight can guide the experimental efforts to resolve the CDW commensurate structure of phase-V, by X-ray

diffraction and detailed TEM studies.

We have also compared the Raman peaks with the phonon dispersion of phase-V in Fig. 5.5 (e). The high-energy peaks around 550 cm^{-1} do not match with any phonon branches nearby. Such high frequency modes generally arise from the deformation of S-S bonds, as we have seen in semiconducing phases. In phase-V, we can estimate the tentative position of these modes arising from S-S stretching bonds, using Steudel's empirical relationship based on bond length d_{S-S} [203],

$$d_{S-S} \; (\mathring{A}) = 2.57 - 9.47 \times 10^{-4} \, \nu_{S-S} \; (cm^{-1}). \tag{5.1}$$

For phase-I and phase-IV, Eq. (5.1) suggests that the S-S stretching mode will be around 584 cm^{-1}, whereas the DFT calculated modes are around 554 cm^{-1}. On the contrary, in phase-V, the stretching modes from Eq. (5.1) should be around 452 cm^{-1}, corresponding to the DFT calculated modes around 400 cm^{-1}. This further indicates that the observed Raman peaks around 550 cm^{-1} (inside black circle) can not arise from reported atomic configuration of phase-V. Rather, it is possible that there is some low-temperature commensurate phases already present in the NbS$_3$-V samples having stronger S-S bonds, and giving rise to those high-energy peaks.

5.4 Conclusion

In this paper, we have explored the electronic and vibrational properties of different phases of NbS$_3$, using ab initio density functional theory. The electronic band dispersion reveals that, like phase-I, phase-IV is semiconductor with band gap of 0.22 eV at the PBE level of theory. From the nature of the dispersion, it seems phase-IV has higher

probability of exhibiting CDW transitions than phase-I. Although phase-IV has several stacking and chiral faults, the similarity of the structures between phase-IV and phase-I results in similar electronic behavior. On the contrary, phase-V is a metal, with weaker S-S bonds compared to other phases. The density of states, when decomposed to individual orbital contributions, can explain the relative transition from semiconducting to metallic transition between phases. Moreover, we have calculated the phonon dispersion and density of states of these phases. We find that the dimerized phases, namely NbS_3-I and NbS_3-IV, are dynamically stable. However, several unstable modes are observed in NbS_3-V, indicating that there is a probable CDW ground state remained to be discovered for this phase.

Chapter 6

Electronic properties and band alignment of quasi-1D materials

6.1 Introduction

Two-dimensional layered materials, where the layers are separated by weak van der Waals force, provides a great opportunity to substantially eliminate the interface dangling bonds [60]. Among them, the semiconducting 2D materials is promising for designing efficient tunneling devices through a "broken-gap" band alignment [72], resulting in a wide variety of tunnel transistors [124, 87, 125], sensors [111, 246, 153] and field effect transistors [177, 190, 181]. On the other hand, the metallic 2D materials are very promising as efficient contacts in its scaled form [98, 43, 34, 71]. Moving forward with the dimensional scaling, the quasi-1D materials seem to be more interesting in terms of contact engineering [95]. The quasi-1D materials, specifically transition metal trichalcogenides (TMTs) grow in a

chain-like formations. Many TMTs retain their properties, even up to single layer, making

the devices less susceptible to growth thickness. The electronic and optical properties of

some of the TMTs have been studied [170, 59, 105, 75, 171]. However, the prior theoretical

efforts were mostly limited to the band calculation of semiconducting TMTs, e.g. ZrX_3 and

HfX_3 [95]. The band alignment of most of the quasi-1D materials, specifically the metallic

ones, are still absent in literature.

In this work, we calculate the electronic band dispersion and band alignment of

several transition metal trichalcogenides, with the purpose to find suitable metallic quasi-1D

materials with better contact characteristics. The metallic TMTs can pave the way towards

ultimate scaling of the contacts, as well as can revolutionize the integration of 1D materials

with existing 2D and bulk electronics.
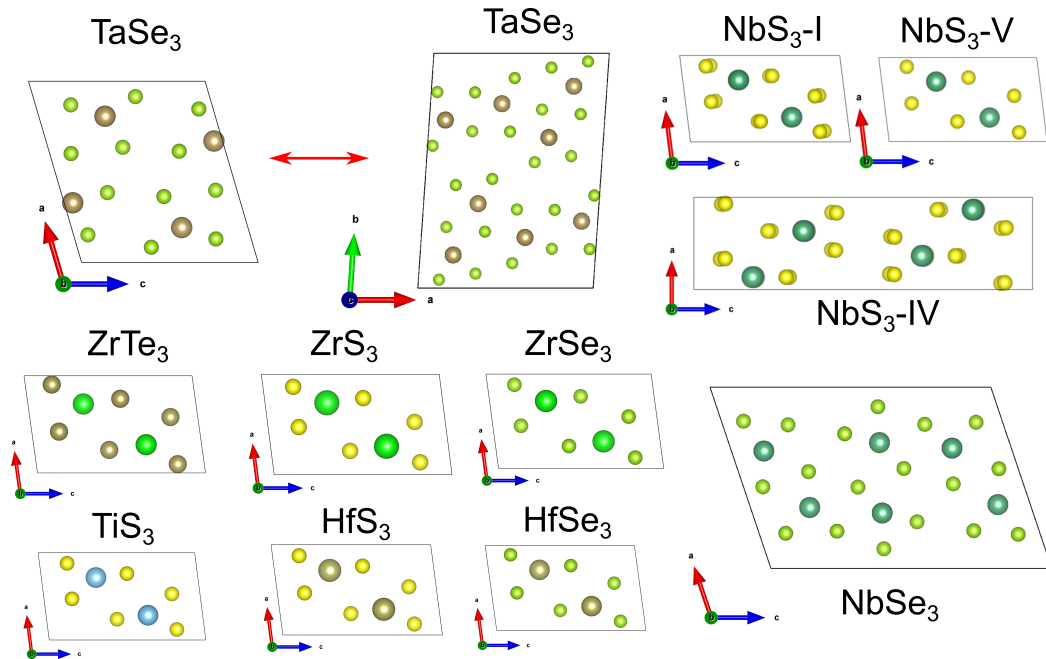
Figure 6.1: Atomic configurations of quasi-1D materials.

6.2   Methodology

We perform the structural optimization of MX_3, within the framework of density function theory using Perdew-Burke-Ernzerhof (PBE) exchange correlation functionals [175], as implemented in VASP [115, 114]. The structures we consider here are shown in Fig. 6.1. The plane-wave energy cutoff is chosen as 400 eV. The atomic positions are optimized through the minimization of energy using Hellman-Feynman forces acting on atoms with the Broyden-Flecher-Goldfarb-Shanno (BFGS) scheme. To include van der Waals interaction between the chains, we have applied the semiempirical DFT-D2 Grimme's method [77, 22]. The structure is relaxed until the forces were less than 10^{-4} eV/Å. A plane wave basis set with kinetic energy cutoff of 400 meV is used to expand the electronic wave functions. A converged Monkhorst Pack k-point mesh of $9\times9\times3$ is adopted for the integration over the first Brillouin zone. The DFT calculated lattice constants are shown in Table 6.1, which are close to the experimental lattice constants. For the hybrid functional correction, we use Heyd-Scuseria-Ernzerhof (HSE) calculation [83], where the fraction of screened Fock exchange α was set to 0.25. The high-symmetric points in the Brillouin zone, for $TaSe_3$ and NbX_3 dispersions, are denoted as: **X** (0.5, 0, 0), Γ (0, 0, 0) **Z** (0, 0, 0.5), **Y** (0, 0.5, 0), **B** (0, 0.5, 0.5), **C** (0.5, 0.5, 0). For $NbSe_3$, TiX_3, ZrX_3 and HfX_3 dispersions, the high-symmetric points are: Γ (0, 0, 0), **Y** (0, 0.5, 0), **C** (0, 0.5, 0.5), **Z** (0, 0, 0.5), **D** (0.5, 0, 0.5), **E** (0.5, -0.5, 0.5), **A** (0.5, -0.5, 0), **B** (0.5, 0, 0).

To calculate the band alignment, we first obtain a monolayer slab by incorporating sufficient vacuum level of 20 $\mathring{A}$. The work function is subsequently calculated by taking the electrostatic energy difference between the vacuum level and the Fermi level.

Table 6.1: Lattice parameters of MX_3 phases. The metallic phases are shown in bold faces. **b**, **a** and **c** axes are parallel to the chain, inter-chain, and interlayer directions, respectively. The values in parentheses are converged lattice parameters obtained from DFT calculations.

	a (Å)	b (Å)	c (Å)	β (°)
TaSe$_3$ [11]	10.411	3.494	9.836	106.36
(DFT)	(10.412)	(3.514)	(9.744)	(106.36)
NbS$_3$-I [96, 188]	4.96	6.73	9.14	97.17
(DFT)	(4.98)	(6.78)	(9.25)	(97.16)
NbS$_3$-IV [15]	4.97	6.75	18.13	90.12
(DFT)	(4.98)	(6.78)	(18.29)	(90.11)
NbS$_3$-V [15]	4.95	3.36	9.08	97.35
(DFT)	(4.98)	(3.36)	(9.17)	(97.06)
NbSe$_3$ [222]	10.009	3.480	15.629	109.47
(DFT)	(10.465)	(3.422)	(15.42)	(108.65)
TiS$_3$ [66]	4.958	3.401	8.778	97.32
(DFT)	(4.992)	(3.401)	(8.906)	(97.26)
HfS$_3$ [66]	5.092	3.595	8.967	97.38
(DFT)	(5.027)	(3.604)	(8.826)	(97.44)
HfSe$_3$ [66]	5.388	3.722	9.428	97.38
(DFT)	(5.391)	(3.710)	(10.092)	(96.18)
ZrS$_3$ [66]	5.124	3.624	8.98	97.28
(DFT)	(5.168)	(3.634)	(9.687)	(96.73)
ZrSe3$_3$ [66]	5.411	3.749	9.44	97.48
(DFT)	(5.445)	(3.761)	(10.08)	(97.30)
ZrTe$_3$ [66]	5.894	3.926	10.10	97.82
(DFT)	(5.915)	(3.881)	(10.154)	(97.93)

6.3 Results and discussions

6.3.1 TaSe$_3$

Monoclinic TaSe$_3$ has four prismatic chains in the bulk unit cell, as shown in Fig. 6.1. There is only a single phase of TaSe$_3$ reported, which exhibits metallic conduction ($\sim$6 $\times$ 10^{-6} Ω·m) [11, 10, 79] and temperature-dependent diamagnetism [230]. No CDW phase is observed in TaSe$_3$, because of comparatively much stronger dispersion along x-z plane [24]. TaSe$_3$ remains metallic up to the helium temperature [192, 79]. Superconducting properties has been also observed below 2.1 K [192, 79, 229, 158, 157].

As evident from the lattice vectors, the in-plane vectors **a** and **c** are not along the interchain or vdW direction. Due to the slanted nature of the coordinates, it is harder to create monolayer for theoretical calculations. Moreover, along the vdW gap, TaSe$_3$ do not have a planar interface, rather shows a corrugated surface. To overcome this issue, we use a coordinate transformation to align the axes along the interchain and interlayer vdW direction. Subsequently, by adding vacuum layer to the modified structure, we can simulate the corresponding monolayer structure.

Figure 6.2 shows the band structure TaSe$_3$ for bulk and monolayer. Evidently, TaSe$_3$ is a metal even up to monolayer limit. This indicates that as a candidate for contact, TaSe$_3$ can remain consistently a metal, irrespective of the lateral dimensions of the chains. Around the Fermi level, several pockets of flat bands are observed, arising from overlapping of Se-controlled valance bands and Ta-controlled conduction bands. The overlapping is reduced in case of monolayer. Further cleavage of TaSe$_3$ along the interchain direction may remove the overlapping, but that would create unwanted dangling bonds. The orbital-

96

decomposed band plot suggests that mainly the metal $d_{x^2-y^2}$ and chalcogen $p_{y,z}$ control the metallic behavior in bulk. However, in monolayer, it is the Ta-d_{z^2} orbital that actively determines the electrical nature in this material.

6.3.2 NbX$_3$

NbS$_3$-I is a semiconductor with triclinic structure of P$\bar{1}$ symmetry [96, 188, 147]. The Nb atoms are displaced by 0.16 Å from the mirror plane, causing a linear peierls distortion [188]. NbS$_3$ remains semiconducting over a wide range of temperature from 4.2 K to 650 K [53]. Apart from the well-known NbS$_3$-I, two new phases of NbS$_3$ have been reported recently [15]. Phase-IV has twice as many chains as phase-I, having a doubled **c**-axis, as seen in Fig. 6.1. Phase-V has same structure as phase-I, but the unit cell is halved along the **b** axis. Unlike the other two phases, no dimerization of Nb atom has been observed in NbS$_3$-V.

Figure 6.3, 6.4 and 6.5 shows the band structure NbS$_3$-I, NbS$_3$-IV and NbS$_3$-V, respectively, for both bulk and monolayer. NbS$_3$-I and NbS$_3$-IV are semiconductor, whereas NbS$_3$-V is a metal. In both bulk and monolayer NbS$_3$-I, the CBM is controlled by the Nb-d_{xz}, whereas the VBM is controlled by the localized Nb-d_{z^2} orbital. Almost similar electrical behavior is observed in case of NbS$_3$-IV. This is expected given that NbS$_3$-I and NbS$_3$-IV have almost similar structure, except exhibiting some stacking faults across the vdW gaps.

Contrary to phase-I and phase-IV, phase-V is metallic up to monolayer, where the bands near the Fermi level is controlled by the Nb-d_{z^2}, $d_{x^2-y^2}$, as well as the S-p_x. In the

monolayer limit, the overlapping between the orbitals increases more.

NbSe$_3$ is a well-known metallic quasi-1D materials that can also exhibit charge density waves [222]. The calculated band structure, as shown in Fig. 6.6, shows that NbSe$_3$ remains metallic when scaled down to monolayer. Mainly the Nb-$d_{x^2-y^2}$ orbital and S-p_y orbital determines the metallic behavior in NbSe$_3$.

6.3.3   TiS$_3$

The prior electrical and transport measurements of bulk TiS$_3$ show that, at room temperature, the bulk TiS$_3$ is an n-type semiconductor with carrier mobility of 30 cm^2/Vs [41]. Optical absorption measurements has also been reported for bulk TiS$_3$, exhibiting an optical gap about 1 eV [58]. We look in to the band dispersion of TiS$_3$ at the PBE level of theory, and find $\sim$0.2 eV band gap. This is consistent with previous theoretical calculations [41]. The element-decomposed and mode-decomposed band plots show that the conduction band minimum (CBM) is controlled by Ti-d_{z^2}, whereas the valance band maximum (VBM) is dominated by the S-p_x.

6.3.4   ZrX$_3$

The electronic [95] and Raman properties [169] of ZrTe$_3$ has been studied by several groups. Here, we look in to their electronic properties to evaluate the band alignment with respect to other members of quasi-1D family. ZrS$_3$ and ZrSe$_3$ are both semiconductor. As seen in Fig. 6.8 and Fig. 6.9, the VBM in both cases remain almost similar, and is dominated by the chalcogen-p_y orbital. However, on the CBM, localized d_{z^2} orbital dominates in ZrS$_3$,

while p_x orbital contributes most in ZrSe$_3$. On the other hand, ZrTe$_3$ is a metal, as evident in Fig. 6.10, with p orbitals mostly controlling the bands near the Fermi energy. Going from bulk to monolayer, there is also a significant increase in electronic density of states, as evident by the emergence of several flat bands at E_F.

6.3.5   HfX$_3$

Finally, we calculate the band structure of Hf-based TMTs. Some electronic and phononic properties of HfX$_3$ has already been reported [1]. We look in to their electrical properties going from bulk to monolayer, to extract the band alignment information. As seen in Fig. 6.11, HfS$_3$ is a strong semiconductor, even at the PBE level of theory. On the other hand, HfSe$_3$ is almost semimetallic, as seen in Fig. 6.12. Going from S to Se, the p_x orbital in the conduction band comes down, whereas the p_y orbital goes up. The effect is less pronounced in monolayer HfSe$_3$.

6.3.6   Band alignment

We compare the relative band alignment of all the aforementioned quasi-1D materials. All the band energy levels in Fig. 6.2 - 6.12 are calibrated with respect to the same vacuum energy level. We can see that several of the materials create broken band alignment, e.g. (NbS$_3$, TiS$_3$) and (NbS$_3$, HfS$_3$), which is promising for tunneling FET. However, with higher-order correction (HSE), this broken gap can turn into a Type-II band alignment. We can also see that the Fermi level of metallic TMTs remains relatively constant (around

-5 eV), at the PBE level of theory. Mixing with the semiconductor TMTs, limited combinations are possible where ohmic contacts can be fabricated, e.g. $TaSe_3$ and TiS_3, $NbSe_3$ and TiS_3, $NbSe_3$ and $HfSe_3$. However, most of the other combinations will create schottky barrier during the contact.

6.4   Conclusion

We have calculated the band structure, atomic contribution and orbital contribution for different quasi-1D TMT materials, for both bulk and monolayer. Using the monolayer geometry, the band alignment of the TMTs are calculated with respect to the absolute vacuum level. Several material combinations are promising for TMT-based tunnel FETs. On the other hand, depending on the material combinations, several metallic TMTs can provide efficient ohmic contacts to electronic devices.
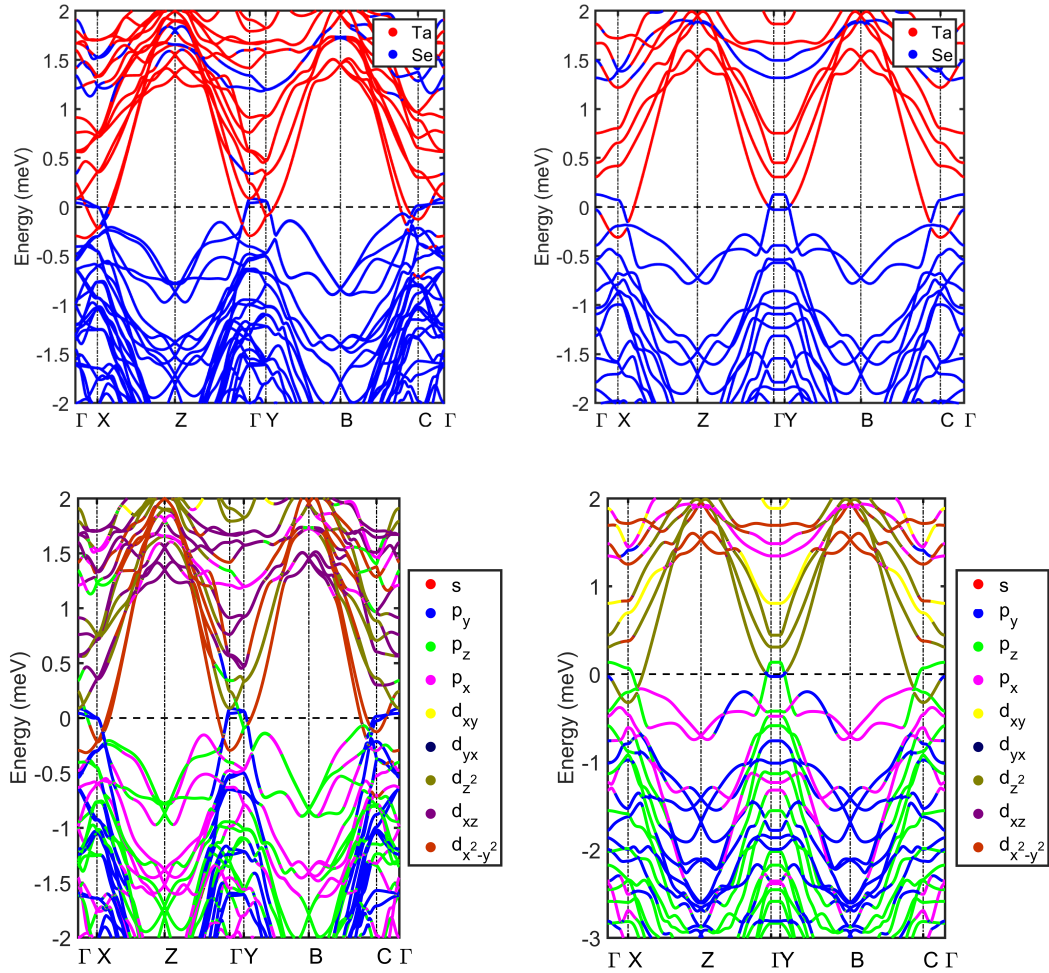
Figure 6.2: Band diagram of (a) bulk TaSe$_3$, and (b) monolayer TaSe$_3$. The color indicates the maximum contribution of either metal or chalcogen atom at each k-point. Band diagram of (c) bulk TaSe$_3$, and (d) monolayer TaSe$_3$, where the color indicates the maximum contribution of atomic orbitals at each k-point.
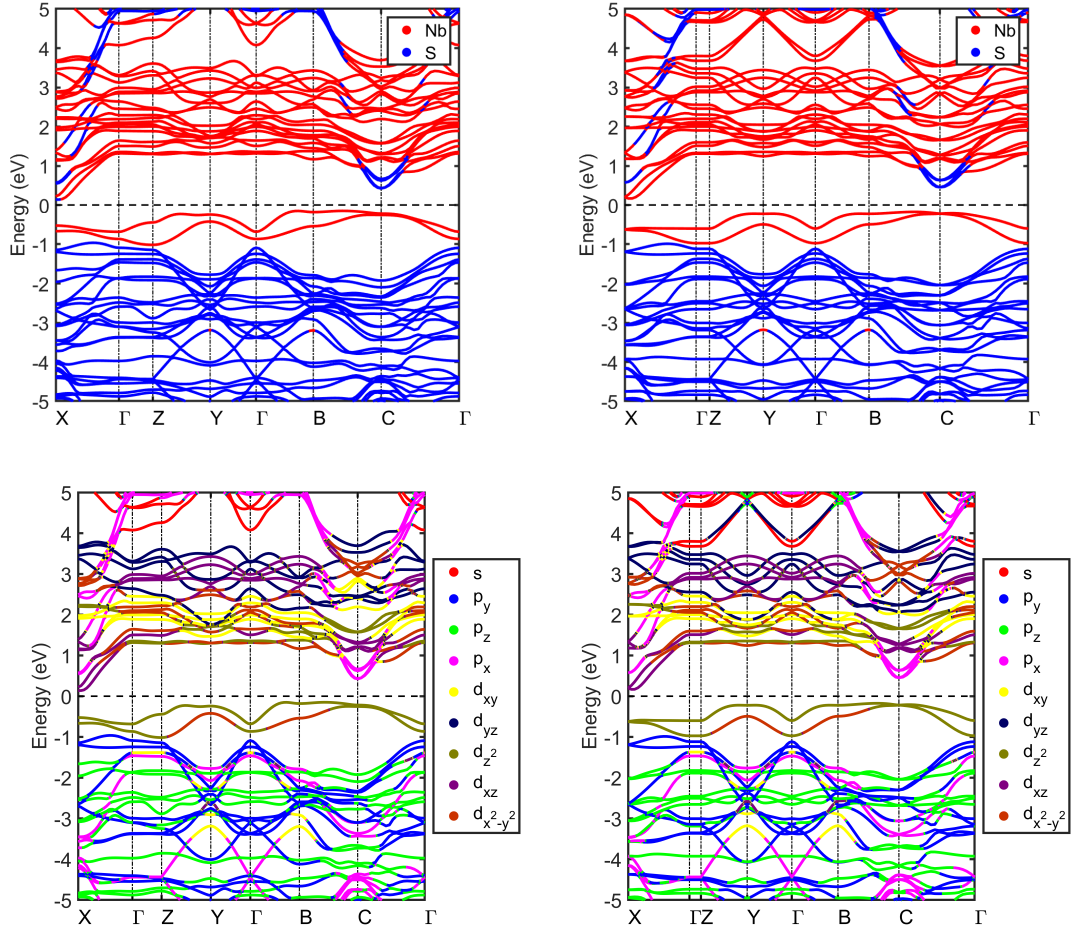
Figure 6.3: Band diagram of (a) bulk NbS$_3$-I, and (b) monolayer NbS$_3$-I. The color indicates the maximum contribution of either metal or chalcogen atom at each k-point. Band diagram of (c) bulk NbS$_3$-I, and (d) monolayer NbS$_3$-I, where the color indicates the maximum contribution of atomic orbitals at each k-point.
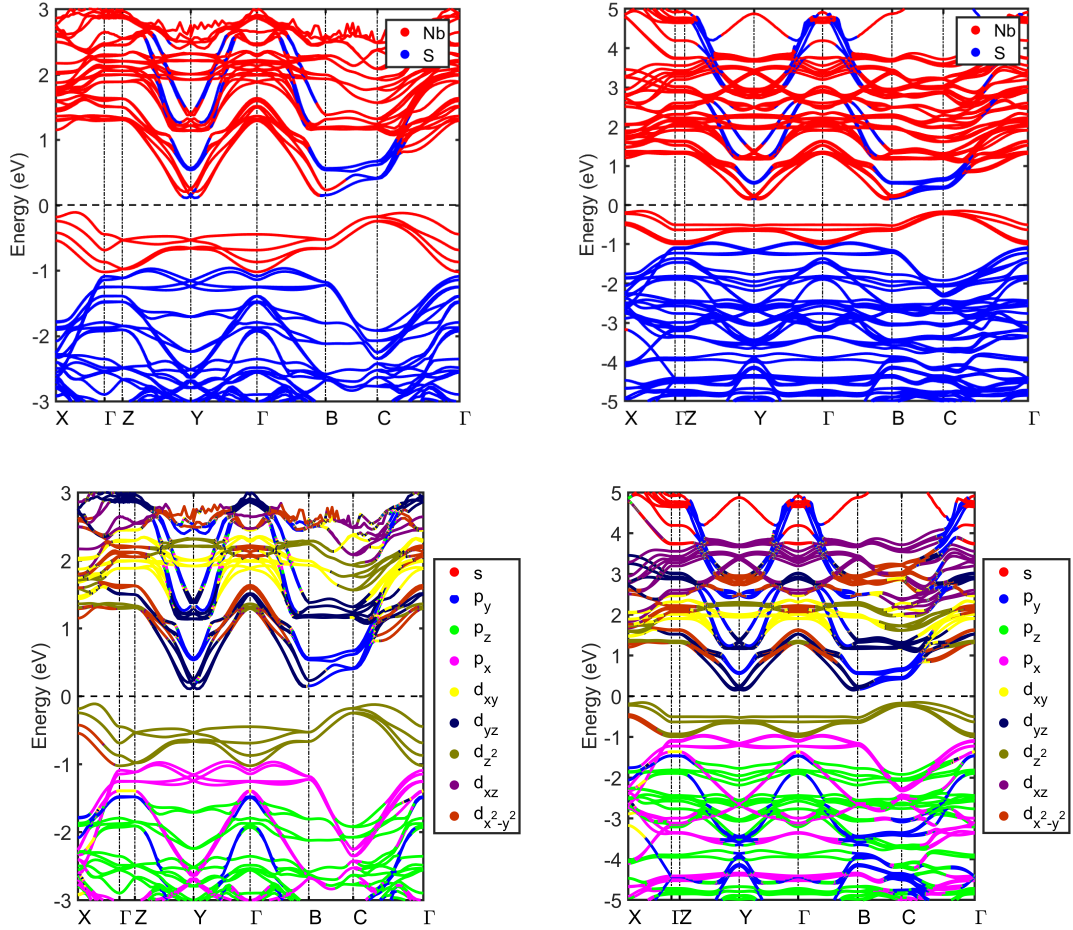
Figure 6.4: Band diagram of (a) bulk NbS$_3$-IV, and (b) monolayer NbS$_3$-IV. The color indicates the maximum contribution of either metal or chalcogen atom at each k-point. Band diagram of (c) bulk NbS$_3$-IV, and (d) monolayer NbS$_3$-IV, where the color indicates the maximum contribution of atomic orbitals at each k-point.
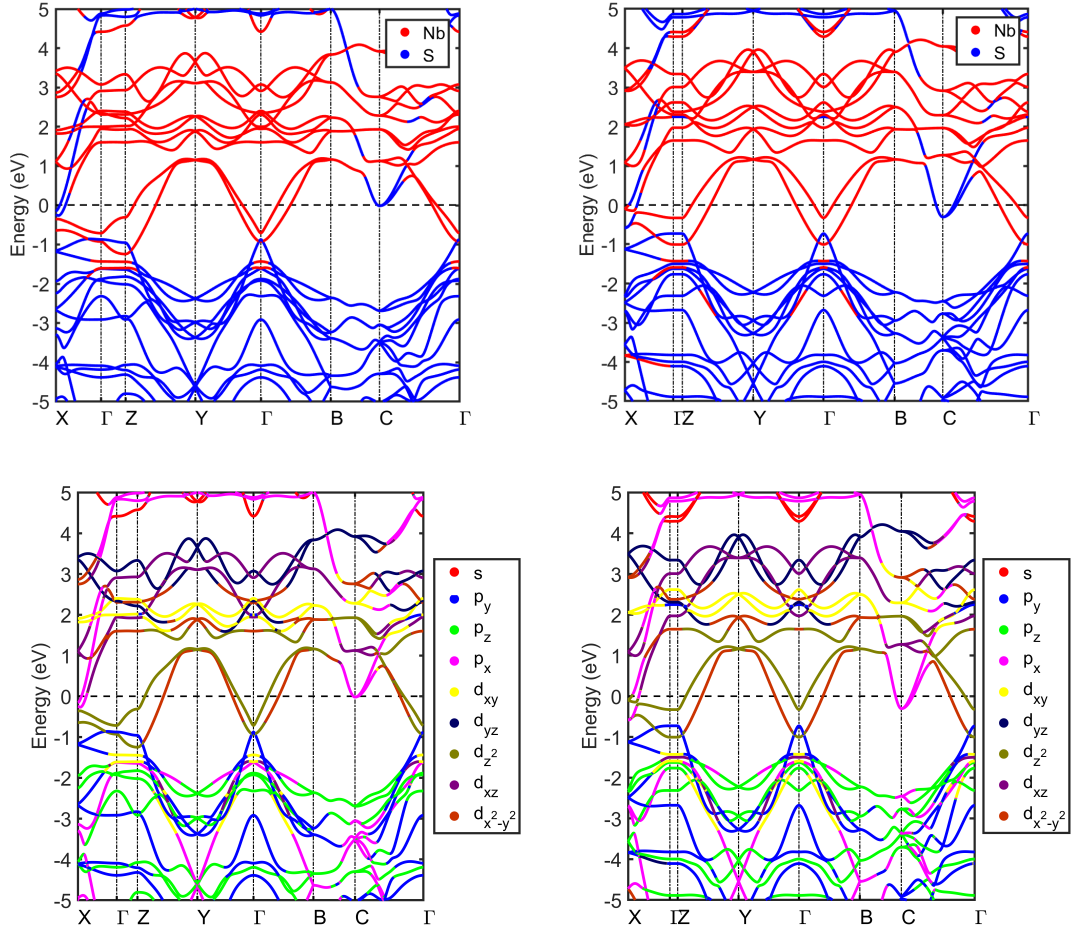
Figure 6.5: Band diagram of (a) bulk NbS$_3$-V, and (b) monolayer NbS$_3$-V. The color indicates the maximum contribution of either metal or chalcogen atom at each k-point. Band diagram of (c) bulk NbS$_3$-V, and (d) monolayer NbS$_3$-V, where the color indicates the maximum contribution of atomic orbitals at each k-point.
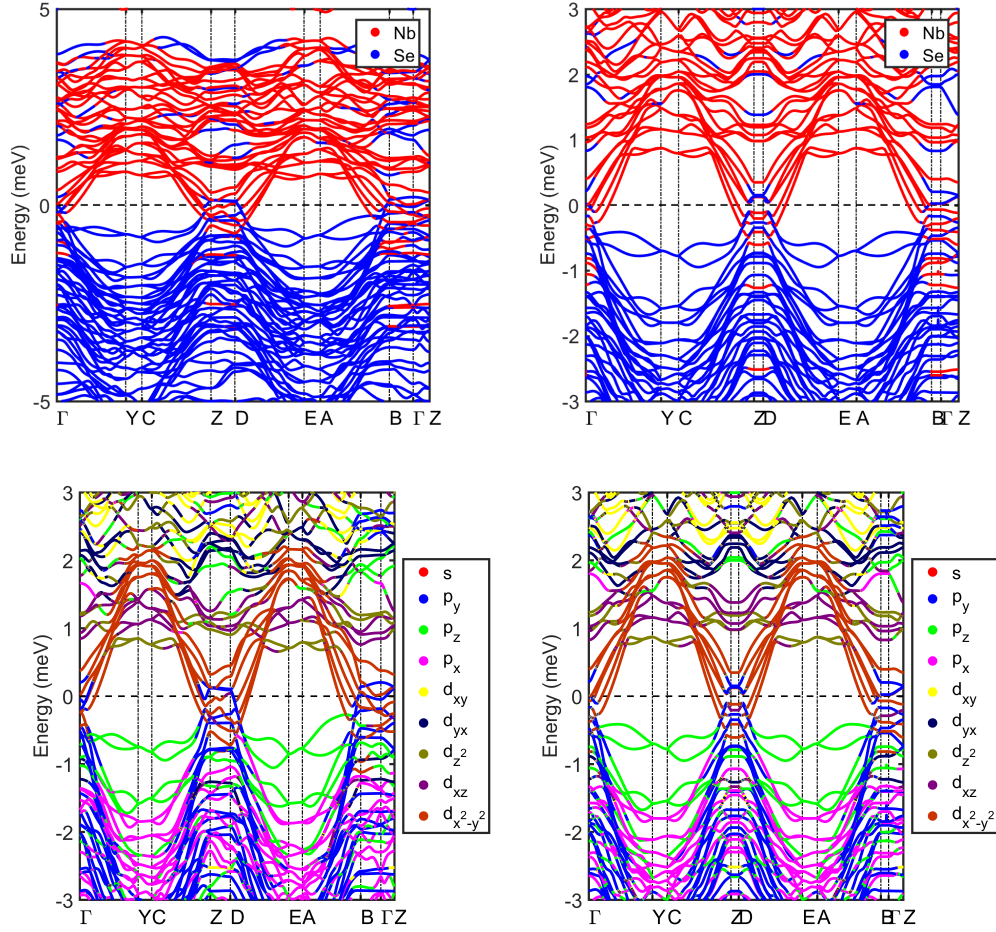
Figure 6.6: Band diagram of (a) bulk NbSe$_3$, and (b) monolayer NbSe$_3$. The color indicates the maximum contribution of either metal or chalcogen atom at each k-point. Band diagram of (c) bulk NbSe$_3$, and (d) monolayer NbSe$_3$, where the color indicates the maximum contribution of atomic orbitals at each k-point.
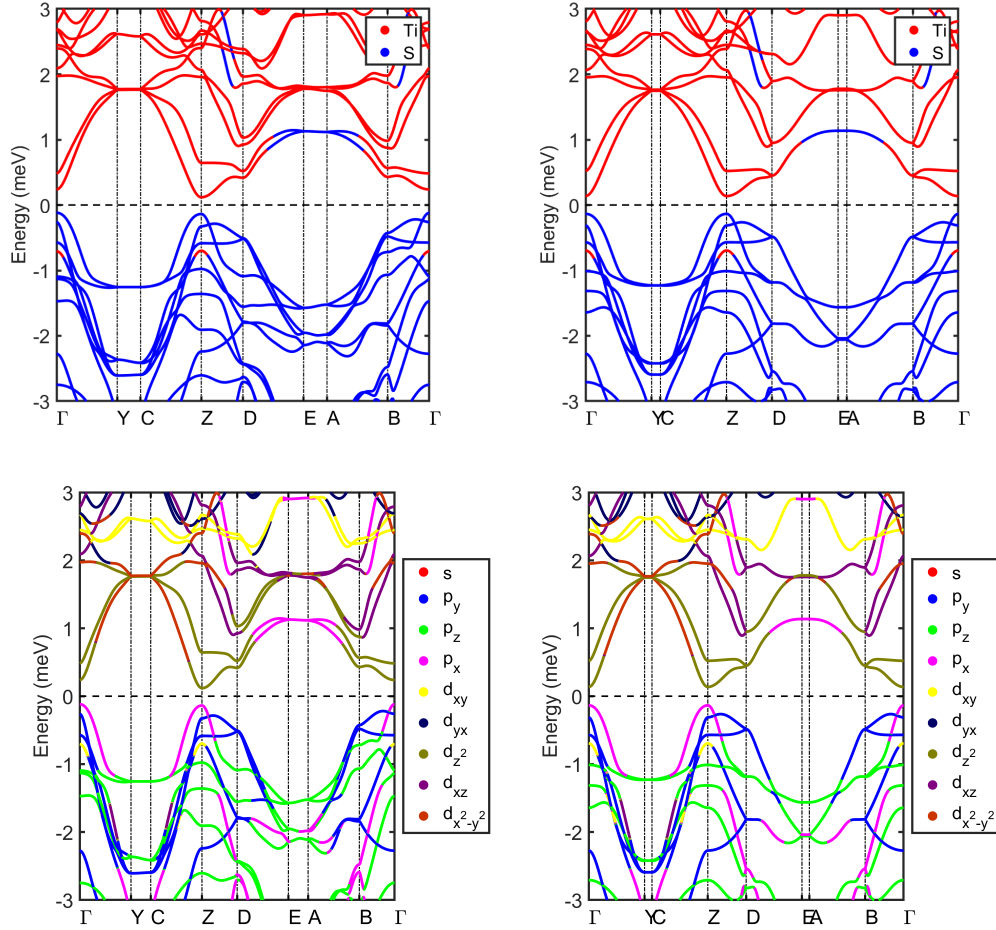
Figure 6.7: Band diagram of (a) bulk TiS$_3$, and (b) monolayer TiS$_3$. The color indicates the maximum contribution of either metal or chalcogen atom at each k-point. Band diagram of (c) bulk TiS$_3$, and (d) monolayer TiS$_3$, where the color indicates the maximum contribution of atomic orbitals at each k-point.
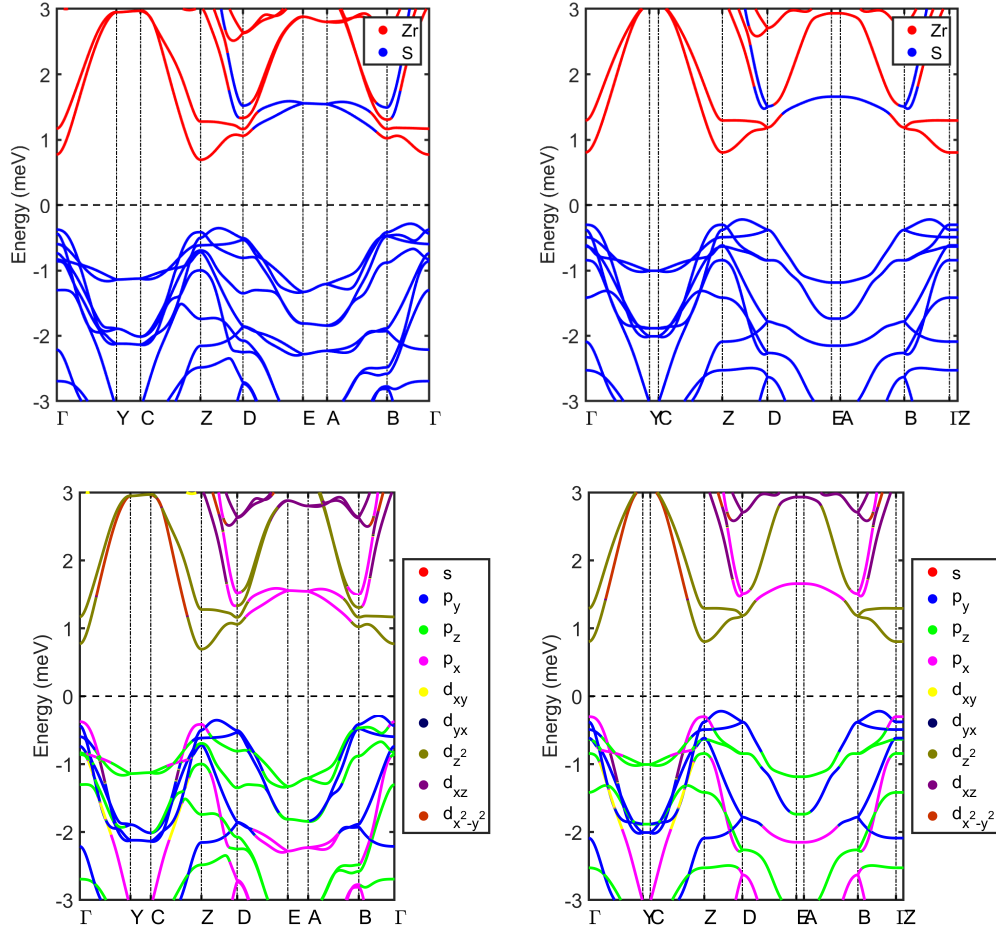
Figure 6.8: Band diagram of (a) bulk ZrS_3, and (b) monolayer ZrS_3. The color indicates the maximum contribution of either metal or chalcogen atom at each k-point. Band diagram of (c) bulk ZrS_3, and (d) monolayer ZrS_3, where the color indicates the maximum contribution of atomic orbitals at each k-point.
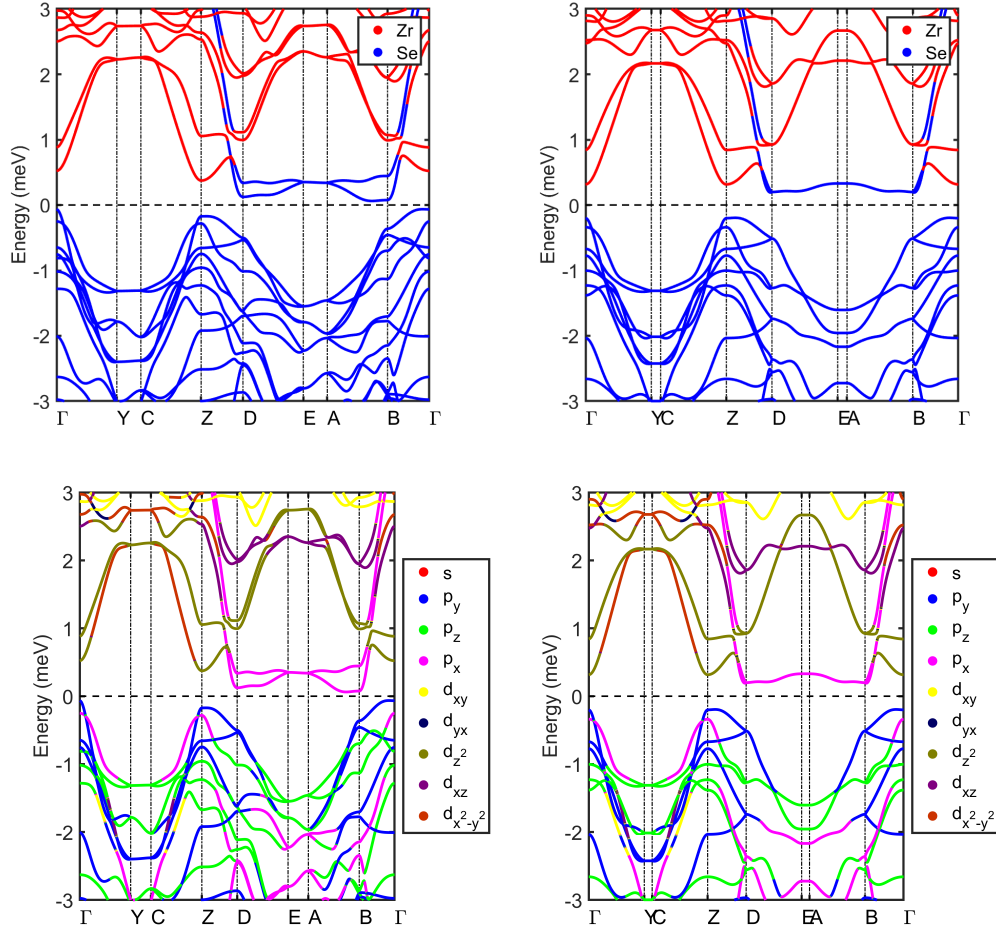
Figure 6.9: Band diagram of (a) bulk ZrSe$_3$, and (b) monolayer ZrSe$_3$. The color indicates the maximum contribution of either metal or chalcogen atom at each k-point. Band diagram of (c) bulk ZrSe$_3$, and (d) monolayer ZrSe$_3$, where the color indicates the maximum contribution of atomic orbitals at each k-point.
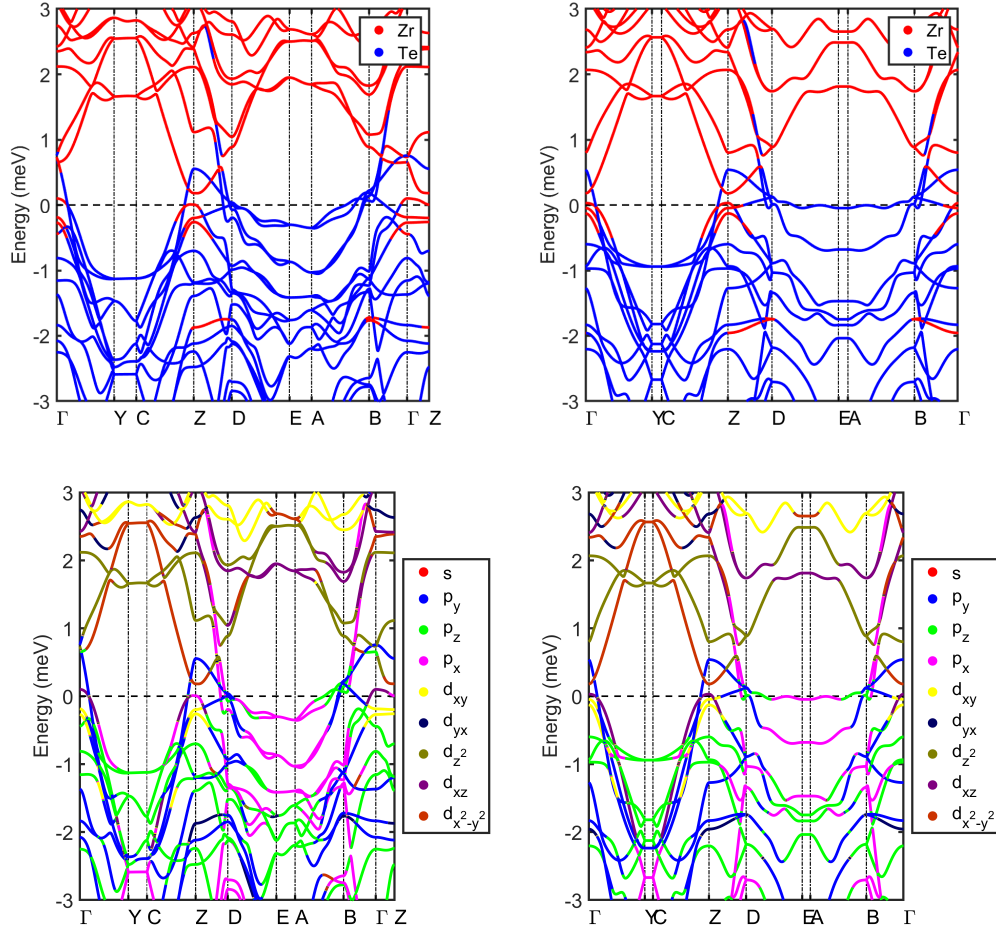
Figure 6.10: Band diagram of (a) bulk ZrTe$_3$, and (b) monolayer ZrTe$_3$. The color indicates the maximum contribution of either metal or chalcogen atom at each k-point. Band diagram of (c) bulk ZrTe$_3$, and (d) monolayer ZrTe$_3$, where the color indicates the maximum contribution of atomic orbitals at each k-point.
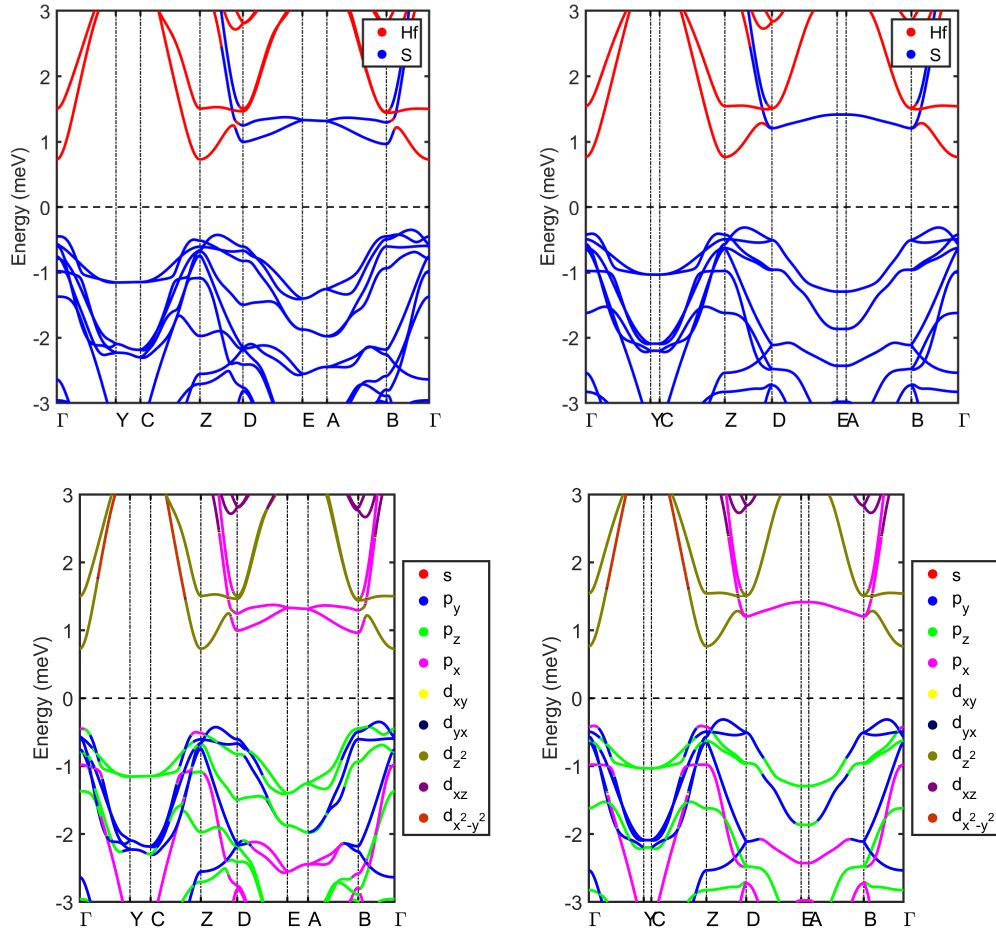
Figure 6.11: Band diagram of (a) bulk HfS$_3$, and (b) monolayer HfS$_3$. The color indicates the maximum contribution of either metal or chalcogen atom at each k-point. Band diagram of (c) bulk HfS$_3$, and (d) monolayer HfS$_3$, where the color indicates the maximum contribution of atomic orbitals at each k-point.
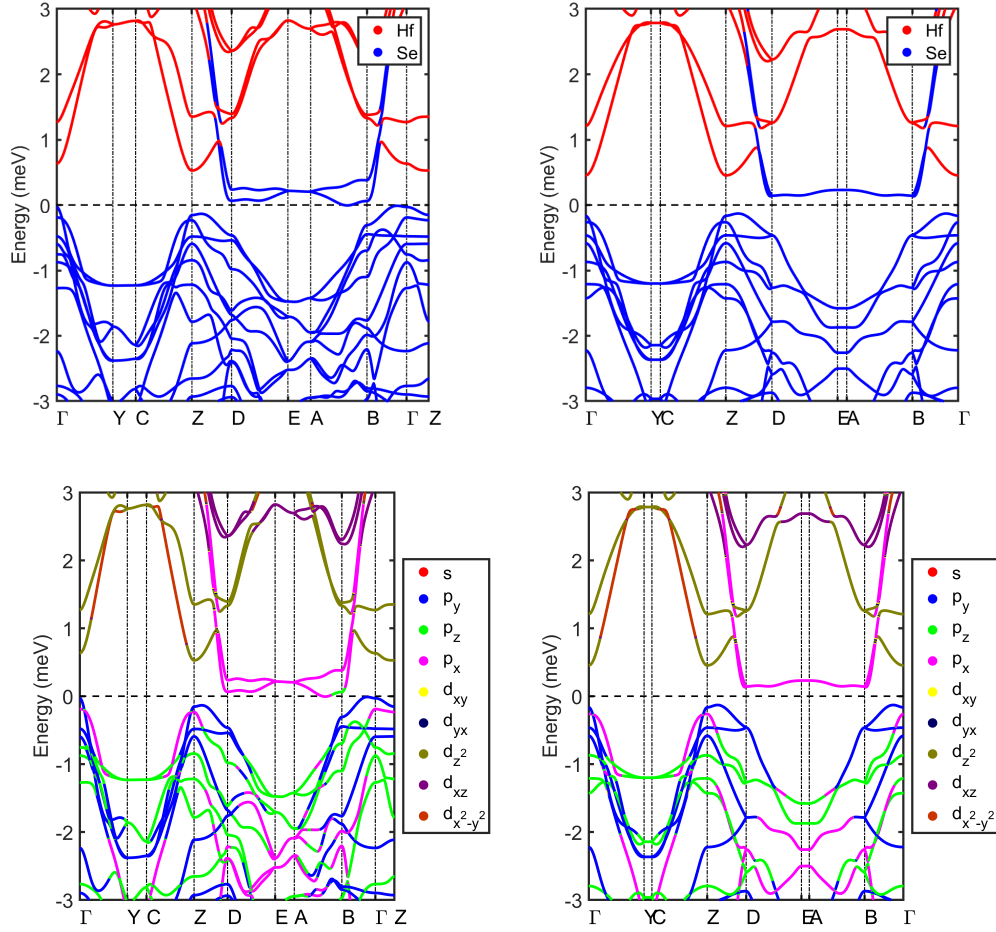
Figure 6.12: Band diagram of (a) bulk HfSe$_3$, and (b) monolayer HfSe$_3$. The color indicates the maximum contribution of either metal or chalcogen atom at each k-point. Band diagram of (c) bulk HfSe$_3$, and (d) monolayer HfSe$_3$, where the color indicates the maximum contribution of atomic orbitals at each k-point.
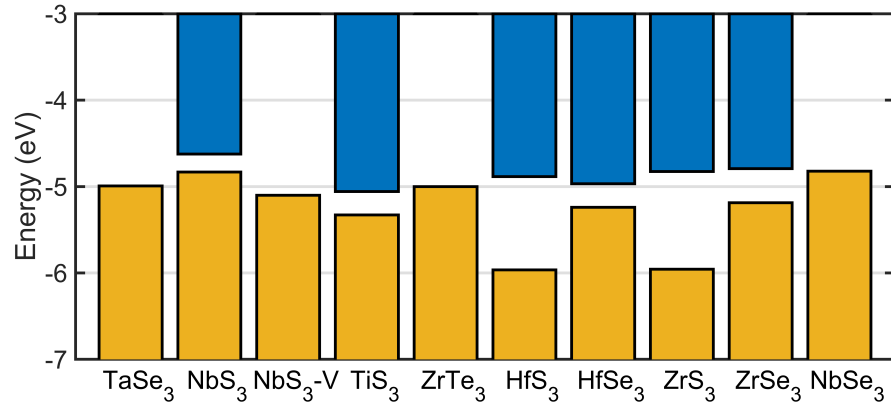
Figure 6.13: Band alignment of monolayer MX$_3$. CBM and VBM with respect to the vacuum level ($E_v = 0\,eV$) are calculated using the density functional theory. The top (bottom) bar indicates the CBM (VBM). In case of the metallic TMTs, only the Fermi level is indicated by the bottom bar.

Bibliography

[1] Mahmud Abdulsalam and Daniel P Joubert. Structural and electronic properties of mx 3 (m= ti, zr and hf; x= s, se, te) from first principles calculations. *The European Physical Journal B*, 88(7):177, 2015.

[2] D. S. L. Abergel, M. Rodriguez-Vega, Enrico Rossi, and S. Das Sarma. Interlayer excitonic superfluidity in graphene. *Phys. Rev. B*, 88:235402, Dec 2013.

[3] A. Abudukelimu, K. Kakushima, P. Ahmet, M. Geni, K. Tsutsui, A. Nishiyama, N. Sugii, K. Natori, T. Hattori, and H. Iwai. The effect of isotropic and anisotropic scattering in drain region of ballistic channel diode. In *2010 10th IEEE International Conference on Solid-State and Integrated Circuit Technology*, pages 1247–1249, Nov 2010.

[4] T. L. Adelman, S. V. Zaitsev-Zotov, and R. E. Thorne. Field-effect modulation of charge-density-wave transport in nbse$_3$ and tas$_3$. *Phys. Rev. Lett.*, 74:5264–5267, Jun 1995.

[5] Philip B. Allen. Improved callaway model for lattice thermal conductivity. *Phys. Rev. B*, 88:144302, Oct 2013.

[6] E. Aytan, B. Debnath, F. Kargar, Y. Barlas, M. M. Lacerda, J. X. Li, R. K. Lake, J. Shi, and A. A. Balandin. Spin-phonon coupling in antiferromagnetic nickel oxide. *Applied Physics Letters*, 111(25):252402, 2017.

[7] Alexander A Balandin. Thermal properties of graphene and nanostructured carbon materials. *Nature materials*, 10(8):569, 2011.

[8] Alexander A. Balandin, Suchismita Ghosh, Wenzhong Bao, Irene Calizo, Desalegne Teweldebrhan, Feng Miao, and Chun Ning Lau. Superior thermal conductivity of single-layer graphene. *Nano Letters*, 8(3):902–907, 2008. PMID: 18284217.

[9] J. Bardeen, L. N. Cooper, and J. R. Schrieffer. Theory of superconductivity. *Phys. Rev.*, 108:1175–1204, Dec 1957.

[10] Einar Bjerkelund and Arne Kjekshus. On the properties of tas3, tase3 and tate4. *Zeitschrift für anorganische und allgemeine Chemie*, 328(5-6):235–242, 1964.

[11] Einar Bjerkelund and Arne Kjekshus. On the crystal structure of tase3. *Acta Chem. Scared*, 19(3):11, 1965.

[12] John Blatt. *Theory of superconductivity*. Academic Press, New York, 1971.

[13] John M. Blatt, K. W. Böer, and Werner Brandt. Bose-einstein condensation of excitons. *Phys. Rev.*, 126:1691–1692, Jun 1962.

[14] P. E. Blöchl. Projector augmented-wave method. *Phys. Rev. B*, 50:17953–17979, Dec 1994.

[15] Matthew A. Bloodgood, Pingrong Wei, Ece Aytan, Krassimir N. Bozhilov, Alexander A. Balandin, and Tina T. Salguero. Monoclinic structures of niobium trisulfide. *APL Materials*, 6(2):026602, 2018.

[16] Nicola Bonini, Jivtesh Garg, and Nicola Marzari. Acoustic phonon lifetimes and thermal transport in free-standing and strained graphene. *Nano letters*, 12(6):2673–2678, 2012.

[17] F.W. Boswell and A. Prodan. Peierls distortions in nbs3 and nbse3. *Physica B+C*, 99(1):361 – 364, 1980.

[18] Liam Britnell, RM Ribeiro, A Eckmann, R Jalil, BD Belle, A Mishchenko, Y-J Kim, RV Gorbachev, T Georgiou, SV Morozov, et al. Strong light-matter interactions in heterostructures of atomically thin films. *Science*, 340(6138):1311–1314, 2013.

[19] D. A. Broido and T. L. Reinecke. Lattice thermal conductivity of superlattice structures. *Phys. Rev. B*, 70:081310, Aug 2004.

[20] D. A. Broido, A. Ward, and N. Mingo. Lattice thermal conductivity of silicon from empirical interatomic potentials. *Phys. Rev. B*, 72:014308, Jul 2005.

[21] DA Broido, Michael Malorny, Gerd Birner, Natalio Mingo, and DA Stewart. Intrinsic lattice thermal conductivity of semiconductors from first principles. *Applied Physics Letters*, 91(23):231922, 2007.

[22] Tomas Bucko, Jurgen Hafner, Sébastien Lebegue, and János G Angyán. Improved description of the structure of molecular and layered crystals: ab initio dft calculations with van der waals corrections. *The Journal of Physical Chemistry A*, 114(43):11814–11824, 2010.

[23] FM Bufler and Wolfgang Fichtner. Scaling of strained-si n-mosfets into the ballistic regime and associated anisotropic effects. *IEEE Transactions on Electron Devices*, 50(2):278–284, 2003.

[24] D W Bullett. Variation of electronic properties with structure of transition metal trichalcogenides. *Journal of Physics C: Solid State Physics*, 12(2):277, 1979.

[25] DW Bullett. Electronic structure and properties of nbs3 and nb3s4. *Journal of Solid State Chemistry*, 33(1):13–16, 1980.

[26] Sheneve Z Butler, Shawna M Hollen, Linyou Cao, Yi Cui, Jay A Gupta, Humberto R Gutiérrez, Tony F Heinz, Seung Sae Hong, Jiaxing Huang, Ariel F Ismach, et al. Progress, challenges, and opportunities in two-dimensional materials beyond graphene. *ACS nano*, 7(4):2898–2926, 2013.

[27] L. V. Butov, A. Zrenner, G. Abstreiter, G. Böhm, and G. Weimann. Condensation of indirect excitons in coupled alas/gaas quantum wells. *Phys. Rev. Lett.*, 73:304–307, Jul 1994.

[28] Joseph Callaway. Model for lattice thermal conductivity at low temperatures. *Phys. Rev.*, 113:1046–1051, Feb 1959.

[29] E. V. Calman, C. J. Dorow, M. M. Fogler, L. V. Butov, S. Hu, A. Mishchenko, and A. K. Geim. Control of excitons in multi-layer van der waals heterostructures. *Applied Physics Letters*, 108(10):101901, 2016.

[30] Jessica Campos-Delgado, Luiz G Cançado, Carlos A Achete, Ado Jorio, and Jean-Pierre Raskin. Raman scattering study of the phonon dispersion in twisted bilayer graphene. *Nano Research*, 6(4):269–274, 2013.

[31] Yuan Cao, Valla Fatemi, Ahmet Demir, Shiang Fang, Spencer L Tomarken, Jason Y Luo, Javier D Sanchez-Yamagishi, Kenji Watanabe, Takashi Taniguchi, Efthimios Kaxiras, et al. Correlated insulator behaviour at half-filling in magic-angle graphene superlattices. *Nature*, 556(7699):80, 2018.

[32] Yuan Cao, Valla Fatemi, Shiang Fang, Kenji Watanabe, Takashi Taniguchi, Efthimios Kaxiras, and Pablo Jarillo-Herrero. Unconventional superconductivity in magic-angle graphene superlattices. *Nature*, 556(7699):43, 2018.

[33] Victor Carozo, Clara M. Almeida, Erlon H. M. Ferreira, Luiz Gustavo Cançado, Carlos Alberto Achete, and Ado Jorio. Raman signature of graphene superlattices. *Nano Letters*, 11(11):4527–4534, 2011. PMID: 21978182.

[34] Yu Chai, Robert Ionescu, Shanshan Su, Roger Lake, Mihrimah Ozkan, and Cengiz S Ozkan. Making one-dimensional electrical contacts to molybdenum disulfide-based heterostructures through plasma etching. *physica status solidi (a)*, 213(5):1358–1364, 2016.

[35] J. P. Cheng, J. Kono, B. D. McCombe, I. Lo, W. C. Mitchel, and C. E. Stutz. Evidence for a stable excitonic ground state in a spatially separated electron-hole system. *Phys. Rev. Lett.*, 74:450–453, Jan 1995.

[36] Manish Chhowalla, Hyeon Suk Shin, Goki Eda, Lain-Jong Li, Kian Ping Loh, and Hua Zhang. The chemistry of two-dimensional layered transition metal dichalcogenide nanosheets. *Nature chemistry*, 5(4):263, 2013.

[37] Alexandr I. Cocemasov, Denis L. Nika, and Alexander A. Balandin. Phonons in twisted bilayer graphene. *Phys. Rev. B*, 88:035428, Jul 2013.

[38] Jonathan N Coleman, Mustafa Lotya, Arlene O´ Neill, Shane D Bergin, Paul J King, Umar Khan, Karen Young, Alexandre Gaucher, Sukanta De, Ronan J Smith, et al. Two-dimensional nanosheets produced by liquid exfoliation of layered materials. *Science*, 331(6017):568–571, 2011.

[39] T Cornelissens, G Van Tendeloo, J Van Landuyt, and S Amelinckx. Peierls distortion, chain polytypism, and dislocation coupling in nbs3. *physica status solidi (a)*, 48(1), 1978.

[40] Jun Dai, Ming Li, and Xiao Cheng Zeng. Group ivb transition metal trichalcogenides: a new class of 2d layered materials beyond graphene. *Wiley Interdisciplinary Reviews: Computational Molecular Science*, 6(2):211–222, 2016.

[41] Jun Dai and Xiao Cheng Zeng. Titanium trisulfide monolayer: Theoretical prediction of a new direct-gap semiconductor with high and anisotropic carrier mobility. *Angewandte Chemie International Edition*, 54(26):7572–7576, 2015.

[42] M Danot, J Afonso, JL Portefaix, M Breysse, and T Des Courières. Catalytic properties of niobium sulphides in the conversion of nitrogen containing molecules. *Catalysis today*, 10(4):629–643, 1991.

[43] Saptarshi Das, Hong-Yan Chen, Ashish Verma Penumatcha, and Joerg Appenzeller. High performance multilayer mos2 transistors with scandium contacts. *Nano letters*, 13(1):100–105, 2012.

[44] S De Palo, F Rapisarda, and Gaetano Senatore. Excitonic condensation in a symmetric electron-hole bilayer. *Physical review letters*, 88(20):206401, 2002.

[45] Bishwajit Debnath, Yafis Barlas, Darshana Wickramaratne, Mahesh R. Neupane, and Roger K. Lake. Exciton condensate in bilayer transition metal dichalcogenides: Strong coupling regime. *Phys. Rev. B*, 96:174504, Nov 2017.

[46] Guangqian Ding, GY Gao, Zhishuo Huang, Wenxu Zhang, and Kailun Yao. Thermoelectric properties of monolayer mse2 (m= zr, hf): low lattice thermal conductivity and a promising figure of merit. *Nanotechnology*, 27(37):375703, 2016.

[47] Eugene Dizhur, Maria Il'Ina, and Sergey Zaitzev-Zotov. Assumed peierls transition in nbs3 under pressure. *physica status solidi (b)*, 246(3):500–503, 2009.

[48] Evgenii Mikhailovich Dizhur, MA Il'ina, and SV Zaĭtsev-Zotov. Metal-insulator transition in whiskers of the nbs3 quasi-one-dimensional conductor under pressure. *JETP Letters*, 86(2):132–134, 2007.

[49] MS Dresselhaus, G Dresselhaus, X Sun, Z Zhang, SB Cronin, and T Koga. Low-dimensional thermoelectric materials. *Physics of the Solid State*, 41(5):679–682, 1999.

[50] Ransell D'Souza and Sugata Mukherjee. Length-dependent lattice thermal conductivity of single-layer and multilayer hexagonal boron nitride: A first-principles study using the callaway-klemens and real-space supercell methods. *Phys. Rev. B*, 96:205422, Nov 2017.

[51] T. Eknapakul, P. D. C. King, M. Asakawa, P. Buaphet, R.-H. He, S.-K. Mo, H. Takagi, K. M. Shen, F. Baumberger, T. Sasagawa, S. Jungthawan, and W. Meevasana. Electronic structure of a quasi-freestanding mos2 monolayer. *Nano Letters*, 14(3):1312–1316, 2014.

[52] K Endo, H Ihara, S Gonda, and K Watanabe. Photoelectron spectroscopic study of nbse3 and tase3. *Physica B+ C*, 105(1-3):159–162, 1981.

[53] Kazuhiro Endo, Hideo Ihara, Kazuhiro Watanabe, and Shun-Ichi Gonda. Xps study on valence band structures of transition-metal trisulfides, tis3, nbs3, and tas3. *Journal of Solid State Chemistry*, 39(2):215 – 218, 1981.

[54] AN Enyashin and AL Ivanovskiĭ. Electronic, energy, and thermal properties of the möbius strip and related ring nanostructures of nbs3. *Physics of the Solid State*, 48(4):780–785, 2006.

[55] A Eucken. On the temperature dependence of the thermal conductivity of several gases. *Phys. Z*, 12:1101–1107, 1911.

[56] VE Fedorov, SB Artemkina, ED Grayfer, Yu V Mironov, AI Romanenko, IV Antonova, and MV Medvedev. Transition metal trichalcogenides as novel layered nano species. In *Proceedings of the International Conference Nanomaterials: Applications and Properties*, number 2, no. 1, pages 01NTF34–01NTF34. Sumy State University Publishing, 2013.

[57] Andrea C Ferrari, Francesco Bonaccorso, Vladimir Fal'Ko, Konstantin S Novoselov, Stephan Roche, Peter Bøggild, Stefano Borini, Frank HL Koppens, Vincenzo Palermo, Nicola Pugno, et al. Science and technology roadmap for graphene, related two-dimensional crystals, and hybrid systems. *Nanoscale*, 7(11):4598–4810, 2015.

[58] IJ Ferrer, JR Ares, JM Clamagirand, M Barawi, and C Sánchez. Optical properties of titanium trisulphide (tis3) thin films. *Thin Solid Films*, 535:398–401, 2013.

[59] E Finkman and B Fisher. Electrical transport measurements in tis3. *Solid state communications*, 50(1):25–28, 1984.

[60] Gianluca Fiori, Francesco Bonaccorso, Giuseppe Iannaccone, Tomás Palacios, Daniel Neumaier, Alan Seabaugh, Sanjay K Banerjee, and Luigi Colombo. Electronics based on two-dimensional materials. *Nature nanotechnology*, 9(10):768, 2014.

[61] Massimo V. Fischetti. Depression of the normal-superfluid transition temperature in gated bilayer graphene. *Journal of Applied Physics*, 115(16):163711, 2014.

[62] B Fisher and M Fibich. Transport properties of tase 3. *Physical Review B*, 37(6):2820, 1988.

[63] M. M. Fogler, L. V. Butov, and K. S. Novoselov. High-temperature superfluidity with indirect excitons in van der waals heterostructures. *Nat. Comm.*, 5:4555, 2014.

[64] T. Fukuzawa, S.S. Kano, T.K. Gustafson, and T. Ogawa. Possibility of coherent light emission from bose condensed states of sehps. *Surface Science*, 228(1):482 – 485, 1990.

[65] T. Fukuzawa, E. E. Mendez, and J. M. Hong. Phase transition of an exciton system in gaas coupled quantum wells. *Phys. Rev. Lett.*, 64:3066–3069, Jun 1990.

[66] SIGRID Furuseth, Leif Brattas, and Arne Kjekshus. Crystal structures of tis 3, zrs 3, zrse 3, zrte 3, hfs 3 and hfse 3. *Acta Chemica Scandinavica*, 29:623, 1975.

[67] Supeng Ge, K. M. Masum Habib, Amrit De, Yafis Barlas, Darshana Wickramaratne, Mahesh R. Neupane, and Roger K. Lake. Interlayer transport through a graphene/rotated boron nitride/graphene heterostructure. *Phys. Rev. B*, 95:045303, Jan 2017.

[68] Andre K Geim and Konstantin S Novoselov. The rise of graphene. In *Nanoscience and Technology: A Collection of Reviews from Nature Journals*, pages 11–19. World Scientific, 2010.

[69] Andre Konstantin Geim. Graphene: status and prospects. *science*, 324(5934):1530–1534, 2009.

[70] Suchismita Ghosh, Wenzhong Bao, Denis L Nika, Samia Subrina, Evghenii P Pokatilov, Chun Ning Lau, and Alexander A Balandin. Dimensional crossover of thermal transport in few-layer graphene. *Nature materials*, 9(7):555, 2010.

[71] Cheng Gong, Luigi Colombo, Robert M Wallace, and Kyeongjae Cho. The unusual mechanism of partial fermi level pinning at metal–mos2 interfaces. *Nano letters*, 14(4):1714–1720, 2014.

[72] Cheng Gong, Hengji Zhang, Weihua Wang, Luigi Colombo, Robert M Wallace, and Kyeongjae Cho. Band alignment of two-dimensional transition metal dichalcogenides: Application in tunnel field effect transistors. *Applied Physics Letters*, 103(5):053513, 2013.

[73] J Gopalakrishnan and KS Nanjundaswamy. Transition metal chalcogenides exhibiting quasi-one-dimensional behaviour. *Bulletin of Materials Science*, 5(3-4):287–306, 1983.

[74] RV Gorbachev, AK Geim, MI Katsnelson, KS Novoselov, T Tudorovskiy, IV Grigorieva, AH MacDonald, SV Morozov, K Watanabe, T Taniguchi, et al. Strong coulomb drag and broken symmetry in double-layer graphene. *Nature Physics*, 8(12):896–901, 2012.

[75] IG Gorlova, V Ya Pokrovskii, SG Zybtsev, AN Titov, and VN Timofeev. Features of the conductivity of the quasi-one-dimensional compound tis 3. *Journal of Experimental and Theoretical Physics*, 111(2):298–303, 2010.

[76] Z.W. Gortel and L. Świerkowski. Superfluid ground state in electron-hole double layer systems. *Surface Science*, 361–362:146 – 149, 1996. Proceedings of the Eleventh International Conference on the Electronic Properties of Two-Dimensional Systems.

[77] Stefan Grimme. Semiempirical gga-type density functional constructed with a long-range dispersion correction. *Journal of computational chemistry*, 27(15):1787–1799, 2006.

[78] Awnish K. Gupta, Youjian Tang, Vincent H. Crespi, and Peter C. Eklund. Nondispersive raman d band activated by well-ordered interlayer interactions in rotationally stacked bilayer graphene. *Phys. Rev. B*, 82:241406, Dec 2010.

[79] P. Haen, F. Lapierre, P. Monceau, M. Núñez Regueiro, and J. Richard. Low temperature phase transition in the chain-like compounds nbse3 and tase3. *Solid State Communications*, 26(11):725 – 730, 1978.

[80] J. Hass, F. Varchon, J. E. Millán-Otoya, M. Sprinkle, N. Sharma, W. A. de Heer, C. Berger, P. N. First, L. Magaud, and E. H. Conrad. Why multilayer graphene on $4h-$SiC($000\bar{1}$) behaves like a single sheet of graphene. *Phys. Rev. Lett.*, 100:125504, Mar 2008.

[81] Robin W. Havener, Houlong Zhuang, Lola Brown, Richard G. Hennig, and Jiwoong Park. Angle-resolved raman imaging of interlayer rotations and interactions in twisted bilayer graphene. *Nano Letters*, 12(6):3162–3167, 2012. PMID: 22612855.

[82] Rui He, Ting-Fung Chung, Conor Delaney, Courtney Keiser, Luis A. Jauregui, Paul M. Shand, C. C. Chancey, Yanan Wang, Jiming Bao, and Yong P. Chen. Observation of low energy raman modes in twisted bilayer graphene. *Nano Letters*, 13(8):3594–3601, 2013. PMID: 23859121.

[83] Jochen Heyd, Gustavo E. Scuseria, and Matthias Ernzerhof. Hybrid functionals based on a screened coulomb potential. *The Journal of Chemical Physics*, 118(18):8207–8215, 2003.

[84] J. Hicks, M. Sprinkle, K. Shepperd, F. Wang, A. Tejeda, A. Taleb-Ibrahimi, F. Bertran, P. Le Fèvre, W. A. de Heer, C. Berger, and E. H. Conrad. Symmetry breaking in commensurate graphene rotational stacking: Comparison of theory and experiment. *Phys. Rev. B*, 83:205403, May 2011.

[85] Yew San Hor, ZL Xiao, Ulrich Welp, Yasuo Ito, JF Mitchell, RE Cook, WK Kwok, and George W Crabtree. Nanowires and nanoribbons of charge-density-wave conductor nbse3. *Nano letters*, 5(2):397–401, 2005.

[86] Hui Hu, X-J Liu, and Peter D Drummond. Equation of state of a superfluid fermi gas in the bcs-bec crossover. *EPL (Europhysics Letters)*, 74(4):574, 2006.

[87] Hesameddin Ilatikhameneh, Yaohua Tan, Bozidar Novakovic, Gerhard Klimeck, Rajib Rahman, and Joerg Appenzeller. Tunnel field-effect transistors in 2-d transition metal dichalcogenide materials. *IEEE Journal on Exploratory Solid-State Computational Devices and Circuits*, 1:12–18, 2015.

[88] Joshua O Island, Robert Biele, Mariam Barawi, José M Clamagirand, José R Ares, Carlos Sánchez, Herre SJ Van Der Zant, Isabel J Ferrer, Roberto D'Agosta, and Andres Castellanos-Gomez. Titanium trisulfide (tis 3): a 2d semiconductor with quasi-1d optical and electronic properties. *Scientific reports*, 6:22214, 2016.

[89] Joshua O Island, Aday J Molina-Mendoza, Mariam Barawi, Robert Biele, Eduardo Flores, José M Clamagirand, José R Ares, Carlos Sánchez, Herre SJ van der Zant, Roberto D'Agosta, et al. Electronics and optoelectronics of quasi-1d layered transition metal trichalcogenides. *2D Materials*, 4(2):022003, 2017.

[90] Toshiaki Iwazumi, Mitsuru Izumi, Kunimitsu Uchinokura, Ryozo Yoshizaki, and Etsuyuki Matsuura. Stacking disorder in nbs3 and zrx3 (x= s, se). *Physica B+ C*, 143(1-3):255–257, 1986.

[91] Mitsuru Izumi, Toshiki Nakayama, Kunimitsu Uchinokura, Ryozo Yoshizaki, and Etsuyuki Matsuura. Superconducting properties in metallic phase of nbs3. *Molecular Crystals and Liquid Crystals*, 121(1-4):79–82, 1985.

[92] F Jellinek, Go Brauer, and H Müller. Molybdenum and niobium sulphides. *Nature*, 185(4710):376, 1960.

[93] D. Jérome, T. M. Rice, and W. Kohn. Excitonic insulator. *Phys. Rev.*, 158:462–475, Jun 1967.

[94] Jin-Wu Jiang, Hui Tang, Bing-Shen Wang, and Zhao-Bin Su. Raman and infrared properties and layer dependence of the phonon dispersions in multilayered graphene. *Phys. Rev. B*, 77:235421, Jun 2008.

[95] Yingdi Jin, Xingxing Li, and Jinlong Yang. Single layer of mx3 (m = ti, zr; x = s, se, te): a new platform for nano-electronics and optics. *Phys. Chem. Chem. Phys.*, 17:18665–18669, 2015.

[96] F Kadijk and F Jellinek. The system niobium-sulfur. *Journal of the Less Common Metals*, 19(4):421–430, 1969.

[97] Seiichi Kagoshima, Hiroshi Nagasawa, and Takashi Sambongi. What are one-dimensional conductors? In *One-Dimensional Conductors*, pages 1–3. Springer, 1988.

[98] Jiahao Kang, Wei Liu, and Kaustav Banerjee. High-performance mos2 transistors with low-resistance molybdenum contacts. *Applied Physics Letters*, 104(9):093106, 2014.

[99] Fariborz Kargar, Zahra Barani, Ruben Salgado, Bishwajit Debnath, Jacob S. Lewis, Ece Aytan, Roger K. Lake, and Alexander A. Balandin. Thermal percolation threshold and thermal properties of composites with high loading of graphene and boron nitride fillers. *ACS Applied Materials & Interfaces*, 0(0):null, 0. PMID: 30299919.

[100] Fariborz Kargar, Sylvester Ramirez, Bishwajit Debnath, Hoda Malekpour, Roger K. Lake, and Alexander A. Balandin. Acoustic phonon spectrum and thermal transport in nanoporous alumina arrays. *Applied Physics Letters*, 107(17):171904, 2015.

[101] J. A. Kash, M. Zachau, E. E. Mendez, J. M. Hong, and T. Fukuzawa. Fermi-dirac distribution of excitons in coupled quantum wells. *Phys. Rev. Lett.*, 66:2247–2250, Apr 1991.

[102] M. Kellogg, J. P. Eisenstein, L. N. Pfeiffer, and K. W. West. Vanishing hall resistance at high magnetic field in a double-layer two-dimensional electron system. *Phys. Rev. Lett.*, 93:036801, Jul 2004.

[103] Maxim Yu. Kharitonov and Konstantin B. Efetov. Electron screening and excitonic condensation in double-layer graphene systems. *Phys. Rev. B*, 78:241401, Dec 2008.

[104] GF Khudorozhko, IP Asanov, AV Mischenko, LN Mazalov, SB Erenburg, VE Fedorov, and AI Romanenko. An x-ray photoelectron and x-ray emission study of the electronic structure of nb trichalcogenides and their lithium intercalates. *Journal of Solid State Chemistry*, 74(1):16–20, 1988.

[105] S Kikkawa, M Koizumi, S Yamanaka, Y Onuki, and S Tanuma. Electrical conductivity of tis3. *physica status solidi (a)*, 61(1):K55–K57, 1980.

[106] S Kikkawa, N Ogawa, M Koizumi, and Y Onuki. High-pressure syntheses of tas3, nbs3, tase3, and nbse3 with nbse3-type crystal structure. *Journal of Solid State Chemistry*, 41(3):315–322, 1982.

[107] Kwanpyo Kim, Sinisa Coh, Liang Z. Tan, William Regan, Jong Min Yuk, Eric Chatterjee, M. F. Crommie, Marvin L. Cohen, Steven G. Louie, and A. Zettl. Raman spectroscopy study of rotated double-layer graphene: Misorientation-angle dependence of electronic structure. *Phys. Rev. Lett.*, 108:246103, Jun 2012.

[108] PG Klemens. The thermal conductivity of dielectric solids at low temperatures (theoretical). In *Proceedings of the Royal Society of London A: Mathematical, Physical and Engineering Sciences*, volume 208, pages 108–133. The Royal Society, 1951.

[109] B. D. Kong, S. Paul, M. Buongiorno Nardelli, and K. W. Kim. First-principles analysis of lattice thermal conductivity in monolayer and bilayer graphene. *Phys. Rev. B*, 80:033406, Jul 2009.

[110] Wilson Kong, Cihan Bacaksiz, Bin Chen, Kedi Wu, Mark Blei, Xi Fan, Yuxia Shen, Hasan Sahin, David Wright, Deepa S Narang, et al. Angle resolved vibrational properties of anisotropic transition metal trichalcogenide nanosheets. *Nanoscale*, 9(12):4175–4182, 2017.

[111] FHL Koppens, T Mueller, Ph Avouris, AC Ferrari, MS Vitiello, and M Polini. Photodetectors based on graphene, other two-dimensional materials and hybrid systems. *Nature nanotechnology*, 9(10):780, 2014.

[112] Andor Kormányos, Guido Burkard, Martin Gmitra, Jaroslav Fabian, Viktor Zólyomi, Neil D Drummond, and Vladimir Fal'ko. k·p theory for two-dimensional transition metal dichalcogenide semiconductors. *2D Materials*, 2(2):022001, 2015.

[113] J M Kosterlitz and D J Thouless. Ordering, metastability and phase transitions in two-dimensional systems. *Journal of Physics C: Solid State Physics*, 6(7):1181, 1973.

[114] G. Kresse and J. Furthmüller. Efficiency of ab-initio total energy calculations for metals and semiconductors using a plane-wave basis set. *Computational Materials Science*, 6(1):15 – 50, 1996.

[115] G. Kresse and J. Hafner. Ab initio. *Phys. Rev. B*, 48:13115–13118, Nov 1993.

[116] Georg Kresse and Jürgen Furthmüller. Efficiency of ab-initio total energy calculations for metals and semiconductors using a plane-wave basis set. *Computational materials science*, 6(1):15–50, 1996.

[117] Georg Kresse and J Hafner. Ab initio molecular dynamics for open-shell transition metals. *Physical Review B*, 48(17):13115, 1993.

[118] YD Kuang, Lucas Lindsay, SQ Shi, and GP Zheng. Tensile strains give rise to strong size effects for thermal conductivities of silicene, germanene and stanene. *Nanoscale*, 8(6):3760–3767, 2016.

[119] Youdi Kuang, Lucas Lindsay, Sanqiang Shi, Xinjiang Wang, and Baoling Huang. Thermal conductivity of graphene mediated by strain and size. *International Journal of Heat and Mass Transfer*, 101:772–778, 2016.

[120] Mohamad Kurdi, Anne-Marie Marie, and Michel Danot. The crystallographic mechanism of the nbs3 to nb1. 12s2 transition. *Solid state communications*, 64(4):395–399, 1987.

[121] Sylvain Latil, Vincent Meunier, and Luc Henrard. Massless fermions in multilayer graphitic systems with misoriented layers: Ab initio calculations and experimental fingerprints. *Phys. Rev. B*, 76:201402, Nov 2007.

[122] Chenyang Li, Bishwajit Debnath, Xiaojian Tan, Shanshan Su, Kui Xu, Supeng Ge, Mahesh R. Neupane, and Roger K. Lake. Commensurate lattice constant dependent thermal conductivity of misoriented bilayer graphene. *Carbon*, 138:451 – 457, 2018.

[123] Hongyang Li, Hao Ying, Xiangping Chen, Denis L. Nika, Alexandr I. Cocemasov, Weiwei Cai, Alexander A. Balandin, and Shanshan Chen. Thermal conductivity of twisted bilayer graphene. *Nanoscale*, 6:13402–13408, 2014.

[124] Mingda Li, David Esseni, Gregory Snider, Debdeep Jena, and Huili Grace Xing. Single particle transport in two-dimensional heterojunction interlayer tunneling field effect transistor. *Journal of Applied Physics*, 115(7):074508, 2014.

[125] Mingda Oscar Li, David Esseni, Joseph J Nahas, Debdeep Jena, and Huili Grace Xing. Two-dimensional heterojunction interlayer tunneling field effect transistors (thin-tfets). *IEEE Journal of the Electron Devices Society*, 3(3):200–207, 2015.

[126] Wu Li, Jesús Carrete, Nebil A. Katcho, and Natalio Mingo. Shengbte: A solver of the boltzmann transport equation for phonons. *Computer Physics Communications*, 185(6):1747 – 1758, 2014.

[127] Wu Li, L. Lindsay, D. A. Broido, Derek A. Stewart, and Natalio Mingo. Thermal conductivity of bulk and nanowire $mg_2si_xsn_{1-x}$ alloys from first principles. *Phys. Rev. B*, 86:174307, Nov 2012.

[128] Wu Li and Natalio Mingo. Lattice dynamics and thermal conductivity of skutterudites $cosb_3$ and $irsb_3$ from first principles: Why $irsb_3$ is a better thermal conductor than $cosb_3$. *Phys. Rev. B*, 90:094302, Sep 2014.

[129] Wu Li and Natalio Mingo. Ultralow lattice thermal conductivity of the fully filled skutterudite ybfe 4 sb 12 due to the flat avoided-crossing filler modes. *Physical Review B*, 91(14):144304, 2015.

[130] Wu Li, Natalio Mingo, L. Lindsay, D. A. Broido, D. A. Stewart, and N. A. Katcho. Thermal conductivity of diamond nanowires from first principles. *Phys. Rev. B*, 85:195436, May 2012.

[131] Tej B Limbu, Konstanze R Hahn, Frank Mendoza, Satyaprakash Sahoo, Joshua James Razink, Ram S Katiyar, Brad R Weiner, and Gerardo Morell. Grain size-dependent thermal conductivity of polycrystalline twisted bilayer graphene. *Carbon*, 117:367–375, 2017.

[132] L. Lindsay, D. A. Broido, and Natalio Mingo. Diameter dependence of carbon nanotube thermal conductivity and extension to the graphene limit. *Phys. Rev. B*, 82:161402, Oct 2010.

[133] L. Lindsay, Wu Li, Jesús Carrete, Natalio Mingo, D. A. Broido, and T. L. Reinecke. Phonon thermal transport in strained and unstrained graphene from first principles. *Phys. Rev. B*, 89:155426, Apr 2014.

[134] Guanxiong Liu, Bishwajit Debnath, Timothy R Pope, Tina T Salguero, Roger K Lake, and Alexander A Balandin. A charge-density-wave oscillator based on an integrated tantalum disulfide–boron nitride–graphene device operating at room temperature. *Nature nanotechnology*, 11(10):845, 2016.

[135] Guanxiong Liu, Sergey Rumyantsev, Matthew A. Bloodgood, Tina T. Salguero, Michael Shur, and Alexander A. Balandin. Low-frequency electronic noise in quasi-1d tase3 van der waals nanowires. *Nano Letters*, 17(1):377–383, 2017. PMID: 28073263.

[136] J. M. B. Lopes dos Santos, N. M. R. Peres, and A. H. Castro Neto. Graphene bilayer with a twist: Electronic structure. *Phys. Rev. Lett.*, 99:256802, Dec 2007.

[137] E. Y. Lozovik and A. A. Sokolik. Ultrarelativistic electron-hole pairing in graphene bilayer. *The European Physical Journal B*, 73(2):195–206, 2010.

[138] Yu. E. Lozovik, I. L. Kurbakov, and Pavel A. Volkov. Anisotropic superfluidity of two-dimensional excitons in a periodic potential. *Phys. Rev. B*, 95:245430, Jun 2017.

[139] Yu. E. Lozovik, S. L. Ogarkov, and A. A. Sokolik. Electron–electron and electron–hole pairing in graphene structures. *Philosophical Transactions of the Royal Society of London A: Mathematical, Physical and Engineering Sciences*, 368(1932):5417–5429, 2010.

[140] Yu. E. Lozovik, S. L. Ogarkov, and A. A. Sokolik. Condensation of electron-hole pairs in a two-layer graphene system: Correlation effects. *Phys. Rev. B*, 86:045429, Jul 2012.

[141] Yu. E. Lozovik and A. A. Sokolik. Electron-hole pair condensation in a graphene bilayer. *JETP Letters*, 87(1):55–59, 2008.

[142] Yu E Lozovik and VI Yudson. A new mechanism for superconductivity: pairing between spatially separated electrons and holes. *Zh. Eksp. Teor. Fiz*, 71:738–753, 1976.

[143] Yu.E. Lozovik and A.A. Sokolik. Multi-band pairing of ultrarelativistic electrons and holes in graphene bilayer. *Physics Letters A*, 374(2):326 – 330, 2009.

[144] Chun-Chieh Lu, Yung-Chang Lin, Zheng Liu, Chao-Hui Yeh, Kazu Suenaga, and Po-Wen Chiu. Twisting bilayer graphene superlattices. *ACS Nano*, 7(3):2587–2594, 2013. PMID: 23448165.

[145] Chun Hung Lui, Leandro M. Malard, SukHyun Kim, Gabriel Lantz, François E. Laverge, Riichiro Saito, and Tony F. Heinz. Observation of layer-breathing mode vibrations in few-layer graphene through combination raman scattering. *Nano Letters*, 12(11):5539–5544, 11 2012.

[146] A. Luican, Guohong Li, A. Reina, J. Kong, R. R. Nair, K. S. Novoselov, A. K. Geim, and E. Y. Andrei. Single-layer behavior and its breakdown in twisted graphene layers. *Phys. Rev. Lett.*, 106:126802, Mar 2011.

[147] F. Lévy and H. Berger. Single crystals of transition metal trichalcogenides. *Journal of Crystal Growth*, 61(1):61 – 68, 1983.

[148] Jinlong Ma, Wu Li, and Xiaobing Luo. Examining the callaway model for lattice thermal conductivity. *Physical Review B*, 90(3):035203, 2014.

[149] Allan H MacDonald and Rafi Bistritzer. Materials science: Graphene moiré mystery solved? *Nature*, 474(7352):453, 2011.

[150] Gerald D Mahan. *Many-particle physics*. Springer Science & Business Media, 2013.

[151] Kin Fai Mak, Keliang He, Jie Shan, and Tony F Heinz. Control of valley polarization in monolayer mos2 by optical helicity. *Nature nanotechnology*, 7(8):494–498, 2012.

[152] Kin Fai Mak, Changgu Lee, James Hone, Jie Shan, and Tony F. Heinz. Atomically thin mos$_2$: A new direct-gap semiconductor. *Phys. Rev. Lett.*, 105:136805, Sep 2010.

[153] Kin Fai Mak and Jie Shan. Photonics and optoelectronics of 2d semiconductor transition metal dichalcogenides. *Nature Photonics*, 10(4):216, 2016.

[154] E. J. Mele. Commensuration and interlayer coherence in twisted bilayer graphene. *Phys. Rev. B*, 81:161405, Apr 2010.

[155] Hongki Min, Rafi Bistritzer, Jung-Jung Su, and A. H. MacDonald. Room-temperature superfluidity in graphene bilayers. *Phys. Rev. B*, 78:121401, Sep 2008.

[156] M. P. Mink, H. T. C. Stoof, R. A. Duine, and A. H. MacDonald. Influence of remote bands on exciton condensation in double-layer graphene. *Phys. Rev. B*, 84:155409, Oct 2011.

[157] Shoichi Nagata, Shuji Ebisu, Tsuyoshi Aochi, Yasuhiro Kinoshita, Susumu Chikazawa, and Kazuhiko Yamaya. Superconductivity in the filamentary conductor tase3. *Journal of Physics and Chemistry of Solids*, 52(6):761–767, 1991.

[158] Shoichi Nagata, Hiroki Kutsuzawa, Shuji Ebisu, Hidemi Yamamura, and Satoshi Taniguchi. Superconductivity in the quasi-one-dimensional conductor tase3. *Journal of Physics and Chemistry of Solids*, 50(7):703–707, 1989.

[159] Yoichiro Nambu. Quasi-particles and gauge invariance in the theory of superconductivity. *Phys. Rev.*, 117:648–663, Feb 1960.

[160] D. Neilson, A. Perali, and A. R. Hamilton. Excitonic superfluidity and screening in electron-hole bilayer systems. *Phys. Rev. B*, 89:060502, Feb 2014.

[161] AH Castro Neto, Francisco Guinea, Nuno MR Peres, Kostya S Novoselov, and Andre K Geim. The electronic properties of graphene. *Reviews of modern physics*, 81(1):109, 2009.

[162] Zhenhua Ni, Lei Liu, Yingying Wang, Zhe Zheng, Lain-Jong Li, Ting Yu, and Zexiang Shen. *g*-band raman double resonance in twisted bilayer graphene: Evidence of band splitting and folding. *Phys. Rev. B*, 80:125404, Sep 2009.

[163] Takeshi Nihira and Tadao Iwata. Temperature dependence of lattice vibrations and analysis of the specific heat of graphite. *Phys. Rev. B*, 68:134305, Oct 2003.

[164] Ahti Niilisk, Jekaterina Kozlova, Harry Alles, Jaan Aarik, and Väino Sammelselg. Raman characterization of stacking in multi-layer graphene grown on ni. *Carbon*, 98:658 – 665, 2016.

[165] Denis L. Nika, Alexandr I. Cocemasov, and Alexander A. Balandin. Specific heat of twisted bilayer graphene: Engineering phonons by atomic plane rotations. *Applied Physics Letters*, 105(3):031904, 2014.

[166] Kostya S Novoselov, Andre K Geim, Sergei V Morozov, D Jiang, Y. Zhang, Sergey V Dubonos, Irina V Grigorieva, and Alexandr A Firsov. Electric field effect in atomically thin carbon films. *science*, 306(5696):666–669, 2004.

[167] KS Novoselov, A Mishchenko, A Carvalho, and AH Castro Neto. 2d materials and van der waals heterostructures. *Science*, 353(6298):aac9439, 2016.

[168] M Omini and A Sparavigna. Heat transport in dielectric solids with diamond structure. *NUOVO CIMENTO-SOCIETA ITALIANA DI FISICA SEZIONE D*, 19:1537–1564, 1997.

[169] Kazuki Osada, Soungmin Bae, Masatoshi Tanaka, Hannes Raebiger, Kenichi Shudo, and Takanori Suzuki. Phonon properties of few-layer crystals of quasi-one-dimensional zrs3 and zrse3. *The Journal of Physical Chemistry C*, 120(8):4653–4659, 2016.

[170] V Ongun Özçelik, Javad G Azadani, Ce Yang, Steven J Koester, and Tony Low. Band alignment of two-dimensional semiconductors for designing heterostructures with momentum space matching. *Physical Review B*, 94(3):035125, 2016.

[171] D Pacilé, M Papagno, M Lavagnini, H Berger, L Degiorgi, and M Grioni. Photoemission and optical studies of zr se 3, hf se 3, and zr s 3. *Physical Review B*, 76(15):155406, 2007.

[172] Anupum Pant, Engin Torun, Bin Chen, Soumya Bhat, Xi Fan, Kedi Wu, David P Wright, Francois M Peeters, Emmanuel Soignard, Hasan Sahin, et al. Strong dichroic emission in the pseudo one dimensional material zrs 3. *Nanoscale*, 8(36):16259–16265, 2016.

[173] Hiral Patel, Robin W Havener, Lola Brown, Yufeng Liang, Li Yang, Jiwoong Park, and Matt W Graham. Tunable optical excitations in twisted bilayer graphene form strongly bound excitons. *Nano letters*, 15(9):5932–5937, 2015.

[174] A. Perali, D. Neilson, and A. R. Hamilton. High-temperature superfluidity in double-bilayer graphene. *Phys. Rev. Lett.*, 110:146803, Apr 2013.

[175] John P. Perdew, Kieron Burke, and Matthias Ernzerhof. Generalized gradient approximation made simple. *Phys. Rev. Lett.*, 77:3865–3868, Oct 1996.

[176] V. Perebeinos, J. Tersoff, and Ph. Avouris. Phonon-mediated interlayer conductance in twisted graphene bilayers. *Phys. Rev. Lett.*, 109:236604, Dec 2012.

[177] V Podzorov, ME Gershenson, Ch Kloc, R Zeis, and E Bucher. High-mobility field-effect transistors based on transition metal dichalcogenides. *Applied Physics Letters*, 84(17):3301–3303, 2004.

[178] Marco Polini, Reza Asgari, Yafis Barlas, T. Pereg-Barnea, and A.H. MacDonald. Graphene: A pseudochiral fermi liquid. *Solid State Communications*, 143(1-2):58 – 62, 2007. Exploring grapheneRecent research advances.

[179] P. Poncharal, A. Ayari, T. Michel, and J.-L. Sauvajol. Raman spectra of misoriented bilayer graphene. *Phys. Rev. B*, 78:113407, Sep 2008.

[180] A Prodan, A Budkowski, FW Boswell, V Marinkov, JC Bennett, and JM Corbett. An approach to the structure of incommensurately modulated nbs3 type ii. *Journal of Physics C: Solid State Physics*, 21(23):4171, 1988.

[181] Branimir Radisavljevic, Aleksandra Radenovic, Jacopo Brivio, i V Giacometti, and A Kis. Single-layer mos 2 transistors. *Nature nanotechnology*, 6(3):147, 2011.

[182] Ashwin Ramasubramaniam, Doron Naveh, and Elias Towe. Tunable band gaps in bilayer transition-metal dichalcogenides. *Physical Review B*, 84(20):205325, 2011.

[183] Pankaj Ramnani, Mahesh R. Neupane, Supeng Ge, Alexander A. Balandin, Roger K. Lake, and Ashok Mulchandani. Raman spectra of twisted cvd bilayer graphene. *Carbon*, 123:302 – 306, 2017.

[184] MH Rashid and DJ Sellmyer. Electrical conduction in quasi-one-dimensional compounds: $TaSe_3$, nb_2se_3, and nb_3s_4. *Physical Review B*, 29(4):2359, 1984.

[185] BV Ratnakumar, CL Ni, S Di Stefano, G Nagasubramanian, and CP Bankston. Electrochemical studies on niobium triselenide cathode material for lithium rechargeable cells. *Journal of The Electrochemical Society*, 136(1):6–12, 1989.

[186] Jackie D Renteria, Denis L Nika, and Alexander A Balandin. Graphene thermal properties: applications in thermal management and energy storage. *Applied Sciences*, 4(4):525–547, 2014.

[187] A. Righi, S. D. Costa, H. Chacham, C. Fantini, P. Venezuela, C. Magnuson, L. Colombo, W. S. Bacsa, R. S. Ruoff, and M. A. Pimenta. Graphene moiré patterns observed by umklapp double-resonance raman scattering. *Phys. Rev. B*, 84:241409, Dec 2011.

[188] J. Rijnsdorp and F. Jellinek. The crystal structure of niobium trisulfide, nbs3. *Journal of Solid State Chemistry*, 25(4):325 – 328, 1978.

[189] Alex W. Robertson and Jamie H. Warner. Hexagonal single crystal domains of few-layer graphene on copper foils. *Nano Letters*, 11(3):1182–1189, 2011.

[190] Tania Roy, Mahmut Tosun, Xi Cao, Hui Fang, Der-Hsien Lien, Peida Zhao, Yu-Ze Chen, Yu-Lun Chueh, Jing Guo, and Ali Javey. Dual-gated mos2/wse2 van der waals tunnel diodes and transistors. *Acs Nano*, 9(2):2071–2079, 2015.

[191] Atsushi Sakuda, Noboru Taguchi, Tomonari Takeuchi, Hironori Kobayashi, Hikari Sakaebe, Kuniaki Tatsumi, and Zempachi Ogumi. Amorphous niobium sulfides as novel positive-electrode materials. *ECS Electrochemistry Letters*, 3(7):A79–A81, 2014.

[192] Takashi Sambongi, Masafumi Yamamoto, Kitomi Tsutsumi, Yoichi Shiozaki, Kazuhiko Yamaya, and Yutaka Abe. Superconductivity in one-dimensional tase3. *Journal of the Physical Society of Japan*, 42(4):1421–1422, 1977.

[193] Kentaro Sato, Riichiro Saito, Chunxiao Cong, Ting Yu, and Mildred S. Dresselhaus. Zone folding effect in raman g-band intensity of twisted bilayer graphene. *Phys. Rev. B*, 86:125414, Sep 2012.

[194] Khan M. F. Shahil and Alexander A. Balandin. Graphene–multilayer graphene nanocomposites as highly efficient thermal interface materials. *Nano Letters*, 12(2):861–867, 2012. PMID: 22214526.

[195] Khan M.F. Shahil and Alexander A. Balandin. Thermal properties of graphene and multilayer graphene: Applications in thermal interface materials. *Solid State Communications*, 152(15):1331 – 1340, 2012. Exploring Graphene, Recent Research Advances.

[196] S. Shallcross, S. Sharma, E. Kandelaki, and O. A. Pankratov. Electronic structure of turbostratic graphene. *Phys. Rev. B*, 81:165105, Apr 2010.

[197] S. Shallcross, S. Sharma, and O. A. Pankratov. Quantum interference at the twist boundary in graphene. *Phys. Rev. Lett.*, 101:056803, Aug 2008.

[198] Nobuyuki Shima. Band structure of nbse3. *Journal of the Physical Society of Japan*, 52(2):578–586, 1983.

[199] CG Slough, B Giambattista, WW McNairy, and RV Coleman. Scanning tunneling microscopy of the linear chain compounds nbse3, tas3, and tase3. *Journal of Vacuum Science & Technology A: Vacuum, Surfaces, and Films*, 8(1):490–494, 1990.

[200] Inti Sodemann, D. A. Pesin, and A. H. MacDonald. Interaction-enhanced coherence between two-dimensional dirac layers. *Phys. Rev. B*, 85:195136, May 2012.

[201] C Sourisseau, R Cavagnat, M Fouassier, and P Maraval. Electronic, vibrational and resonance raman spectra of the layered semiconducting compound nbs3. *Journal of Raman Spectroscopy*, 21(6):337–349, 1990.

[202] I. B. Spielman, J. P. Eisenstein, L. N. Pfeiffer, and K. W. West. Resonantly enhanced tunneling in a double layer quantum hall ferromagnet. *Phys. Rev. Lett.*, 84:5808–5811, Jun 2000.

[203] Ralf Steudel. Properties of sulfur-sulfur bonds. *Angewandte Chemie International Edition in English*, 14(10):655–664, 1975.

[204] Jung-Jung Su and Allan H. MacDonald. Spatially indirect exciton condensate phases in double bilayer graphene. *Phys. Rev. B*, 95:045416, Jan 2017.

[205] PH Tan, WP Han, WJ Zhao, ZH Wu, K Chang, H Wang, YF Wang, N Bonini, N Marzari, N Pugno, et al. The shear mode of multilayer graphene. *Nature materials*, 11(4):294, 2012.

[206] Atsushi Togo, Fumiyasu Oba, and Isao Tanaka. First-principles calculations of the ferroelastic transition between rutile-type and cacl$_2$-type sio$_2$ at high pressures. *Phys. Rev. B*, 78:134106, Oct 2008.

[207] Atsushi Togo and Isao Tanaka. First principles phonon calculations in materials science. *Scripta Materialia*, 108:1 – 5, 2015.

[208] J. Towns, T. Cockerill, M. Dahan, I. Foster, K. Gaither, A. Grimshaw, V. Hazlewood, S. Lathrop, D. Lifka, G. D. Peterson, R. Roskies, J. R. Scott, and N. Wilkins-Diehr. Xsede: Accelerating scientific discovery. *Computing in Science Engineering*, 16(5):62–74, Sept 2014.

[209] E. Tutuc, M. Shayegan, and D. A. Huse. Counterflow measurements in strongly correlated gaas hole bilayers: Evidence for electron-hole pairing. *Phys. Rev. Lett.*, 93:036802, Jul 2004.

[210] Pedro Venezuela, Michele Lazzeri, and Francesco Mauri. Theory of double-resonant raman spectra in graphene: Intensity and line shape of defect-induced and two-phonon bands. *Phys. Rev. B*, 84:035433, Jul 2011.

[211] Giovanni Vignale and A. H. MacDonald. Drag in paired electron-hole layers. *Phys. Rev. Lett.*, 76:2786–2789, Apr 1996.

[212] Fancy Qian Wang, Jiabing Yu, Qian Wang, Yoshiyuki Kawazoe, and Puru Jena. Lattice thermal conductivity of penta-graphene. *Carbon*, 105:424 – 429, 2016.

[213] Gang Wang, Cedric Robert, Aslihan Suslu, Bin Chen, Sijie Yang, Sarah Alamdari, Iann C Gerber, Thierry Amand, Xavier Marie, Sefaattin Tongay, et al. Spin-orbit engineering in transition metal dichalcogenide alloy monolayers. *Nature communications*, 6, 2015.

[214] Qing Hua Wang, Kourosh Kalantar-Zadeh, Andras Kis, Jonathan N Coleman, and Michael S Strano. Electronics and optoelectronics of two-dimensional transition metal dichalcogenides. *Nature nanotechnology*, 7(11):699, 2012.

[215] Yanan Wang, Zhihua Su, Wei Wu, Shu Nie, Nan Xie, Huiqi Gong, Yang Guo, Joon Hwan Lee, Sirui Xing, Xiaoxiang Lu, Haiyan Wang, Xinghua Lu, Kevin McCarty, Shin-shem Pei, Francisco Robles-Hernandez, Viktor G. Hadjiev, and Jiming Bao. Resonance raman spectroscopy of g-line and folded phonons in twisted bilayer graphene with large rotation angles. *Applied Physics Letters*, 103(12):123101, 2013.

[216] ZZ Wang, P Monceau, H Salva, C Roucau, L Guemas, and A Meerschaut. Charge-density-wave transport above room temperature in a polytype of nbs 3. *Physical Review B*, 40(17):11589, 1989.

[217] A. Ward and D. A. Broido. Intrinsic phonon relaxation times from first-principles studies of the thermal conductivities of si and ge. *Phys. Rev. B*, 81:085205, Feb 2010.

[218] A. Ward, D. A. Broido, Derek A. Stewart, and G. Deinzer. Ab initio theory of the lattice thermal conductivity in diamond. *Phys. Rev. B*, 80:125203, Sep 2009.

[219] M Stanley Whittingham and Gerald H Newman. Niobium triselenide in a lithium dioxolane cell. *Journal of The Electrochemical Society*, 128(3):706–707, 1981.

[220] Darshana Wickramaratne. *Electronic, Vibrational and Thermoelectric Properties of Two-Dimensional Materials*. PhD thesis, University of California Riverside, 2015.

[221] TJ Wieting, A Grisel, and F Levy. Raman scattering by optical phonons in tase3 and nbse3. *Molecular Crystals and Liquid Crystals*, 81(1):117–124, 1982.

[222] JA Wilson. Bands, bonds, and charge-density waves in the nb se 3 family of compounds. *Physical Review B*, 19(12):6456, 1979.

[223] Dillon Wong, Yang Wang, Jeil Jung, Sergio Pezzini, Ashley M DaSilva, Hsin-Zon Tsai, Han Sae Jung, Ramin Khajeh, Youngkyou Kim, Juwon Lee, et al. Local spectroscopy of moire-induced electronic structure in gate-tunable twisted bilayer graphene. *Physical Review B*, 92(15):155409, 2015.

[224] Feng-Cheng Wu, Fei Xue, and A. H. MacDonald. Theory of two-dimensional spatially indirect equilibrium exciton condensates. *Phys. Rev. B*, 92:165121, Oct 2015.

[225] Jian Wu, Da Wang, Hao Liu, Woon-Ming Lau, and Li-Min Liu. An ab initio study of tis3: a promising electrode material for rechargeable li and na ion batteries. *RSC Advances*, 5(28):21455–21463, 2015.

[226] Xian Wu, X. Mou, L. F. Register, and S. K. Banerjee. Theoretical study of the spontaneous electron-hole exciton condensates between n and p-type mos2 monolayers, toward beyond cmos applications. In *2015 International Conference on Simulation of Semiconductor Processes and Devices (SISPAD)*, pages 124–127. IEEE, Sept 2015.

[227] Di Xiao, Gui-Bin Liu, Wanxiang Feng, Xiaodong Xu, and Wang Yao. Coupled spin and valley physics in monolayers of mos 2 and other group-vi dichalcogenides. *Physical Review Letters*, 108(19):196802, 2012.

[228] M Yagmurcukardes, François M Peeters, Ramazan Tuğrul Senger, and H Sahin. Nanoribbons: From fundamentals to state-of-the-art applications. *Applied Physics Reviews*, 3(4):041302, 2016.

[229] Masafumi Yamamoto. Superconducting properties of tase3. *Journal of the Physical Society of Japan*, 45(2):431–438, 1978.

[230] Masafumi Yamamoto. Superconducting properties of tase3. *Journal of the Physical Society of Japan*, 45(2):431–438, 1978.

[231] T Yamamoto, S Kikkawa, and M Koizumi. Lithium secondary battery using monoclinic nbs3 prepared under high pressure. *Journal of The Electrochemical Society*, 133(8):1558–1561, 1986.

[232] K. Yamaya, T.H. Geballe, J.F. Kwak, and R.L. Greene. The effect of pressure on the superconducting transition temperature in tase3. *Solid State Communications*, 31(9):627 – 630, 1979.

[233] Jun Yan, Erik A. Henriksen, Philip Kim, and Aron Pinczuk. Observation of anomalous phonon softening in bilayer graphene. *Phys. Rev. Lett.*, 101:136804, Sep 2008.

[234] Zhong Yan, Guanxiong Liu, Javed M Khan, and Alexander A Balandin. Graphene quilts for thermal management of high-power gan transistors. *Nature communications*, 3:827, 2012.

[235] Hongtao Yuan, Xiaoge Liu, Farzaneh Afshinmanesh, Wei Li, Gang Xu, Jie Sun, Biao Lian, Alberto G Curto, Guojun Ye, Yasuyuki Hikita, et al. Polarization-sensitive broadband photodetector using a black phosphorus vertical p–n junction. *Nature nanotechnology*, 10(8):707, 2015.

[236] Wangzhi Yuan and John R Günter. Insertion of bivalent cations into monoclinic nbs3 prepared under high pressure and their secondary batteries. *Solid State Ionics*, 76(3-4):253–258, 1995.

[237] SV Zaitsev-Zotov, VF Nasretdinova, and VE Minakova. Charge-density waves physics revealed by photoconduction. *Physica B: Condensed Matter*, 460:174–179, 2015.

[238] M Zarenia, A Perali, D Neilson, and FM Peeters. Enhancement of electron-hole superfluidity in double few-layer graphene. *Scientific reports*, 4:7319, 2014.

[239] Bartosz M. Zawilski, Roy T. Littleton, and Terry M. Tritt. Description of the parallel thermal conductance technique for the measurement of the thermal conductivity of small diameter samples. *Review of Scientific Instruments*, 72(3):1770–1774, 2001.

[240] B.M. Zawilski, R.T. Littleton IV, N.D. Lowhorn, and T.M. Tritt. Observation of a two level thermal conductivity in the low-dimensional materials. *Solid State Communications*, 150(29):1299 – 1302, 2010.

[241] A. Zettl, C.M. Jackson, A. Janossy, G. Grüner, A. Jacobsen, and A.H. Thompson. Charge density wave transition and nonlinear conductivity in nbs3. *Solid State Communications*, 43(5):345 – 347, 1982.

[242] C.-H. Zhang and Yogesh N. Joglekar. Excitonic condensation of massless fermions in graphene bilayers. *Phys. Rev. B*, 77:233405, Jun 2008.

[243] Enze Zhang, Peng Wang, Zhe Li, Haifeng Wang, Chaoyu Song, Ce Huang, Zhi-Gang Chen, Lei Yang, Kaitai Zhang, Shiheng Lu, et al. Tunable ambipolar polarization-sensitive photodetectors based on high-anisotropy rese2 nanosheets. *ACS nano*, 10(8):8067–8077, 2016.

[244] Yi Zhang, Tay-Rong Chang, Bo Zhou, Yong-Tao Cui, Hao Yan, Zhongkai Liu, Felix Schmitt, James Lee, Rob Moore, Yulin Chen, et al. Direct observation of the transition from indirect to direct bandgap in atomically thin epitaxial mose2. *Nature nanotechnology*, 9(2):111–115, 2014.

[245] Weijie Zhao, Zohreh Ghorannevis, Leiqiang Chu, Minglin Toh, Christian Kloc, Ping-Heng Tan, and Goki Eda. Evolution of electronic structure in atomically thin sheets of ws2 and wse2. *ACS Nano*, 7(1):791–797, 2013.

[246] Zhaoqiang Zheng, Tanmei Zhang, Jiandomg Yao, Yi Zhang, Jiarui Xu, and Guowei Yang. Flexible, transparent and ultra-broadband photodetector based on large-area wse2 film for wearable devices. *Nanotechnology*, 27(22):225501, 2016.

[247] Mengjian Zhu, Davit Ghazaryan, Seok-Kyun Son, Colin R Woods, Abhishek Misra, Lin He, Takashi Taniguchi, Kenji Watanabe, Kostya S Novoselov, Yang Cao, et al. Stacking transition in bilayer graphene caused by thermally activated rotation. *2D Materials*, 4(1):011013, 2016.

[248] Z. Y. Zhu, Y. C. Cheng, and U. Schwingenschlögl. Giant spin-orbit-induced spin splitting in two-dimensional transition-metal dichalcogenide semiconductors. *Phys. Rev. B*, 84:153402, Oct 2011.

[249] John M Ziman. *Electrons and Phonons: Theorz of Transport Phenomena in Solids*. Clarendon Press, 1962.

[250] E Zupanič, HJP van Midden, M van Midden, S Šturm, E Tchernychova, V Ya Pokrovskii, SG Zybtsev, VF Nasretdinova, SV Zaitsev-Zotov, WT Chen, et al. The basic and the charge density wave modulated structures of nbs3-ii. *arXiv preprint arXiv:1804.02232*, 2018.

[251] A. Zwick, M.A. Renucci, R. Carles, N. Saint-Cricq, and J.B. Renucci. Correlation between k = 0 optical phonons in nbs3 and phonons in zrs3. *Physica B+C*, 105(1):361 – 365, 1981.

[252] S. G. Zybtsev, V. Ya. Pokrovskii, V. F. Nasretdinova, and S. V. Zaitsev-Zotov. Gigahertz-range synchronization at room temperature and other features of charge-density wave transport in the quasi-one-dimensional conductor nbs3. *Applied Physics Letters*, 94(15):152112, 2009.

[253] S. G. Zybtsev, V. Ya. Pokrovskii, V. F. Nasretdinova, S. V. Zaitsev-Zotov, V. V. Pavlovskiy, A. B. Odobesco, Woei Wu Pai, M.-W. Chu, Y. G. Lin, E. Zupanič, H. J. P. van Midden, S. Šturm, E. Tchernychova, A. Prodan, J. C. Bennett, I. R. Mukhamed-shin, O. V. Chernysheva, A. P. Menushenkov, V. B. Loginov, B. A. Loginov, A. N. Titov, and M. Abdel-Hafiez. Nbs$_3$: A unique quasi-one-dimensional conductor with three charge density wave transitions. *Phys. Rev. B*, 95:035110, Jan 2017.

[254] SG Zybtsev, V Ya Pokrovskii, VF Nasretdinova, and SV Zaitsev-Zotov. Growth, crystal structure and transport properties of quasi one-dimensional conductors nbs3. *Physica B: Condensed Matter*, 407(11):1696–1699, 2012.